The Bright Side of the Black Hole: Flares from Sgr A*

Katie Dodds-Eden

München 2010

The Bright Side of the Black Hole: Flares from Sgr A*

Katie Dodds-Eden

Dissertation
an der Fakultät für Physik
der Ludwig–Maximilians–Universität
München

vorgelegt von
Katie Dodds-Eden
aus Canberra, Australia

München, den 28. September 2010

Erstgutachter: Prof. Dr. Reinhard Genzel

Zweitgutachter: Prof. Dr. Andreas Burkert

Tag der mündlichen Prüfung: 13. December 2010

To the dear memory of my grandmother, Reta Dodds, my uncle, Ken Moyse, and my granddad, Francis Eden.

Contents

List of Figures

List of Tables

Zusammenfassung

Sgr A*, die Strahlungsquelle, die dem schweren schwarzen Loch im Zentrum der Milchstraße entspricht, bietet uns die besondere Möglichkeit, Phänomene in der unmittelbaren Nähe eines schwarzen Lochs zu beobachten. Da Sgr A* nur mit 10^{-8} seiner Eddington-Leuchtkraft strahlt, gehört die Quelle zu den schwächsten bekannten strahlenden schwarzen Löchern (sogenannte Low Luminosity Active Galactic Nuclei, LLAGN). Sgr A* ist die am besten untersuchbare Quelle dieser Art, da sie vergleichsweise nah, nämlich in unserer eigenen Milchstraße lokalisiert ist. Während das Vorhandensein eines schwarzen Lochs im Galaktischen Zentrum lange angezweifelt wurde, stellt die Beobachtung der Bewegung einzelner Sterne in Umlaufbahnen um Sgr A* heute den besten Beleg dafür da, dass schwarze Löcher überhaupt existieren.

Durch Beobachtung und Modellierung der langwelligen Emission von Sgr A* (Radio- bis submm-Bereich) ist bekannt, dass die relativ konstante Emission in diesen Wellenlängenbereichen durch Synchrotron-Strahlung eines stark magnetisierten, dünnen, relativistischen Plasmas in einem mehrschichtigen, strahlungsineffizienten Akkretionsfluss erzeugt wird. Im inneren Bereich in der Nähe des schwarzen Lochs liegen die typische magnetische Flussdichte, die Dichte und der Gamma-Faktor des Plasmas bei etwa $B \approx 30$ G, $n_e \approx 10^7$ cm^{-3} und $\gamma \approx 10$. Andererseits ist die physikalische Ursache für die sporadischen Strahlungsausbrüche (*Flares* im folgenden), die etwa eine Stunde dauern und im Nahinfrarot- (NIR) und Röntgenbereich häufig beobachtet werden, weiterhin ein ungelöstes Rätsel. Sie wurden erst in den letzten zehn Jahren entdeckt. Das Ziel dieser Arbeit ist es, den physikalischen Ursprung der Flares von Sgr A* zu untersuchen.

Diese Arbeit beginnt mit drei einführenden Kapiteln: Zunächst werden astrophysikalische schwarze Löcher im allgemeinen besprochen (Kapitel 1), danach die Beobachtungen von Sgr A* in Kapitel 2. In Kapitel 3 dann werden die Eigenschaften der wichtigsten Strahlungsprozesse für die Quelle, Synchrotron-Strahlung und inverse Comptonstreuung, zusammengefasst. Der Hauptteil der Arbeit beginnt in Kapitel 4 mit der Vorstellung der Multiband-Beobachtungen eines Flares am 4. April 2007, der sowohl im Nahinfrarot- als im Röntgenbereich detektiert wurde. Es ist der bislang hellste Flare während einer Simultanbeobachtung in beiden Wellenlängenbereichen. Die Beobachtungen wurden mit der Nahinfrarotkamera NAOS-CONICA (NACO) am Very Large Telescope (VLT) und dem Röntgensatelliten XMM-Newton durchgeführt. Die spektralen Eigenschaften dieses Flares waren zunächst unverständlich. Zu Beginn meiner Arbeit war die favorisierte Erklärung für die Röntgenflares von Sgr A* der Mechanismus inverser Compton-Streuung

von submillimeter- oder NIR-Photonen mit energiereichen Elektronen mit Gamma-Faktoren von $\gamma \sim 100$–1000. Nach den neuen Beobachtungen vom 4. April 2007 jedoch sprechen die beobachteten mittleren spektralen Indizes gegen inverse Compton-Streuung als Ursprung der Röntgenflares, da dieser Mechanismus physikalische Parameter für das Plasma (z.B. Magnetfeldstärke, Elektronendichte oder submm-Photonendichte) innerhalb der Flareregion benötigen würde, die in ihrer Grösse stark abweichen von den Werten, die für den Akkretionsfluss aus den längerwelligen Beobachtungen bestimmt wurden. Eine alternative Möglichkeit ist, dass die Röntgenflares durch Synchroton-Strahlung von noch energiereicheren Elektronen mit Gamma-Faktoren um $\gamma \sim 10^5 - 10^6$ entstehen. Dieses Szenario erfordert physikalische Parameter, die in ihrer Gösse auf natürliche Weise zu den aus den Beobachtungen abgeleiteten Werten der Emissionsregion passen.

Diese Ergebnisse werden in Kapitel 5 vertieft, wo ich detaillierte, zeitabhängige Modelle für die zeitliche Entwicklung der spektralen Energieverteilung (SED) des Flares vorstelle. Die Emission wird dabei aus einer Population an Elektronen berechnet, wobei deren Energien selbstkonsistent zeitlich evolviert werden, unter der Annahme dass hochenergetische Elektronen injiziert werden und Kühl- und Verlustprozesse wirken. Das simultane Modellieren von NIR- und Röntgen-Lichtkurven wurde hier zum ersten Mal selbstkonsistent durchgeführt. Mittels dieser Analyse konnte ich einen wichtigen Aspekt der Multiband-Beobachtungen vom 4. April 2007 identifizieren - nämlich, dass die beobachteten NIR- und Röntgen-Flares zeitlich verschiedene Längen haben, die Emissionsmaxima aber trotzdem gleichzeitig stattfinden. Dies bedeutet, dass viele einfache Injektions- und Kühlszenarien ausgeschlossen werden konnten. Um die beobachteten Lichtkurven reproduzieren zu können, war es notwendig, eine Abnahme des Magnetfelds parallel zur Elektroneninjektion anzunehmen. Solch eine Abnahme des Magnetfelds hat in der Tat eine sehr natürliche Erklärung in einem physikalischen Bild, in dem magnetische Energie in Bewegungsenergie von Elektronen umgewandelt wird, wie etwa in einer magnetischen Rekonnexion.

Der letzte Teil dieser Arbeit (Kapitel 6) geht in das andere Extrem: Ich untersuche die allgemeinen Eigenschaften der Variabilität von Sgr A* im nahen Infrarot, indem ich einen großen, unverzerrt Ks-Band Datensatz zusammenstelle, der aus Beobachtungen über sechs Jahren hinweg mit NACO/VLT gewonnen wurde. Der Datensatz entspricht effektiv einer 184 Stunden lange Lichtkurve von Sgr A*. Zunächst stellt man fest, dass Sgr A* eine permanente, variable Quelle bei niedrigen NIR-Flüssen ist. Weiterhin zeigt die Flussverteilung, dass es Unterschiede zwischen der schwachen und starken Emission von Sgr A* gibt. Bei niedrigen Flüssen kann die Flussverteilung als logarithmische Normalverteilung beschrieben werden. Dies deutet auf einen Prozess mit multiplikativem Charakter als Ursprung für die schwache Emission hin. Ein Beispiel dafür wäre ein Filtern von Dichteschwankungen, die an verschiedenen Radien im inneren Akkretionsfluss erzeugt werden. Andererseits zeigt die Flussverteilung bei größeren Flüssen einen flacheren Auslauf. Der flachere Auslauf der Flussverteilung bei höheren Energien könnte durch den zusätzlichen Beitrag von einzelnen, energiereichen Fluss-Ausbrüchen zustande kommen. Solche Ereignisse könnten, im Gegensatz zur Emission bei niedrigen Flüssen, durch spontane magnetische Rekonnexionen im Akkretionsfluss verursacht werden, wie die detaillierte Modellierung der NIR- und Röntgen-Lichtkurven für das helle Flare am 4.April 2007 suggeriert.

Summary

Sgr A*, the radiative manifestation of the massive black hole known to reside in our galaxy's center, provides us with an enormously valuable window into phenomena occurring in the very close environment of a black hole. Emitting at a mere 10^{-8} of its Eddington luminosity, Sgr A* belongs to the weakest emitting class of observed, radiating massive black holes (Low Luminosity Active Galactic Nuclei, or LLAGN), and due to its proximity in our own galaxy, is the most accessible example. While in fact the presence of a black hole at the Galactic Center was long doubted due to Sgr A's incredible faintness, observations of the dynamics of close orbiting stars about Sgr A* now provide the best proof for the existence of a black hole anywhere in nature.

Through observations and modeling of the long wavelength (radio to sub-mm) emission of Sgr A* it is generally known that the relatively steady emission at these wavelengths arises from the synchrotron emission of a highly magnetized, tenuous, relativistic plasma in a stratified, radiatively inefficient accretion flow. In the central regions close to the black hole the typical magnetic field strength, density and gamma factor of the plasma are known to be of the order of $B \approx 30$ G, $n_e \approx 10^7$ cm^{-3}, and $\gamma \approx 10$. On the other hand, the physical origin of sporadic emission – *flares* – of $\sim$1 hour duration observed frequently from Sgr A* at near-infrared (NIR) and X-ray wavelengths and only discovered within the last decade, is still a great mystery. The aim of this thesis is to investigate the physical origin of the flares of Sgr A*.

This thesis begins with three introductory chapters: we start with astrophysical black holes in general in Chapter 1, review the observations of Sgr A* in Chapter 2, and summarize properties of the most relevant radiative processes for this source – synchrotron and inverse Compton scattering – in Chapter 3. The main part of this thesis then begins (Chapter 4) with the presentation of multiwavelength observations of a flare from April 4, 2007, observed at both NIR and X-ray wavelengths: the brightest simultaneous NIR/X-ray flare that has yet been observed. The observations were obtained with the near-infrared imager NAOS-CONICA (NACO) at the Very Large Telescope (VLT) and the X-ray satellite XMM-Newton. The spectral properties of this flare were at first puzzling. Previously, the inverse Compton scattering of sub-mm or NIR photons by energetic electrons with gamma factors $\gamma \sim$100-1000 has been the most popular explanation for the X-ray flares from Sgr A*. With the new observations of April 4, 2007, however, the observed average spectral slopes argue against inverse Compton scattering for the origin of the X-ray flare, because this would require physical parameters for the flaring region (e.g. magnetic field

strengths and electron densities, or sub-mm photon densities) that are extreme compared to those inferred for the steady state flow from the long wavelength observations. An alternative which remains is that the X-ray flare is produced from the synchrotron emission of even more energetic electrons with gamma factors $\gamma \sim 10^5 - 10^6$, a scenario which works rather naturally with reasonable physical parameters for the emission region.

These findings are followed up in Chapter 5, where I present detailed time-dependent models for the evolution of the Spectral Energy Distribution (SED) of a flare with time, the emission computed from a population of electrons with energies self-consistently evolved subject to the injection of high energy electrons, escape and cooling processes. This work was the first to model simultaneous NIR/X-ray lightcurves from Sgr A* self-consistently and in detail. From this analysis, I could identify that one crucial aspect of the multiwavelength observations of April 4, 2007 – that the observed NIR and X-ray lightcurves have different durations, though they are simultaneous – implied that many simple injection plus cooling scenarios were ruled out. Instead, to reproduce the observed lightcurves I found it necessary to invoke a decrease in the magnetic field accompanying the electron injection in the model flares. Such a decrease in magnetic field has in fact a very natural explanation in a physical scenario where magnetic energy is being converted to energize the electrons, such as in a magnetic reconnection event.

The final part of this thesis (Chapter 6) goes to the other extreme: I present a study of overall characteristics of the variability of Sgr A* in the near-infrared by putting together a large unbiased dataset of Ks-band observations collected with NACO/VLT over a six year period, an effectively $\sim$184 hour lightcurve of Sgr A*. It is found, first of all, that Sgr A* appears to be a persistent, variable source at low levels in the NIR. Secondly, the distribution of fluxes in this dataset demonstrates that there are differences between the low and high flux emission from Sgr A*. At low fluxes, the flux distribution can be described by a lognormal distribution. This indicates a multiplicative origin to the low level variability, such as might be produced, for example, by the filtering of density fluctuations produced at different radii through to the inner regions of the accretion flow. On the other hand, at high fluxes the flux distribution exhibits a flatter tail. The flatter tail of the flux distribution at high fluxes could be due to an extra contribution of isolated, energetic events to the flux of Sgr A*. Such events, in contrast to the low level emission, could plausibly arise through spontaneous magnetic reconnection events in the accretion flow, as is suggested for the origin of the bright flare of April 4, 2007 from detailed modeling of the NIR and X-ray lightcurves.

Chapter 1

Black Holes in Nature

1.1 A Theoretical Curiosity

Einstein's elegant field equations form the foundation of the theory of General Relativity, the most well-established theory of gravitation:

$$G_{\mu\nu} = \frac{8\pi G}{c^2} T_{\mu\nu} \tag{1.1}$$

(e.g. Misner et al., 1973). With G a constant (the gravitational constant) and c the speed of light, the field equations relates the geometry of spacetime (the 4-dimensional unification of 3D space and time, represented by the Einstein tensor, $G_{\mu\nu}$), to its energy content (represented by the energy-momentum tensor, $T_{\mu\nu}$).

According to Einstein's theory, all energy (whether in matter form or radiation form) both distorts and responds to the intrinsic geometry of spacetime. Major predictions of the theory have undergone stunning verification in precision tests in the solar system (see Will, 2006). However, the consequences of the theory for very dense matter can be totally mind-boggling: the gravitational field surrounding very dense objects can be so strong that light itself (also subject to gravity in Einstein's theory) cannot escape. For such an object, no radiation emitted from within a critical radius, the *event horizon*, will ever be seen by the outside world: the term *black hole* is used to describe these curious objects.

1.1.1 Schwarzschild black holes

The solution to the Einstein field equations for the spacetime geometry outside a stationary, uncharged, spherically symmetric object of mass is the Schwarzschild metric (Schwarzschild, 1916):

$$g_{\mu\nu}dx^\mu dx^\nu = -\left(1 - \frac{R_S}{r}\right)c^2 dt^2 + \left(1 - \frac{R_S}{r}\right)^{-1} dr^2 + r^2 \left(d\theta^2 + \sin^2\theta d\phi^2\right) \tag{1.2}$$

where R_S is the Schwarzschild radius, an important length scale for a black hole[1]:

$$R_S = \frac{2GM}{c^2}. \tag{1.3}$$

At the Schwarzschild radius (the event horizon) the escape speed approaches the speed of light, and within R_S not even photons can escape the object's gravitational pull. If a (spherically symmetric, non-spinning) object is compact enough such that it is smaller than its Schwarzschild radius, then the object has no causal contact with the outside world and is a black hole. Stable circular orbits about the black hole only exist down to a radius of

$$R_{LSO} = 3R_S. \tag{1.4}$$

called the last stable orbit, or LSO.

1.1.2   Kerr black holes

Schwarzschild black holes are a special (non-spinning) case of a more general class of black holes with angular momentum, the Kerr black holes (Misner et al., 1973). In fact, since most distributions of matter (from which black holes must form) have some angular momentum, Kerr black holes are those expected to be found most commonly in nature. Charged black holes are not expected since the electrostatic forces of a charge black hole would be so large as to attract enough opposite charge to neutralize the black hole immediately. The *no hair theorem* postulates that the only distinguishable properties of a black hole is its mass, spin and charge. Astrophysical black holes are thus expected to be entirely characterized by their mass and their spin.

The solution to the Einstein equations for a stationary point mass with non-zero angular momentum was discovered by Roy Kerr in 1963; the metric in this case is (Kerr, 1963):

$$\begin{aligned}
g_{\mu\nu}dx^\mu dx^\nu &= -\left(1 - \frac{R_S r}{r^2 + a^2 \cos^2\theta}\right) c^2\, dt^2 - \left(\frac{r^2 + a^2 \cos^2\theta}{r^2 - R_S r + a^2}\right) dr^2 \\
&\quad + \left(r^2 + a^2 \cos^2\theta\right) d\theta^2 - \left(\frac{2R_S a^2 \sin^2\theta r}{r^2 + a^2 \cos^2\theta}\right) c\, dt\, d\phi \\
&\quad + \left(r^2 + a^2 + \frac{R_s a^2 r}{r^2 + a^2 \cos^2\theta}\sin^2\theta\right)\sin^2\theta\, d\phi^2
\end{aligned}$$

where a is the *spin parameter*, defined as the angular momentum J divided by the object mass and c:

$$a = J/Mc \tag{1.5}$$

A Kerr black hole has two important radii:

$$R_{\text{event horizon}} = \frac{R_S + \sqrt{R_S^2 - 4a^2}}{2} \tag{1.6}$$

---

[1]in Chapter 6 we denote the Schwarzschild radius by r_g instead of R_S, since in the publication associated with this Chapter we also presented the results of MHD simulations, where the notation r_g is more commonly used.

and

$$R_{\text{static limit}} = \frac{R_S + \sqrt{R_S^2 - 4a^2 \cos^2 \theta}}{2} \tag{1.7}$$

which form two surfaces. The inner, spherical surface is the event horizon, within which causal contact is lost with the outside world.

   The region between the outer surface, of an oblate spheroid shape, and the inner event horizon, is named the ergosphere. Within the ergospherere, spacetime itself is dragged along with the rotation of the black hole (an effect that has been named frame-dragging) at speeds faster than the speed of light. A test particle entering the ergosphere is dragged along with the rotating spacetime and cannot stay stationary with respect to the rest of the universe. At the outer horizon, the *static limit*, a particle can just stay stationary with respect to the rest of the universe if it travels (in the reverse direction to the rotation) at the speed of light.

   Of course, when $a = 0$, $r_{\text{event horizon}} = r_{\text{static limit}}$ and there is no ergosphere (the solution reduces to the Schwarzschild case). There is also thought to be a maximum value of the spin. From Equation 1.6, one can see that there is no real-valued solution for the value of r_{inner} if the spin parameter $a > GM/c^2$. A black hole with spin parameter $a = GM/c^2$ is called an extreme Kerr black hole. It is thought unlikely that a super-extreme Kerr black hole could really occur in nature, because there would be no event horizon to hide the central (ring-like) singularity from the rest of the universe.

   For an extreme Kerr black hole ($a = GM/c^2$) there are two last stable orbits, one for particles orbiting in the opposite direction to the black hole's rotation, *retrograde* orbits,

$$R_{LSO}(\text{extreme Kerr, retrograde}) = 4.5 \ R_S \tag{1.8}$$

and the same direction as the black hole's rotation, *prograde* orbits,

$$R_{LSO}(\text{extreme Kerr, prograde}) = 0.5 \ R_S. \tag{1.9}$$

Since the event horizon of an extreme Kerr black hole is also at $R = 0.5R_S$, then for black holes with spin, matter may orbit the black hole on stable circular orbits down to the event horizon of the black hole.

1.2   The Search for Real Black Holes

The black hole solution was initially thought to be little more than a theoretical curiosity: it seemed inconceivable that such wierd objects could really be present in the natural world. It is really a sign of the incredible advances that have occurred in astronomy in the last fifty years that we can now be quite sure that black holes exist, and that they are probably even quite commonplace in the universe.

   Some of the most important advances were the surprising new astronomical discoveries of the late 1950s and 1960s – the first quasars, luminous objects at large redshift (Schmidt, 1963), the first detections of extrasolar X-ray sources (Giacconi et al., 1962) of which one of

the first was Cygnus X-1, and the first pulsar (Hewish et al., 1968). With the discovery of the pulsar it was apparent that exotic objects like neutron stars could, shockingly, actually exist in the universe and be observable. It was not too much of a leap to suspect that the same may be true of black holes, and that these might be the agent responsible for both the quasars (which would require supermassive black holes, perhaps at the centers of young galaxies) and the binary X-ray sources, powered by black holes of a few stellar masses.

The first convincing evidence for a black hole came with Cygnus X-1, an X-ray emitter in a binary system. Measuring the variation of the spectral lines of the stellar companion, implies a mass greater than 3 $M_\odot$ (Webster & Murdin, 1972; Bolton, 1972). This exceeds the theoretical maximum mass for neutron-degeneracy-supported matter (Oppenheimer & Volkoff, 1939; Bombaci, 1996), and is considered strong evidence that Cygnus X-1 is indeed a black hole.

The great advantage of the X-ray binary systems in deducing the presence of a black hole is the direct determination of the mass of the unseen object from the dynamics of the companion star. Black holes in the centers of galaxies, generally, do not lend themselves to the kinds of direct dynamical measurements possible in the X-ray binary systems, and must be considered black hole candidates. There is however one exception to this: the massive black hole in the center of our own galaxy (for a review, see Genzel et al., 2010). Exceptionally strong evidence for the existence of a black hole there comes from the star S2, which has been observed to complete a complete orbit in the past 16 years. Simple analysis of the orbit (as determined from astrometric and spectroscopic monitoring, and which follows, to the current best precision, a perfect Keplerian ellipse) shows that there must be a mass of 4×10^6 $M_\odot$ within S2's distance of closest approach of only $\approx 1300 R_S$. The high minimum density this implies inside the S2 orbit rules out even exotic alternatives to a supermassive black hole, such as a cluster of dark objects like neutron stars or black holes, or a single massive ball of fermions. A single massive ball of bosons remains as a possible alternative, although such an object is expected to have a relatively short lifetime (after which it would any way collapse to form a black hole). The dark object at the position of Sgr A* in the Galactic Center is thus considered to be the most convincing case of a black hole in nature.

1.3   Radiation from Accretion

The basic idea behind accretion flows is the liberation of gravitational energy. Consider the work done in moving a particle of mass m from infinite distance to the surface R_* of a massive body of mass M_*. The energy lost by the particle in accomplishing this journey is

$$\Delta E = \int_{R_*}^{\infty} \frac{GM_*m}{r^2} dr = \frac{GM_*m}{R_*} \tag{1.10}$$

If the accretion flow is reasonably efficient at converting the gravitational potential energy of accreting particles into electromagnetic radiation then it is possible that considerable

amounts of radiation can be produced via accretion. This is especially true for very massive and very compact objects. For a Schwarzschild black hole, for example, where $R_S = 2GM/c^2$ it's possible that the energy liberated by the accreting matter is as much as

$$\Delta E = 0.5mc^2 \tag{1.11}$$

which is about 70 times the efficiency of hydrogen-burning of the same mass ($\Delta E \approx 0.007mc^2$). In practice numerical models show that the radiative efficiency of luminous accretion flows is more of the order of $\Delta E = 0.1mc^2$. For sources for which the rate at which the matter is moving inwards quickly (a high accretion rate), high luminosities can be achieved. The high luminosities obtainable led accretion to proposed as a good candidate to power the unusually distant and luminous quasars. Accretion is now believed to be responsible for the observed radiation from X-ray binaries and a whole range of galactic nuclei.

Evidence is beginning to build (e.g. Falcke et al. 2004; McHardy et al. 2006) that certain properties of accreting sources, from the stellar mass black holes up to AGN, are independent of the amount of central mass M, i.e. that accretion proceeds in a relatively similar way in both stellar mass black hole systems and around the supermassive black holes at the centers of galaxies. The most important influence then on their behavior appears to be rather the rate at which they are accreting matter $\dot{M}$. The behavior of accreting black holes in X-ray binaries, for example, is seen to depend on L/L_{Edd}, where L is, to some extent, an observational substitute for $\dot{M}$. Cygnus X-1, for example, is seen to make transitions between a *low hard state*, at low luminosity to a *high soft state* at $L \approx 0.01L_{Edd}$ (see Figure 1.1). The important luminosity here L_{Edd} is the Eddington luminosity, above which the outwards pressure of radiation in the source would overwhelm the inwards gravitational force and halt the inwards flow of matter:

$$L_{Edd} = \frac{4\pi G m_p c}{\sigma_T} M \simeq 3.4 \times 10^5 \left(\frac{M}{M_\odot} \right) \, L_\odot. \tag{1.12}$$

The Eddington luminosity of a black hole of Sgr A*'s mass, for example, is $\approx 10^{11} \, L_\odot$.

Other X-ray binaries are observed to make similar transitions between a low hard state and a high soft state, at luminosities in the range $L/L_{Edd} = 0.003 - 0.2$ (Done et al., 2007). There are also other states that have been identified, but which we do not go into here. These are usually intermediate states that can be associated with the transition from the low hard state to the high soft state or vice versa.

At high luminosities the *high soft state* is characterised by a soft X-ray spectrum with a prominent bump that can be well fit with a blackbody. This blackbody component is interpreted to indicate the presence of a standard optically thick disk (Shakura & Sunyaev, 1973) in the accretion flow.

At lower luminosities, there is the *low hard* state, at which the properties of the source become very different to those of higher luminosities: the X-ray spectrum becomes harder, and the blackbody component disappears or becomes less prominent. The timing properties, as demonstrated by the form of the Power Spectral Density distribution (PSD), are
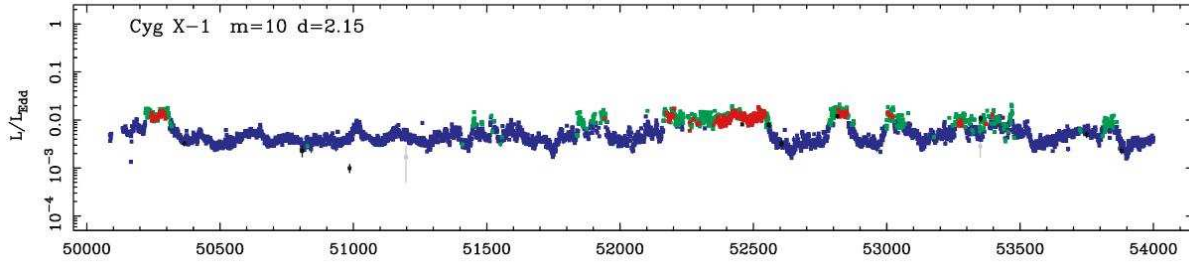
Figure 1.1 The lightcurve of Cygnus X-1, reproduced from Done et al. (2007). The x axis shows the Modifed Julian date (MJD). The different colors correspond to state transitions in the source, in particular the low hard state (blue) and the high soft state (red). There is also a "very high state" (green) and measurements for which the state was uncertain (black).

also different to those of the high soft state. In the low hard state, the inner disk is thought to be replaced by a hot, optically thin, geometrically thick flow (see Section 2.1.1). The disk of the higher luminosity soft state may still be present, but is truncated at outer radii, and generally there is much less contribution from a thermal blackbody component to the spectrum. Alternatively, the low hard state is the signature of a jet taking over as the dominant contributor to the emission at low luminosity (e.g. Fender et al., 2004).

At even lower luminosities, there is what is called the *quiescent state*. It is however, not known whether the quiescent state is even a distinct state from the low hard state, or whether perhaps the low hard state continues all the way down to extremely low accretion rates. The lowest accretion rate X-ray binary that is known is A0620-00, at $L \approx 10^{-8} L_{Edd}$ (discovered in outburst in 1975 by Elvis et al. 1975), of similar accretion rate to Sgr A*. Sgr A* is much easier to observe due to its proximity and higher Eddington luminosity. This property makes Sgr A* an extremely valuable source to study, if not just in its own right, but as an archetype of low accretion rate sources.

Sgr A* and other AGN not only offer a high luminosity window into low-accretion rate accreting systems, they also offer an opportunity to examine the time-dependent properties of emission from accretion around black holes in very fine detail, in comparison to the time dependence of emission from X-ray binaries. A typical timescale for an accreting source is the dynamical timescale, $t_{dyn} \simeq \sqrt{R_S^3/2GM}$, which scales linearly with mass M. Comparing timescales in Cyg X-1 (taking $M \approx 10 M_\odot$; Remillard & McClintock 2006) with the corresponding timescales in Sgr A* ($M = 4 \times 10^6 M_\odot$; Gillessen et al. 2009), we can see that if indeed an analogy can be drawn between accreting sources of all masses, then short timescales in an X-ray binary correspond to very long timescales in an AGN:

Cyg X-1	Sgr A*
1 ms	7 minutes
1 second	4.6 days
1 minute	280 days
1 hour	45 years
1 day	1100 years

While we are rather unlikely to ever see a state transition like those seen in X-ray binaries in a supermassive accreting source, we have in these sources the potential to observe the short timescale variability with better statistics and in much finer detail than is possible for the stellar mass black hole systems. In other words, in Sgr A* we can sit back and watch low-density accretion in "slow motion".

Chapter 2

The Massive Black Hole at the Galactic Center

The first time I went to Paranal Observatory in the Atacama desert in Chile, only a few months after beginning my Ph.D., it was remarkably easy to spot by eye the on-sky location of the supermassive black hole – Sgr A* – at the center of our Galaxy. This was because we were shining a bright laser beam, an 'artificial star', directly at it, using this Laser Guide Star to aid with the correction of image distortions due to the light's passage through the Earth's atmosphere (see Figure 2.1 for a stunning image taken by Yuri Beletsky on this actual observation run, July 2007).

In reality, what I was seeing with the naked eye when I looked towards the patch of sky where the laser beam was pointing was, however, nothing that is really that close to the true Galactic Center at all; though beautiful, what I was gazing at was really just a bunch of dust clouds far in front of the Galactic Center. From our position in the disk of our Galaxy, ~8 kpc from the center and situated in the plane of the Galactic disk, the line of sight towards the supermassive black hole passes through incredible quantities of dust, which at visible wavelengths blocks all but 10^{-10} (i.e. effectively all) of the visible light originating from the Galactic Center. Because of the dust, we have no hope to ever see anything of the innermost regions of our own galaxy at visible wavelengths, not with the naked eye, nor with the largest existing telescopes, nor even the even larger telescopes one might imagine will conceivably be built in the future.

Fortunately however the Galactic Center is not entirely lost to observation, because as soon as one turns to wavelengths other than visible one starts to see through the incredible wall of dust and we are introduced to the rich and beautiful environment of the Galactic Center. At radio wavelengths, the center of the Galaxy is full of glowing gas and dust, with arcs, streamers and filaments sculpted by magnetic fields. At X-ray wavelengths, the region is awash with X-ray emitting point sources (stellar mass black holes, neutron stars, white dwarfs) and supernova remnants, within a glow of diffuse emission. And at near-infrared wavelengths, one sees the stunning cluster of stars, old and young, that surround and crowd around the central massive black hole at the center of our Galaxy.

In the last two decades, some incredible advances have taken place that have resulted

Figure 2.1 VLT, Laser Guide Star pointing at the Galactic Center (during SINFONI observations, July 2007). Image credit: Yuri Beletsky

in the most direct and compelling evidence for a black hole, anywhere in the universe, and that being the black hole at our own Galactic Center. It is the central cluster of stars, seen in the near-infrared, that have provided this evidence. Two teams, one at the MPE and one based at UCLA, have tracked some of the innermost stars over the last 18 years, watching them move, accelerate, and even in some cases make complete orbits of the central massive black hole. It is a dream experiment, monitoring effective test particles as they complete perfect Keplerian orbits (as far as can be currently measured, though deviations due to relativistic effects are hoped for in the future) in the strong gravitational field of a much more massive object. These observations have proven beyond reasonable doubt that the central dark object at the common focus of the elliptical orbits of the stars must consist of about 4 million solar masses with little possibility for it to be anything but a black hole (Schödel et al., 2002; Ghez et al., 2003; Eisenhauer et al., 2005a).

2.0.1   Sgr A*: the Radio to Submm Source

There is something radiating very close to the massive black hole at the center of the Galaxy: a curious, compact, radio source coincident with the dynamical center which was
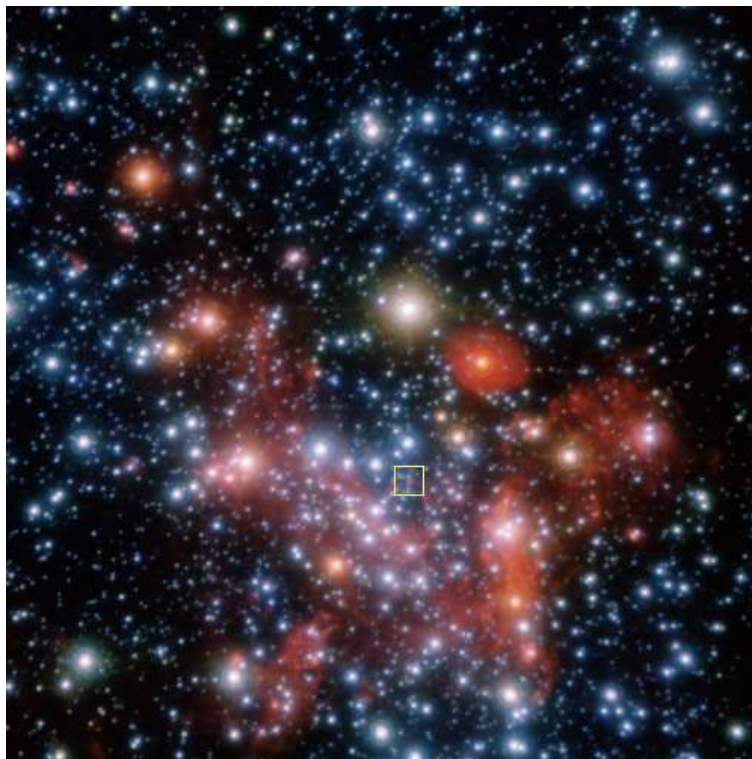
Figure 2.2 Three color combined near-infrared image of the Galactic Center. Sgr A* can be seen in this image, as the red source at the center of the yellow box.

first discovered and reported by Balick & Brown in their 1974 paper, titled *Intense Sub-arcsecond Structure in the Galactic Center*. This source, subsequently given the name Sagittarius A* (Sgr A* for short) in Brown (1982), had several unusual properties: it had a high brightness temperature, was unresolved on scales of a tenth of an arcsecond, and appeared to be at the very center of the Galaxy (within the inner parsec). These were all facts which pointed towards it being the radiative counterpart of a black hole in our own galactic nucleus – similar to what was seen at the time, at a much more energetic level, in quasars (that such a source, in analogy to quasars, might be found at the center of our own galaxy had in fact been predicted several years prior to Sgr A*'s discovery by Lynden-Bell & Rees 1971).

Variability

Brown & Lo (1982) discovered the Sgr A* source was variable, displaying (at 2.7 and 8.1 GHz) 20-40% variations on all time scales from years to days. The amplitude of the variability increases towards higher frequencies, up to factors of a few at mm/submm frequencies (e.g. Zhao et al., 2001, 2003). There appear to be long-term variations ($\sim$100 days, e.g. Zhao et al., 2001) which are long for typical dynamical timescales in the disk

and are thought to be likely linked to accretion rate variations. Also seen are very short variations on timescales of ∼hours (Bower et al., 2002).

Spectrum

Multiwavelength efforts have mapped out the spectral energy distribution of Sgr A*. The spectrum rises from radio towards submm wavelengths with a spectral index of roughly $\beta = 1.2$ at long wavelengths (where β is defined as $\nu L_\nu \sim \nu^\beta$). The spectral index appears to increase to $\beta \approx 1.4$ above 100 GHz, but no steady emission can be detected above roughly 10^{12} Hz, implying that the spectral energy distribution (SED) turns abruptly around at this point (Zylka et al., 1995; Serabyn et al., 1997; Falcke et al., 1998). This feature has been named the 'submm bump' – and the fact that the spectrum suddenly cuts off is seen to be an indication of the size of the black hole.

Polarization

Sgr A* shows different polarization properties at high frequencies compared to low frequencies. Above ∼100 GHz the emission has significant linear polarization on the level of $\sim 10\%$ (Aitken et al., 2000; Bower et al., 2002). In contrast, below ∼100 GHz however the linear polarization is very low ($< 1\%$, Bower et al. 1999) and the source is circularly polarized on the level of 0.3-1%.

Size measurements:

The short timescale variability of the source alone argues for a small size. However, even more stringent constraints have been obtained on the source structure in Sgr A* through VLBI observations. Studies have been carried out by (Rogers et al., 1994; Krichbaum et al., 1998; Lo et al., 1998; Doeleman et al., 2001; Bower et al., 2004, 2006; Shen et al., 2005). These studies show that the intrinsic size of Sgr A* is very compact and varies with wavelength. Bower et al. (2006) found, for example

$$R(\lambda) \approx 13 \ R_S \ (\lambda/0.35\text{cm})^{1.3 \text{ to } 1.7}. \tag{2.1}$$

The measurement of the intrinsic source size at long wavelengths is however complicated by interstellar scattering, which broadens the image. The influence of interstellar scattering is less severe at shorter wavelengths, such that it becomes possible to ever better disentangle the intrinsic size from the scatter-broadened size with increasing frequency. Doeleman et al. (2008) have reported size measurements at the shortest wavelengths yet (1.3 mm), where the scattering is far less important, finding a size of ≈ 40 micro-arcseconds, which would correspond to $4R_S$.

$$R(1.3\text{mm}) \approx 4R_S \tag{2.2}$$
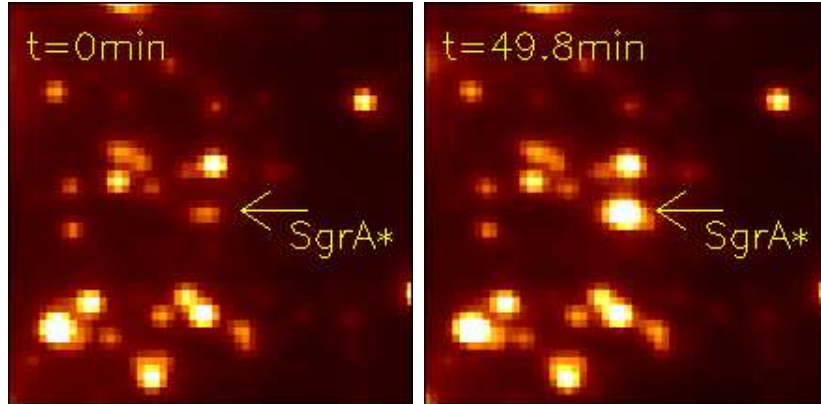
Figure 2.3 Observations from 5th August 2008, on which a very bright flare occurred. The arrow indicates the position of Sgr A*. In the space of 50 minutes, the source brightens by a factor of ≈ 27. This flare is presented in Section 6 (Dodds-Eden et al., 2010b)

2.0.2 Near-infrared and X-ray Flares from Sgr A*

A rather recent discovery from the Galactic Center has been the discovery of dramatic NIR (Genzel et al., 2003b) and X-ray (Baganoff et al., 2001) flares.

General Features

Prominent NIR flares occur on average ~ 4 times per day (see e.g. Figure 18, Eckart et al., 2006a), or between 30-40% of the observing time (Yusef-Zadeh et al., 2006a). Flux increases up to factor ~ 20 have been observed. The typical duration is on the order of ~ 80min (Genzel et al., 2010).

The X-ray flares on the other hand are detected less frequently than the NIR flares, occurring on average ~ 1 per day (Baganoff, 2003). Flux increases of up to factor ~ 160 have been observed. The typical duration is ~ 50 min (Genzel et al., 2010). X-ray flares may occur in clusters: Porquet et al. (2008) observed a sequence of flares within half a day (a bright flare followed by three flares of more moderate flux).

Substructures & Quasi-Periodic Variability

The first flares to be observed in the near-infrared exhibited intriguing substructural features in their lightcurves (Genzel et al., 2003b), which have a tantalising possible explanation in the Doppler-beaming of a hot emission region as it rotates about the black hole, close to the last stable orbit. The timescales of these substructures are often on the order of 15-20 minutes, which, if associated directly with the orbital timescale of matter at or near the last stable orbit of the black hole, would imply the black hole has non-zero spin (of $a \sim 0.5$). Similar substructural variations with characteristic timescales of 15-25 minutes have been seen also in many other NIR flares (Genzel et al., 2003b; Meyer et al., 2006; Eckart et al., 2006c; Trippe et al., 2007; Do et al., 2009a).

The X-ray flares on the other hand do not in general display such obvious QPO-like features. A more typical property of X-ray flares seems to be significant and very sharp drops in flux, often near the flare peak (Baganoff et al., 2003; Porquet et al., 2003, 2008).

Polarization

Polarimetric investigations of the flares in the NIR have shown that the source is significantly polarized and exhibits dramatic swings in the polarization degree and angle during the flare (Eckart et al., 2006b). In the cases where the polarization properties of the emission are clear-cut (Eckart et al., 2006b; Trippe et al., 2007; Meyer et al., 2006; Eckart et al., 2008a), the polarization appears to be lower (10%) near the peak of the flare, and higher (30-40%) at lower flux levels, with the swing occurring as the emission decays.

Spectral properties

There have been studies of the spectral index (we define the spectral index, β, here through $\nu L_\nu \sim \nu^\beta$) of the flares in the NIR through both spectroscopy and through broadband imaging. For low fluxes quite red spectral indices have been reported, for example Ghez et al. (2005), Eisenhauer et al. (2005a) and Krabbe et al. (2006). The emission was quite faint in these studies ($F_{Ks} \lesssim$ a few mJy, dereddened with $A_{Ks} = 2.8$ mag), with the exception of Krabbe et al. (2006) with $F_K \sim 6$mJy.

Gillessen et al. (2006) caught a brighter flare ($F_{Ks} \sim 8$mJy) with an apparent trend of spectral index with flux. These authors discussed several possible methods for correcting for the uncertain background (faint stars contributing to the emission and/or an unknown quiescent state of Sgr A*). Using an 'off state' subtraction method, which essentially yields an upper limit on the colour they obtained $\beta = -1.4 \pm 0.4$ and $\beta = 0.4 \pm 0.2$ for faint and bright states, respectively. A different method which aims to subtract the maximum amount of stellar contribution (with $\beta_{\text{star}} \approx 3$) that would be consistent with the data, essentially yielding a lower limit to the spectral index, results in values of $\beta = -3.4 \pm 0.4$ and $\beta = -0.3 \pm 0.2$ for the faint and bright state, respectively.

A different study, using colours derived from broadband imaging at M, L, K' and H-bands, Hornstein et al. (2007) derived an average spectral index $\beta = 0.4 \pm 0.2$ for all epochs, observation bands, and observed fluxes. They found no significant trend in spectral index with flux. A background subtraction was only carried out for the H-K' data in these measurements (justified as the subtraction of stellar contamination which is more important at H-K'), via the subtraction of the minimum of the lightcurve. Some of the flares analysed by Hornstein et al. (2007) reached rather high fluxes, one reaching 20 mJy (dereddened for $A_{Ks} = 2.8$ mag).

The two brightest X-ray flares (Porquet et al., 2003, 2008) have been observed to have well constrained soft νL_ν spectral index values $\beta = -0.2 \pm 0.3$ and $\beta = -0.3 \pm 0.3$ calculated at a 90% confidence range (Porquet et al., 2008). For other, moderately bright to faint flares, harder spectral index values are reported (e.g., the first X-ray flare observed with Chandra, for which $\beta = 1.0^{+0.8}_{-0.7}$, 90% confidence, Baganoff et al., 2001). However,

at least in data obtained with XMM-Newton, Porquet et al. (2008), using a homogeneous data analysis could not however confirm a statistically significant trend of spectral index with flux.

Multiwavelength Observations

Simultaneous multiwavelength observations are needed to discover how the NIR flares of Genzel et al. (2003b) and X-ray flares of Baganoff et al. (2001) relate to each other. The first discovery of a *simultaneous* NIR and X-ray flare was made by Eckart et al. (2004). Further multiwavelength campaigns have found further examples of simultaneous NIR and X-ray flares, 10 in total: (Bélanger et al., 2005; Eckart et al., 2006a; Yusef-Zadeh et al., 2006a; Hornstein et al., 2007; Eckart et al., 2008a; Marrone et al. , 2008; Yusef-Zadeh et al., 2008; Porquet et al., 2008; Yusef-Zadeh et al., 2009; Trap et al., 2010), including the flare presented in Chapter 4 of this thesis (Dodds-Eden et al., 2009). Generally, these simultaneous NIR/X-ray flares are seen to peak within minutes of each other, with no significant delay.

There is, however, not a one-to-one ratio between detected NIR and X-ray flares. In all cases where an X-ray flare was detected in observations simultaneous to observations in the NIR, a NIR counterpart has always been observed. However, there have been cases of NIR flares which have had no X-ray counterpart (Hornstein et al., 2007). Peak flux ratios between the NIR and X-ray flares can vary widely (e.g. Trap et al. 2010, in prep.).

In simultaneous observations at longer wavelengths, no significant activity simultaneous to the NIR/X-ray flares is observed. There have however been several tentative reports of flares at mm and submm wavelengths occurring subsequent to NIR/X-ray wavelengths, delayed by $\sim$100 minutes. Much more well-established are lags between variations at different radio wavelengths; e.g. between 43 and 23 GHz, with longer wavelengths lagging the higher frequency emission (Yusef-Zadeh et al., 2006b).

Steady State Emission in X-ray and Near-infrared

A source that could correspond to the extrapolation of the radio to submm steady-state spectrum to high frequencies, has never unambiguously been detected in the NIR. Upper limits on such a steady state source are on the ~ 2 mJy level (dereddened with $A_{Ks} = 2.8$, Hornstein et al. 2002, Schödel et al. 2007, Sabha et al. 2010).

On the other hand, Chandra X-ray observations revealed a steadily emitting source at X-ray wavelengths (Baganoff et al., 2003), which is resolved and has a spatial extent of $\approx 1''$. However, because of the spatial extent, this steady source must be produced in the outer regions of the accretion flow and cannot be directly related to the compact source, which must be produced at small radii. The quiescent X-ray source most likely originates from Bremstrahlung emission, for which the outer regions of the accretion flow, close to the Bondi radius, are expected to contribute the most emission (Quataert, 2002).

2.1 Models for Sgr A*

2.1.1 The submm-radio source

Sgr A* is extraordinarily faint, when compared to many other accreting black holes. Its bolometric luminosity, at about 300 $L_\odot$, is far below the Eddington limit for a black hole of its mass. It is not just a question of gas supply; there is enough gas from stellar winds for Sgr A* to accrete at a rate of $\sim 3 \times 10^{-6} M_\odot/yr$ (Cuadra et al., 2006), the "Bondi rate". The energy liberated by the accretion of this gas should produce a much greater radiative output ($\sim 10^5$ higher than observed). That the luminosity of Sgr A* is so low implies that either not much of the gas supply at outer radii is making it to the inner regions of the accretion flow, or alternatively, that the gas makes it to the inner radii of the accretion flow, but that very little of its mass energy is actually liberated in the form of radiation.

The steady state accretion flow around Sgr A* is often modelled as a RIAF (Radiatively Inefficient Accretion Flow, see Quataert 2003 for a review). RIAFs are a class of models describing accretion flows that are radiatively inefficient, either due to inefficient transport of gas to small radii, or due to true radiative inefficiency. Although analytical models for RIAFs (named ADAFs, Advection Dominated Accretion Flows) can reproduce the spectrum of Sgr A* with an accretion flow that is truly radiatively inefficient and accreting matter at the Bondi rate, the numerical models of RIAFs favor instead the opposite conclusion that the accretion flow is underluminous due to inefficient transport of mass to small radii. The simulations, for example, show shallower density profiles and thus lower densities close to the black hole than would be expected under simple spherical accretion.

The conclusions of the numerical RIAF models – that not much of the material available at large radii is making it to the inner regions of the accretion flow – are independently supported by the radio observations of Sgr A*: the high polarization of emission at $\nu > 100$ GHz implies the electron densities in the accretion flow are constrained to $\lesssim 10^6$ to 10^7 cm^{-3}; with higher densities Faraday rotation would act to depolarize the emission, and such high polarizations could not be observed. Typical values for the electron energy, electron density and magnetic field in the innermost regions of the accretion flow of the RIAF simulations that match the observations are $\gamma \sim 10$, $n_e \sim 10^6 - 10^7$cm^{-3} and $B \sim 10 - 30$ G (Yuan et al., 2003).

The accretion flow has also been modelled as a compact jet (e.g. Falcke & Markoff 2000, Markoff et al. 2001). The jet models come up with the same range of electron densities and magnetic field strengths for the innermost region of the jet as the RIAF models. In fact, these properties of the inner accretion flow appear to be independent of the particular model geometry and can be deduced from simple arguments (Loeb & Waxman, 2007).

2.1.2 Flare Models

The origin of the high amplitude variability at NIR and X-ray wavelengths from Sgr A* is not known. The timescales are inconsistent with tidal disruption of a star (Baganoff et al., 2001; Rees, 1988), and the few milli-arcseonds coincidence of the infrared flares with the

central mass implies the flares arise from the inner region of the accretion flow, inconsistent with production via the interaction of close orbiting stars with an accretion disk which would happen further out(Nayakshin & Sunyaev, 2003). It is unlikely to be an increase in the accretion rate of the steady state source at radio-submm wavelengths(Markoff et al., 2001), since increases of factor $\sim$20-100 that would be required to explain the X-ray flares are never been seen in the radio, despite extensive monitoring; further, in simultaneous X-ray/NIR and submm to radio observations do not reveal any simultaneous flaring counterpart at mm/submm wavelengths).

Baganoff et al. (2001) and Markoff et al. (2001) suggested the flare might instead be caused by a sudden acceleration of electrons in the inner accretion flow (triggered by, say, an accretion instability or a magnetic reconnection event). Electrons accelerated to energies of $\gamma \sim 100 - 1000$ could scatter submillimeter or NIR photons up to X-ray energies, or the NIR photons could also be scattered by the submm-emitting electrons. The cooling time of the $\gamma \sim 100 - 1000$ electrons would be on the timescale of hours for the typical magnetic field strengths of the accretion flow, which would suit the observed timescale of X-ray flares very well.

However, it also could be that the X-ray emission is due to direct synchrotron emission from very energetic $\gamma \gtrsim 10^5$ electrons, although the cooling time of the electrons responsible for the X-ray emission would then be much shorter than the duration of the X-ray flare, and there would need to be sustained energization of electrons for the duration of the X-ray flare. There are nevertheless a number of ways accelerated electrons can produce X-ray emission via synchrotron and inverse Compton scattering with different combinations of accelerated electrons and origins of seed photons. The discovery of the NIR flares fits into the transient acceleration picture if $\gamma \sim 100 - 1000$ electrons are emitting synchrotron emission at NIR wavelengths Yuan et al. (2004), but many aspects remain to be filled in, such as the emission mechanism of the NIR/X-ray flares, the physical conditions in the flaring region and the reason for the sudden energization.

As a starting point, it seems reasonable to assume that the physical parameters in flares should probably not be too far from the typical values in the steady state accretion flow, since this determines the availability of electrons and the background magnetic field strength – or at least that any significant enhancement or reduction from the quiescent values should be understandable in terms of a physical picture. A number of authors have developed models under various inverse Compton scenarios, and show that generally the observed aspects (of specific flares) can be satisfied with physical parameters (e.g. magnetic field B, electron density n_e) that seem plausible for the inner regions of the accretion flow around Sgr A*.

The following list of NIR/X-ray emission mechanisms have been proposed in the literature:

- *NIR/X-ray Synchrotron*
  (Markoff et al., 2001; Yuan et al., 2003, 2004)

- *NIR synchrotron, X-ray IC of NIR photons by NIR-emitting electrons (SSC)*

(Yuan et al., 2003; Liu et al., 2004; Eckart et al., 2004, 2006c; Liu et al., 2006a; Marrone et al. , 2008).

- *NIR synchrotron, X-ray IC of submm photons by NIR-emitting electrons (submm photon IC)*
  (Baganoff et al., 2001; Yuan et al., 2003; Yusef-Zadeh et al., 2006a).

- *NIR synchrotron, X-ray IC of NIR photons by submm-emitting electrons (NIR photon IC)*
  Yusef-Zadeh et al. (2006a)

- *NIR SSC, X-ray SSC*
  (Liu et al., 2004; Eckart et al., 2004)

In Chapter 3 we have put together an overview of the synchrotron and inverse Compton radiation processes.

More recent models have also turned their attention to the longer wavelengths, where possible delays are seen with respect to the NIR and X-ray flares, and the flares are modelled from X-ray to radio wavelengths as the adiabatic expansion of expanding blobs (van der Laan, 1966). Marrone et al. (2008) suggested that the short timescales of the rise/decay of delayed emission in the mm/submm – too short for the estimated synchrotron cooling times at those wavelengths – was an indication that the cooling was provided by some energy-independent mechanism such as adiabatic cooling. They also suggested that the stability of the spectral index indicated by the results of Hornstein et al. (2007) suggests that the cooling mechanism in the NIR is also energy-independent (and therefore unlikely to be synchrotron cooling).

Another branch of models attempt to explain the more detailed time dependent structure of the emission at a single wavelength, such as models where the flare is a hot spot orbiting in the inner regions of the accretion flow (Broderick & Loeb, 2005; Meyer et al., 2006; Trippe et al., 2007; Hamaus et al., 2009), or models where the flare is due to an accretion instability (Tagger & Melia, 2006; Falanga et al., 2008), or a density perturbation Chan et al. (2009).

Chapter 3

Radiation Processes

3.1 Simple Radiative Transfer

The observed radiation from a medium in which emission and absorption processes are taking place can be determined by solving the radiative transfer equation. We consider here only very simple radiative transfer from a homogeneous source (i.e. where the emission and absorption rates are constant over the source). All the basic definitions following can be found in Rybicki & Lightman (1986).

A fundamental quantity in radiative transfer is the specific intensity, I_ν, defined as the energy crossing a unit area dA in time dt in frequency range $d\nu$ in solid angle $d\Omega$:

$$I_\nu = \frac{dE}{dt\ d\nu\ dA\ d\Omega} \qquad [\text{erg s}^{-1}\text{Hz}^{-1}\text{cm}^{-2}\text{steradian}^{-1}] \tag{3.1}$$

Emission within the source is described by the quantity j_ν, the monochromatic emission coefficient, defined as the energy emitted per second per unit frequency per unit volume per steradian:

$$j_\nu = \frac{dE}{dt\ d\nu\ dV\ d\Omega} \qquad [\text{erg s}^{-1}\text{Hz}^{-1}\text{cm}^{-3}\text{steradian}^{-1}] \tag{3.2}$$

Absorption is described by the quantity α_ν, the absorption coefficient, defined as the fraction of intensity lost from the beam, per unit length, when traversing the absorbing medium:

$$\alpha_\nu = -\frac{dI_\nu}{I_\nu} \qquad [\text{cm}^{-1}] \tag{3.3}$$

Two other useful quantities are the optical depth, τ_ν, defined as

$$d\tau_\nu = \alpha_\nu ds \tag{3.4}$$

and the source function, S_ν, defined as

$$S_\nu = \frac{j_\nu}{\alpha_\nu} \tag{3.5}$$

The optical depth, τ_ν indicates the total fraction of incident intensity absorbed along a path parameterized by s. The source function indicates the relative strength of emission to absorption per unit volume of the source, i.e. the net intensity produced per unit volume.

As a beam of intensity travels a distance ds, its intensity changes by

$$dI_\nu = j_\nu ds - \alpha_\nu I_\nu. \tag{3.6}$$

This is the *radiative transfer equation*. Integrating along a full path through the source, one obtains the formal solution of the radiative transfer equation:

$$I_\nu(\tau_\nu) = I_\nu(0)\exp(-\tau_\nu) + \int_0^{\tau_\nu}\exp(-(\tau_\nu - \tau_\nu'))S_\nu(\tau_\nu')d\tau_\nu' \tag{3.7}$$

as a function of optical depth ($I_\nu(0)$ is the initial intensity before traversing the source, i.e. the incident intensity). For a constant source function (i.e. constant j_ν and α_ν) along a given path, and not considering any incident intensity, the solution of Equation 3.7 is simply

$$I_\nu = S_\nu(1 - \exp(\tau_\nu)). \tag{3.8}$$

3.1.1   Homogeneous Sphere

We now want to know the observed radiation from a source. For this equation (2.8) must be integrated over the geometry of our emitting region, considering all possible paths, τ_ν, through the source. In this thesis, we assume the source of radiation is a homogeneously emitting and absorbing sphere. Solving the radiative transfer equation for this geometry, one obtains the flux measured by an observer at distance R_0 (Gould, 1979):

$$F_\nu = \frac{\pi R^2}{R_0^2}\frac{\nu j_\nu}{\alpha_\nu}\left(1 + \frac{\exp(-2\alpha_\nu R)}{\alpha_\nu R} - \frac{1 - \exp(-2\alpha_\nu R)}{2\alpha_\nu^2 R^2}\right). \tag{3.9}$$

In this thesis we use the convention of expressing the result in units of νL_ν (total output power of the source with frequency) instead of the observed flux. While a L_ν spectrum shows the distribution of output power per unit frequency, a νL_ν spectrum gives an indication of the total power output of the source with frequency (the peak occurs at the frequency at which most power is emitted). In terms of νL_ν, Equation 3.9 becomes

$$\nu L_\nu = 4\pi^2 R^2\frac{\nu j_\nu}{\alpha_\nu}\left(1 + \frac{\exp(-2\alpha_\nu R)}{\alpha_\nu R} - \frac{1 - \exp(-2\alpha_\nu R)}{2\alpha_\nu^2 R^2}\right). \tag{3.10}$$

This has the optically thin limit ($\tau_\nu \ll 1$))

$$\nu L_\nu = 4\pi \times \frac{4\pi R^3}{3}\nu j_\nu. \tag{3.11}$$

and the optically thick limit ($\tau_\nu \gg 1$)

$$\nu L_\nu = 4\pi \times \pi R^2\frac{\nu j_\nu}{\alpha_\nu}. \tag{3.12}$$

The extra factor of 4π arises because j_ν is defined per steradian though we assume it to be isotropic.

3.2 Synchrotron Emission

An electron will, in the presence of a magnetic field, experience a force that depends on its charge, the strength of the magnetic field, and the velocity of the electron, as well as the orientation (the pitch angle, ϕ) of the electron's velocity relative to the magnetic field:

$$F = q|v||B|\sin\phi. \tag{3.13}$$

the force acts on the electron in the direction perpendicular to the velocity and magnetic field directions, causing it to accelerate in a helical path along the direction of the magnetic field line.

The acceleration of the moving charge will produce electromagnetic radiation, and is called cyclotron emission. It is emitted at distinct frequencies, corresponding to the frequency of the electron's orbit and its harmonics. When the electron has a relativistic velocity, the discrete spectrum emitted by the electron blends into a continuous spectrum, and is called synchrotron emission.

We give here the most general forms of the emission and absorption coefficients from which the synchrotron emission can be computed given an arbitrary energy distribution of electrons for which the velocities are oriented at random (are isotropic) with respect to the magnetic field direction. All the basic formulae given here can be found in Rybicki & Lightman (1986). These equations were used in Chapter 5 to calculate the instantaneous synchrotron spectrum from a population of electrons with an evolving energy distribution. In Chapter 4 we used however analytical equations for the synchrotron spectrum, assuming a thermal (relativistic Maxwellian) distribution of energies for which the emission and absorption coefficients can be written analytically.

Emission coefficient

The spectral power radiated by a single electron emitting synchrotron radiation with pitch angle ϕ relative to the magnetic field B is

$$P_e(\gamma, \nu, \phi) = \frac{\sqrt{3}q^3 B}{mc^2} F\left(\frac{\nu}{\nu_{syn}(\gamma, \phi)}\right)\sin\phi \qquad [\text{erg s}^{-1}\text{Hz}^{-1}] \tag{3.14}$$

where

$$\nu_{\text{syn}}(\gamma, \phi) = \frac{3q}{4\pi m_e c}B\gamma^2 \sin\phi \tag{3.15}$$

is the critical synchrotron frequency (the frequency at which the electron emits most of its radiation), and

$$F(x) = x \int_x^\infty K_{5/3}(\xi)d\xi \tag{3.16}$$

which contains the shape of the spectrum. Here q, m_e and c are the electron charge, mass, and the speed of light.

We assume a distribution of electrons with velocities distributed isotropically with respect to the magnetic field. We approximate the pitch angle averaged spectral power, $P_{iso}(\gamma, \nu)$, as

$$P_{iso}(\gamma, \nu, \phi) = \int P_e(\gamma, \nu, \phi)d\phi \approx P_e(\gamma, \nu, \phi = \arcsin(\pi/4)) \qquad [\text{erg s}^{-1}\text{Hz}^{-1}] \qquad (3.17)$$

(the evaluation at $\phi = \arcsin(\pi/4)$ is close to the true pitch angle averaged spectrum but much faster to evaluate). The angle-averaged value of the critical synchrotron frequency is

$$\nu_{\text{syn,iso}}(\gamma) = \frac{3qB}{16m_ec}B\gamma^2 \qquad (3.18)$$

The electrons have some arbitrary (but isotropic) distribution of energies with differential number density

$$dn_e = n_e(\gamma)d\gamma \qquad [\text{cm}^{-3}] \qquad (3.19)$$

The total spectral power emitted is the obtained by integrating over the energy distribution of the electrons:

$$P_{tot}(\nu) = \int_1^\infty n_e(\gamma)P_{iso}(\gamma, \nu)d\gamma \qquad [\text{erg s}^{-1}\text{Hz}^{-1}\text{cm}^{-3}] \qquad (3.20)$$

The emission coefficient (which is defined per steradian though we assume isotropy) is finally computed as

$$j_\nu = \frac{1}{4\pi}P_{tot}(\nu) \qquad [\text{erg s}^{-1}\text{Hz}^{-1}\text{cm}^{-3}\text{steradian}^{-1}] \qquad (3.21)$$

Absorption coefficient

The absorption coefficient for a population of electrons with arbitrary energy distribution can be calculated from

$$\alpha_\nu = \frac{c^2}{8\pi\nu^2mc^2}\int_1^\infty n_e(\gamma)\left(\frac{2P_e(\gamma, \nu)}{\gamma} + \frac{dP_e(\gamma, \nu)}{d\gamma}\right)d\gamma \qquad (3.22)$$

3.2.1   Properties of the Spectrum

Given the synchrotron emission and absorption coefficients, we can compute the emitted spectrum using Equation 3.10. Here we show an overview of the properties of the emitted spectra, with examples from our numerical computations. Comparing with these well-known properties of synchrotron radiation also served as tests of our numerical code.

The Critical Frequency

A synchrotron-emitting electron emits most of its radiation at the critical frequency

$$\nu_{\text{syn}}(\gamma, \phi) = \frac{3q}{4\pi m_e c} B \gamma^2 \sin \phi \tag{3.23}$$

which for an isotropic distribution of electrons is

$$\nu_{\text{syn,iso}}(\gamma) = 3qB\gamma^2/(16m_e c) \tag{3.24}$$

This is the frequency at which the optically thin synchrotron spectrum from a monoenergetic distribution of electrons (of energy γ) turns over, when plotted in νL_ν which shows the total energy emitted per frequency interval. The spectrum from a monoenergetic distribution of electrons is plotted in both L_ν and νL_ν in Figure 3.1. The νL_ν spectrum is narrowly peaked close to the frequency $\nu_{syn,iso}$. The peak of the L_ν spectrum occurs at about $\nu = 0.29\nu_{syn,iso}$.
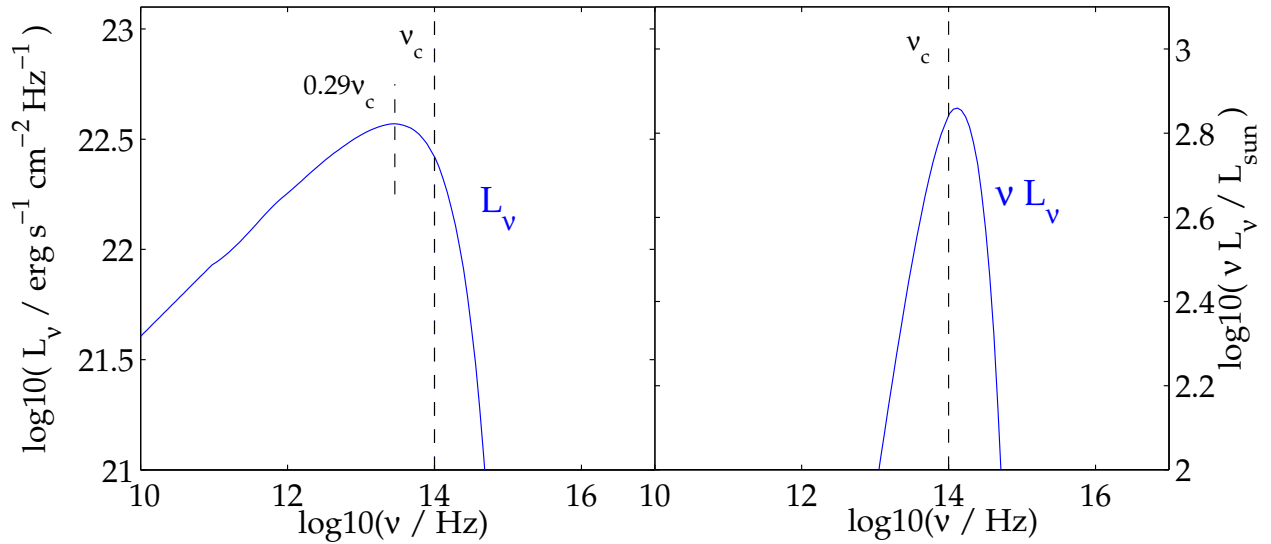
Figure 3.1 The spectrum from a monoenergetic distribution of electrons. In νL_ν the spectrum peaks close to the critical synchrotron frequency, $\nu_c \ (= \nu_{syn,iso})$.

The Spectral Index

The optically thin part of a synchrotron spectrum from a power-law electron spectrum with particle index p (i.e. $n_e(\gamma) \sim \gamma^{-p}$) has the spectral index ($\nu L_\nu \propto \nu^\beta$)

$$\beta = \frac{3-p}{2}$$
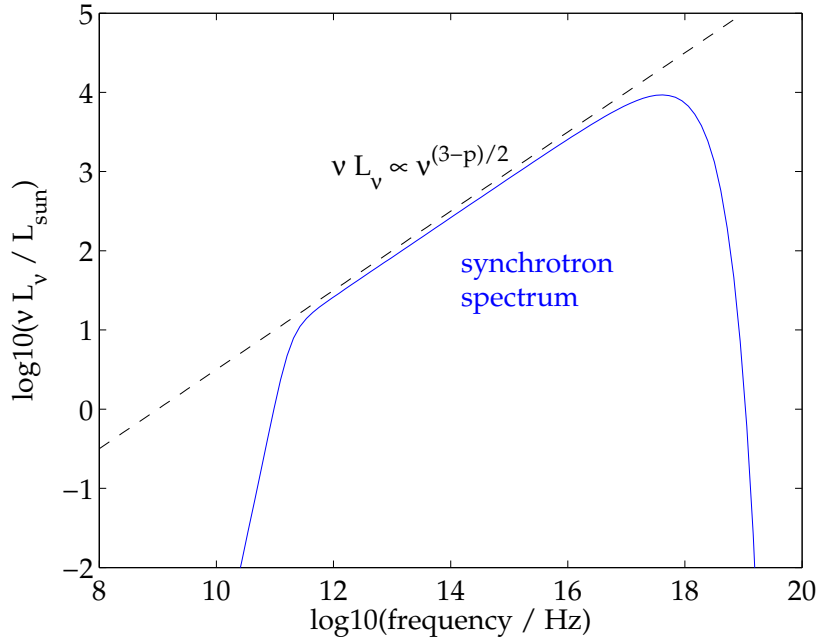
Figure 3.2 The synchrotron spectrum from a power-law electron distribution of particle index p has the spectral index $\beta = (3-p)/2$ where β is defined as $\nu L_\nu \propto \nu^\beta$.

Total Emitted Power (Angle-Averaged Emission and the Normalization of the Optically Thin Spectrum)

The total synchrotron power varies with pitch angle. The angle-averaged total synchrotron power emitted by electrons with energy γ is

$$P_{el,synch} = \frac{4}{3}\sigma_T c \beta^2 \gamma^2 U_B \tag{3.25}$$

where U_B is the magnetic energy density,

$$U_B = \frac{B^2}{8\pi} \tag{3.26}$$
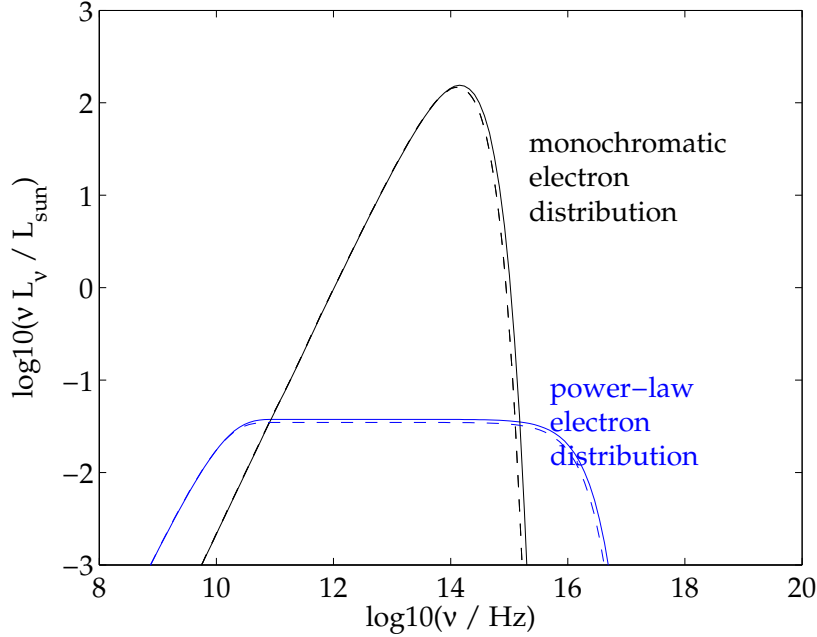
Figure 3.3 The dashed lines show the $\phi = \arcsin \pi/4$ approximation, and the solid lines shows the full numerical integration. The ratio of the total power in the two spectra is ≈ 0.92.

We check the normalization of the synchrotron spectrum in our numerical code by integrating over the calculated spectrum from a monoenergetic distribution of electrons and comparing the result, $P_{\text{tot,code}} = \int_0^\infty L_\nu d\nu$, with the expected power:

$$P_{\text{tot,synch}} = N_e \times P_{el,synch} = N_e \frac{4}{3} \sigma_T c \beta^2 \gamma^2 \frac{B^2}{8\pi} \tag{3.27}$$

Using our code where the integral over pitch angles is performed, we obtain $P_{tot,code} = 1.007 P_{tot,synch}$. In our faster code, where we use $\phi = \arcsin \pi/4$ as a reasonable approximation to the true pitch angle averaged spectrum, we obtain $P_{tot,code} = 0.93 P_{tot,synch}$. The two spectra are compared in Figure 3.3.

The Self-Absorption Frequency

The frequency at which the synchrotron spectrum becomes self-absorbed (often denoted ν_m) depends on the number of electrons, the size of the region in which they are contained, and the magnetic field strength, and also on the relative numbers of electrons at different energies (for a power-law electron spectrum, for example, this is expressed by the parameter p). Even for the power-law case, obtaining an expression for the self-absorption frequency is very complicated, involving the solution to a transcendental equation Gould

(1979). However, using the equations of Gould (1979), and assuming the electron spectrum continues down to $\gamma_{\min} = 1$, one can write down the following expressions for the self-absorption frequency for specific values of p:

$$\nu_m(p = 2, \gamma_{\min} = 1) = 4.83 \times 10^{10} \text{ Hz } \left(\frac{B}{5\text{G}}\right)^{2/3} \left(\frac{n_e}{10^7 \text{cm}^{-3}}\right)^{1/3} \left(\frac{R}{R_S}\right)^{1/3} \quad (3.28)$$

$$\nu_m(p = 3, \gamma_{\min} = 1) = 1.75 \times 10^{10} \text{ Hz } \left(\frac{B}{5\text{G}}\right)^{5/7} \left(\frac{n_e}{10^7 \text{cm}^{-3}}\right)^{2/7} \left(\frac{R}{R_S}\right)^{2/7} \quad (3.29)$$

$$\nu_m(p = 4, \gamma_{\min} = 1) = 8.45 \times 10^{9} \text{ Hz } \left(\frac{B}{5\text{G}}\right)^{3/4} \left(\frac{n_e}{10^7 \text{cm}^{-3}}\right)^{1/4} \left(\frac{R}{R_S}\right)^{1/4} \quad (3.30)$$

The ν_m given here corresponds to the frequency at which $dL_\nu/d\nu = 0$ (and is thus just an approximation of the point where the self-absorbed and optically thin spectrum would meet when extrapolated; see, for example the slight differences for different p in Figure 3.5). Figure 3.4 shows how the self-absorption frequency changes with region size for a $p = 4$ electron spectrum. The self-absorption frequency may be higher for given electron density if the minimum gamma factor of the electron spectrum is higher than $\gamma_{min} = 1$. However, one should be careful with higher $\gamma_{\min}$ that the expressions in Gould (1979), which rely on the fact that one is away from the endpoints of the electron spectrum, remain valid (the value of ν_m calculated with the above equations is not accurate, for example, if $\nu_{syn}(B, \gamma_{min}) > \nu_m$).
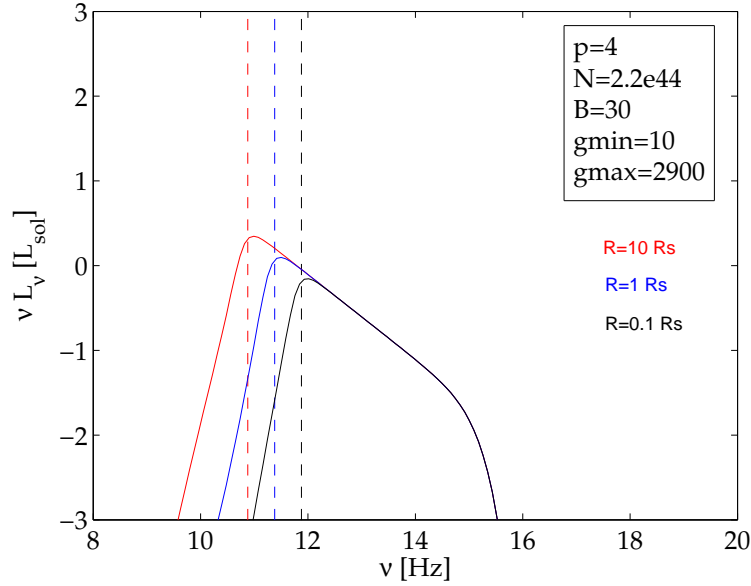
Figure 3.4 The self-absorption frequency for a power law distribution of electrons.

Comparison with analytical models for the spectrum

Another test of our code consisted of comparing our numerical results with analytical models for the spectrum in the special case of a power law distribution of electrons. In Figure 3.5 we demonstrate that the spectrum computed with our numerical code matches with the spectrum that is computed analytically by determining ν_m and S_m (the self-absorption frequency and the flux at that frequency) from Gould (1979) (see also Marscher 1983).

Model Parameters	Demonstration Figure
$B = 30$ G $n_e = 2.2 \times 10^6$ cm^{-3} $\gamma_{\min} = 10$ $\gamma_{\max} = 10^4$ $p = 2$ $R = 1\ R_S$	
$B = 30$ G $n_e = 2.2 \times 10^7$ cm^{-3} $\gamma_{\min} = 10$ $\gamma_{\max} = 10^4$ $p = 3$ $R = 1\ R_S$	
$B = 30$ G $n_e = 2.2 \times 10^7$ cm^{-3} $\gamma_{\min} = 10$ $\gamma_{\max} = 10^4$ $p = 4$ $R = 1\ R_S$	
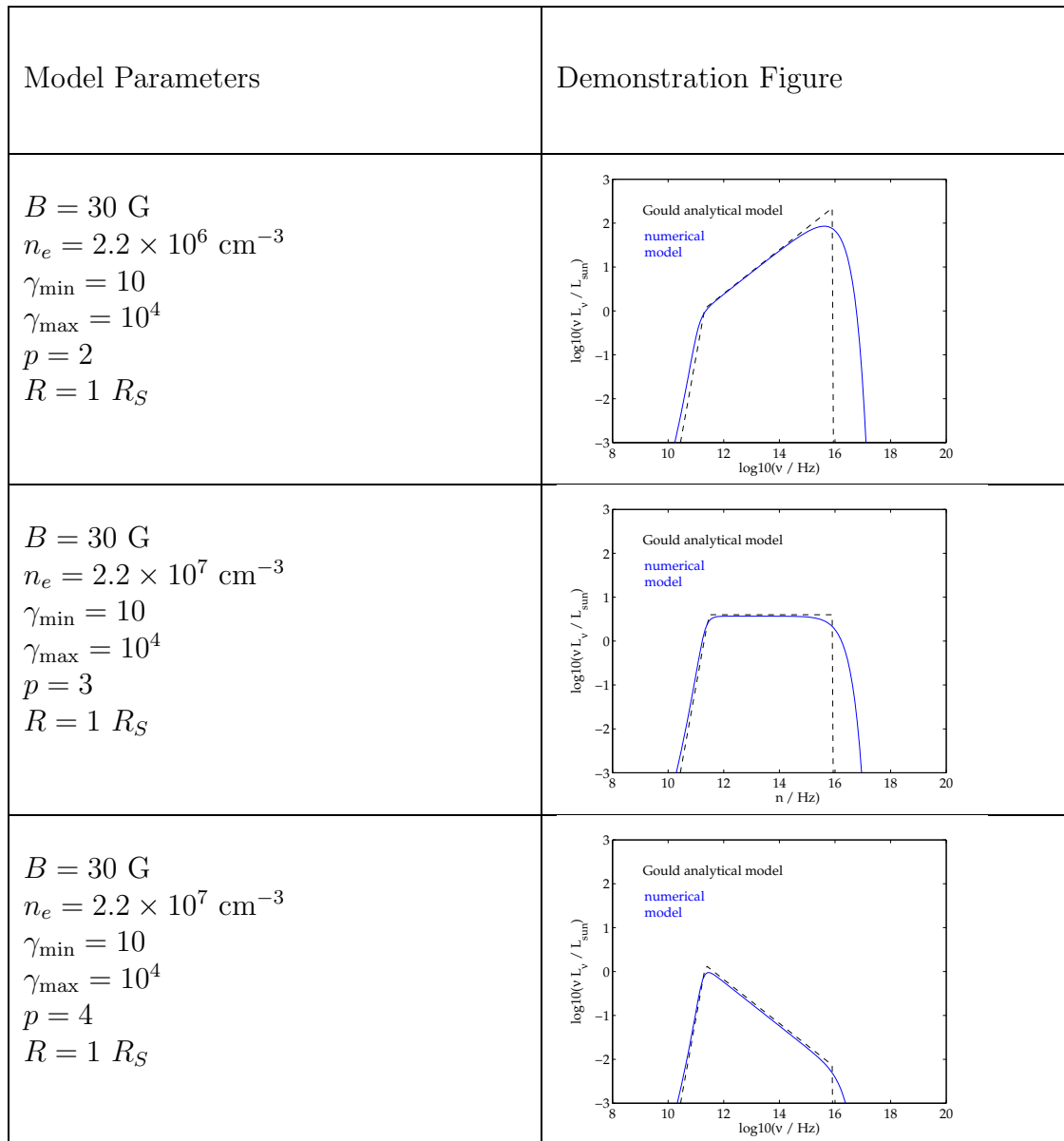
Figure 3.5 Comparison with analytic models.

3.3 Inverse Compton Scattering

In an interaction between a high-energy photon and a low-energy electron, the photon may give some energy to the electron in a process known as Compton scattering. The photon is scattered to a lower frequency, while the electron gains energy from the scattering. In cases where the electron is high energy compared to the photon the reverse process may occur: the electron may give energy to the photon, scattering it up in energy/frequency – this is called inverse Compton scattering.
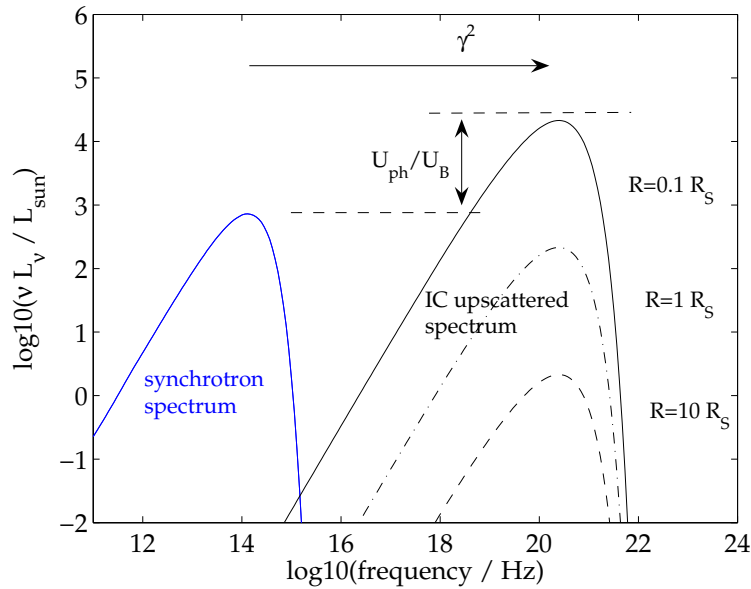
Figure 3.6 Synchrotron and SSC spectra from a monoenergetic electron distribution of energy γ_e. Since the synchrotron and upscattered spectra have similar shapes, $\max(\nu L_\nu) \propto \int L_\nu \, d\nu$ and the maximum of the IC spectrum can be predicted with the ratio $\nu L_{\nu,\text{IC}} = \nu L_{\nu,\text{synch}} U_{ph}/U_B$. The spectra shown have $U_B = 37$ erg cm^{-3} and $U_{\text{ph}} = 0.12$, 12 and 1200 erg cm^{-3} for $R = 10$, 1, and 0.1 R_S, respectively.

When the initial photon energy, $\epsilon_{\text{in}} = h\nu_{in}$, is very low compared to the mass of the electron in the electron rest frame ($\gamma\epsilon_{\text{in}} \ll mc^2$), the scattering is said to be in the Thompson limit. In this limit, a photon is scattered up in energy by a factor $\sim \gamma^2$ upon interaction with a relativistic electron, and the inverse Compton scattered luminosity is

$$P_{IC} = \frac{4}{3}\sigma_T c \gamma^2 \beta^2 U_{\text{ph}} \tag{3.31}$$

where U_{ph} is the photon energy density. We usually approximate the photon energy density of seed photons with total luminosity L_{seed} from a region with size R_{seed}, as

$$U_{\text{ph}} \approx \frac{L_{\text{seed}}}{4\pi c R^2} \tag{3.32}$$

Comparing with Equation 3.31 with Equation 3.25, one can see that

$$\frac{P_{IC}}{P_{synch}} = \frac{U_{\mathrm{ph}}}{U_B} \tag{3.33}$$

With observations of the positions and fluxes of the peaks of synchrotron and their inverse Compton spectra this property can often be used to infer physical parameters of the source (such as, e.g. the magnetic field strength, if the radius of the source can be estimated through some other means).

When a population of relativistic electrons emitting synchrotron radiation also upscatter their own photons, the process is called Synchrotron Self-Compton (SSC). Figure 3.6 demonstrates the basic properties of inverse Compton scattered spectra in the Thompson limit for the synchrotron and SSC spectra of a monoenergetic electron distribution. We verified that Equation 3.31 was satisfied upon integrating over the L_ν spectrum to obtain the total power.
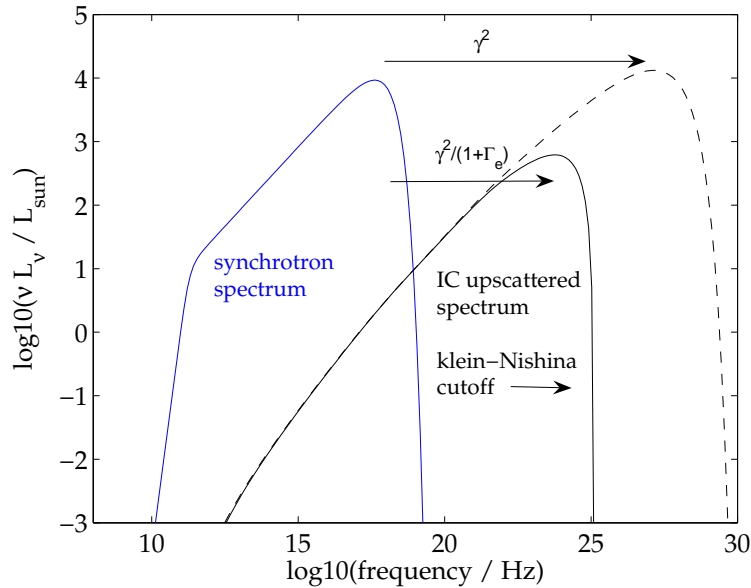
Figure 3.7 Demonstration of the Klein-Nishina limit for inverse Compton scattering. The blue line shows the synchrotron spectrum, produced by electrons with a power law energy distribution with a maximum gamma factor of $\gamma_{\mathrm{max}} = 10^5$ and $B = 30$G such that $\nu_{synch}(\gamma_{\mathrm{max}}, B) \approx 10^{18}$ Hz. The Compton factor for the scattering of the highest frequency photons from the highest energy electrons is then $\Gamma_e = \approx 3000$. The solid black line shows the correctly computed inverse Compton scattered spectrum, including Klein-Nishina effects, while the dashed line shows how the spectrum would be computed with the Thompson approximation only, not considering Klein-Nishina effects. The scattered spectrum is strongly suppressed above $\nu_{KN} = \nu_{synch}\gamma^2/(1 + \Gamma_e) \approx 10^{25}$Hz.

When the Thompson limit is no longer applicable the scattering becomes inelastic and the electron begins to lose large amounts of energy per scattering. Quantum mechanical effects on the scattering cross section can no longer be neglected, and the full cross section is called the Klein-Nishina cross section. The net result is that scattering above $\gamma^2(1+\Gamma_e)$ is strongly suppressed. The quantity Γ_e is the Compton factor,

$$\Gamma_e = 4\epsilon_{\text{in}}\gamma/mc^2 \tag{3.34}$$

which is very small ($\Gamma_e \ll 1$) in the Thompson limit, and large ($\Gamma_e \gg 1$) in the Klein-Nishina limit.

Taking the full Klein-Nishina cross section into account, the inverse Compton scattered luminosity can be calculated from (Blumenthal & Gould, 1970)

$$\nu L_{\nu,\text{IC}} = \frac{4\pi}{3}R_F^3(h\nu)^2 \int_\gamma n(\gamma) \int_{\epsilon_{\text{in}}} (dN_{\gamma,\epsilon_{\text{in}}}/dtd\epsilon_{\text{sc}}d\epsilon_{\text{in}})d\epsilon_{\text{in}}d\gamma \tag{3.35}$$

where γ, $\epsilon_{\text{in}} = h\nu_{\text{in}}$ and $\epsilon_{\text{sc}} = h\nu$ are the electron energy, initial and scattered photon energies respectively, and the quantity

$$\frac{dN_{\gamma,\epsilon_{\text{in}}}}{dtd\epsilon_{\text{sc}}d\epsilon_{\text{in}}} = \frac{3\sigma_T c\, n_{ph}(\epsilon_{\text{in}})}{4\gamma^2\epsilon_{\text{in}}}\left[2q\ln q + (1+2q)(1-q) + \frac{(\Gamma_e q)^2(1-q)}{2(1+\Gamma_e q)}\right] \tag{3.36}$$

where

$$q = \frac{\epsilon_{\text{sc}}}{\Gamma_e(\gamma mc^2 - \epsilon_{\text{sc}})}. \tag{3.37}$$

The number density of seed photons, $n_{ph}(\epsilon)$, is approximated by

$$n_{ph}(\epsilon) = n_{ph}(\nu)/h \approx L_{\nu,\text{seed}}/(4\pi h^2\nu cR_F^2). \tag{3.38}$$

An example spectrum with the suppression of emission at high frequencies because of the reduced scattering cross-section in the Klein-Nishina limit is shown in Figure 3.7.

Chapter 4

Multiwavelength Observations and the Emission Mechanism

Abstract: This paper reports measurements of Sgr A* made with NACO in L$'$-band (3.80 μm), Ks-band (2.12 μm) and H-band (1.66 μm) and with VISIR in N-band (11.88 μm) at the ESO VLT[1], as well as with XMM-Newton at X-ray (2-10 keV) wavelengths. On 4 April, 2007, a very bright flare was observed from Sgr A* simultaneously at L$'$-band and X-ray wavelengths. No emission was detected using VISIR. The resulting SED has a blue slope ($\beta > 0$ for $\nu L_\nu \propto \nu^\beta$, consistent with $\nu L_\nu \propto \nu^{0.4}$) between 12 micron and 3.8 micron.

For the first time our high quality data allow a detailed comparison of infrared and X-ray light curves with a resolution of a few minutes. The IR and X-ray flares are simultaneous to within 3 minutes. However the IR flare lasts significantly longer than the X-ray flare (both before and after the X-ray peak) and prominent substructures in the 3.8 micron light curve are clearly not seen in the X-ray data. From the shortest timescale variations in the L$'$-band lightcurve we find that the flaring region must be no more than 1.2 R_S in size.

The high X-ray to infrared flux ratio, blue νL_ν slope MIR to L$'$-band, and the soft νL_ν spectral index of the X-ray flare together place strong constraints on possible flare emission mechanisms. We find that it is quantitatively difficult to explain this bright X-ray flare with inverse Compton processes. A synchrotron emission scenario from an electron distribution with a cooling break is a more viable scenario.

---

[1]The Very Large Telescope (VLT) at the European Southern Observatory (ESO) on Paranal, Chile: Program IDs 179.B-0261(A) and 60.A-9234(A).

4.1   Introduction

The radio source coincident with the gravitational center of the Milky Way, named Sgr A*, was first discovered by Balick & Brown in 1974. It had already been suggested (Lynden-Bell & Rees, 1971) that the Milky Way may host a supermassive black hole at its center, and the newly discovered, unresolved source looked like it could well be the manifestation of such an object. That there really is a supermassive black hole of $\sim 4 \times 10^6 M_\odot$, has now been proven beyond reasonable doubt through long-term monitoring and observation of the cluster of stars orbiting within arcseconds of the black hole, most notably the star S2 (S0-2 in Ghez et al., 2003) which has completed a complete 15-year orbit since the first monitoring observations in 1992 (Schödel et al., 2002; Ghez et al., 2003; Eisenhauer et al., 2005a).

Sgr A* is thus a source of intense observational and theoretical interest, since it provides an avenue by which to study the physics of accretion in the presence of extreme gravitational fields. However, it is unusually dim for a supermassive black hole (Rieke & Lebofsky, 1982). The spectral energy distribution of the radio source rises from radio towards submm wavelengths, but no steady emission can be detected above roughly 10^{12} Hz, implying that the spectral energy distribution (SED) turns abruptly around at this point (this feature has been named the 'submm bump'). The overall luminosity is far below (by a huge factor of $\sim 10^8$) that expected for a black hole accreting at the Eddington rate.

It was only recently that the source was discovered at all on the high frequency side of the submm bump, where it was found to exhibit strong flares in the X-ray (Baganoff et al., 2001) and in the near-infrared (NIR) (Genzel et al., 2003b). A steady quiescent state in the X-rays at very low luminosities was also found (Baganoff et al., 2003). The quiescent state has never been detected unambiguously in the NIR, nor has it ever been detected at mid-infrared (MIR) wavelengths for which only upper limits can be determined on either the quiescent state or possible flaring activity (see for example, Schödel et al., 2007).

Subsequent to the first detections of Sgr A* flaring in the X-ray and NIR, a number of flares have been observed in both IR and X-ray wavelengths. Multiwavelength campaigns co-ordinating telescopes across the electromagnetic spectrum have worked towards obtaining simultaneous observations.

Some general properties concerning the IR and X-ray flares that have emerged from those studies are:

1. IR/NIR flares occur on average ~ 4 times per day (see e.g. Figure 18, Eckart et al., 2006a), or between 30-40% of the observing time (Yusef-Zadeh et al., 2006a).

2. Strong X-ray flares occur on average ~ 1 per day (Baganoff, 2003). However, an enhanced rate of X-ray flaring can be observed within a time interval of roughly half a day (e.g. a bright flare followed by three flares of more moderate amplitude Porquet et al., 2008).

3. Every X-ray flare appears to be associated with a NIR flare, however not every NIR flare is associated with an X-ray flare (e.g., Hornstein et al., 2007).

4. X-ray and NIR flares occur simultaneously, with no significant delay (Eckart et al., 2004, 2006c; Yusef-Zadeh et al., 2006a).

5. Substructural variations with characteristic timescales of 15-25 minutes are seen in IR flares on a regular basis (Genzel et al., 2003b; Meyer et al., 2006; Eckart et al., 2006c;

Trippe et al., 2007).

6. Significant drops in flux are sometimes seen during X-ray flares (Baganoff et al., 2003; Porquet et al., 2003).

7. Polarimetric investigations of the flares in the NIR have shown that the source is significantly polarized (Eckart et al., 2006b) and that the polarization angle can swing in the tail end of the flare (Trippe et al., 2007; Meyer et al., 2006).

8. At high fluxes the flare has a constant blue spectral index in νL_{ν}^2 of $\beta = 0.4$ between 3.8 and 1.6 μm (Hornstein et al., 2007; Gillessen et al., 2006). For low fluxes it appears that the flare shows red νL_{ν} spectral indices (Ghez et al., 2005; Eisenhauer et al., 2005a; Krabbe et al., 2006) with a possible trend of spectral index with flux (Gillessen et al., 2006) although this is disputed (Hornstein et al., 2007).

9. The two brightest X-ray flares (Porquet et al., 2003, 2008) have been observed to have well constrained soft νL_{ν} spectral index values $\beta = 0.2 \pm 0.3$ and $\beta = 0.3 \pm 0.3$ calculated at a 90% confidence range (Porquet et al., 2008). While several fainter flares were observed, only a small number of photon index values has been reported; the latter exhibiting harder spectral indices (e.g., Baganoff et al., 2001). A re-analysis of XMM-Newton archival flares performed by Porquet et al. (2008) with a homogeneous data analysis shows that at low X-ray flux the spectral index is in fact not well constrained and a soft index as found for the two brightest flares cannot be excluded. Similarly, Mascetti et al. 2008 (submitted) analyses a co-added spectrum of all Chandra flares to date and reaches the same conclusion (i.e. that soft νL_{ν} indices are not excluded). Therefore, higher S/N spectra for individual weak/moderate X-ray flares are still required to establish whether all flares have similar spectral shape or not.

10. The X-ray flares appear unambiguously to be 'events', i.e. short, large amplitude outbursts followed by what looks like a perfectly flat baseline (Baganoff et al., 2003; Porquet et al., 2008). In the infrared, it is less clear whether this picture applies or whether the IR 'flares' are simply peaks within an underlying sea of variability with the characteristics of red noise. Similarly, it is debated whether the substructural features seen in IR flares correspond to a characteristic frequency of the system (a quasi periodic oscillation (QPO)), or whether it is caused by statistical fluctuations in a smooth, red noise power spectrum (Do et al., 2009a; Meyer et al., 2008).

Note that there are also many important results from observations at longer wavelengths, but since we are directly concerned with the IR and X-ray data we have obtained, we have not gone into them in this paper. The full results of our April 2007 multiwavelength campaign including the observations at radio and submm wavelengths will be presented in Yusef-Zadeh et al. (2009, in prep.).

The quiescent state of Sgr A* can be successfully described by either a radiatively inefficient accretion flow (or RIAF; see for example Yuan et al., 2003), or as arising from the base of a compact jet (Falcke & Markoff, 2000). Each of these models can describe the observed properties of the quiescent state with similar magnetic field strengths ($B \approx 30$ G) and electron energies

---

[2]Here and elsewhere in this paper we use β to denote the νL_{ν} spectral index, defined as $\nu L_{\nu} \propto \nu^{\beta}$.

($\gamma = E/mc^2 \approx 10$). The addition of Bremstrahlung emission from within the Bondi accretion radius ($R_{\text{Bondi}} \sim 1''$) explains the X-ray quiescent emission (Quataert, 2002).

The origin of the flare emission within either of these basic pictures is much less certain. The high degree of linear polarization of the flares at IR wavelengths points to a synchrotron origin, but the emission mechanism responsible for the X-ray flares is not known. In the analysis of the simultaneous IR/X-ray multiwavelength observations to date, inverse Compton scattering processes have been favored. Eckart et al. (2004) and Eckart et al. (2006c) explained the simultaneity and the observed fluxes of infrared and X-ray flares through the synchrotron self Compton (SSC) emission of a compact source component emitting primarily at mm/submm wavelengths, with the emission at IR wavelengths possibly due to a combination of synchrotron and SSC emission. In Yusef-Zadeh et al. (2006a), the IR and X-ray observations were interpreted within a picture where the X-ray emission was due to inverse Compton scattering of submm and IR photons involving populations of both submm-emitting and IR-emitting electrons. Liu et al. (2006a) and Yuan et al. (2003) also present models involving inverse Compton processes. Synchrotron models for the X-ray flare have been suggested by Markoff et al. (2001) and Yuan et al. (2003) and IR/X-ray synchrotron models by Yuan et al. (2004). Synchrotron models in general have been criticized due to the fact that the high energy electrons needed to generate X-ray synchrotron emission have very short cooling timescales (much shorter than the typical X-ray flare duration), requiring continuous injection in order to replenish the high energy population. However, this may not be such a disadvantage, and continuous injection is in fact a natural and reasonable expectation for the kinds of processes responsible for particle acceleration such as magnetic reconnection, turbulence and shocks.

Going beyond the emission process behind the flare, there are models which attempt to simultaneously describe the detailed properties at one wavelength, such as the hot spot model (Broderick & Loeb, 2005; Meyer et al., 2006; Trippe et al., 2007; Hamaus et al., 2009), or accretion instability models (Tagger & Melia, 2006; Falanga et al., 2008)

In this paper we present our multiwavelength observations and focus on constraining the emission mechanisms responsible for the simultaneous IR and X-ray flares we have observed. Although a full analysis of the detailed time-resolved SED evolution is beyond the scope of this paper, our high quality, full coverage, lightcurves in both L′-band and X-ray wavelengths offer the for the first time the opportunity to undertake detailed modelling of the time evolution of the flare SED, which may shed further light on the emission mechanisms and physical conditions/processes giving rise to a flare event.

Throughout this paper we adopt a Galactic Center distance of 8 kpc (Eisenhauer et al., 2003), and a black hole mass of 4×10^6 M$_\odot$ (Gillessen et al., 2009; Ghez et al., 2008) for which the Schwarzschild radius is $R_S = 1.2 \times 10^{12}$ cm. For the solar luminosity we used the value $L_\odot = 3.8 \times 10^{33}$ erg s^{-1}.

4.2 Observations

In this section we present IR/NIR (3.8, 2.1 and 1.6 μm), MIR (11.88 μm) and X-ray (2-10 keV) observations of Sgr A* taken in April 2007. In particular we focus on April 4, 2007, on which date a very bright flare was observed in both L′-band (3.8 μm) and X-ray simultaneous to the MIR observations.

4.2.1   IR/NIR Observations

The IR/NIR observations were taken at the VLT in Chile as part of a multiwavelength campaign (LP 179.B-0261) in April 2007, using the NAOS-CONICA instrument (Lenzen et al., 2003; Rousset et al., 2003) in imaging and polarimetric modes. We observed between 5:00 and 11:00 UT on April 1 to April 6 obtaining data in L′ (3.8 μm), Ks (2.1 μm) and H (1.6 μm) wavelength bands.

We subjected the raw data to a sky subtraction computed from jittered object images in the L′-band case, and from dedicated observations of a patch of sky devoid of stars $\approx 700''$ W and $400''$ N of the GC for the Ks and H band observations. This was followed by flat-fielding and a correction for dead/hot pixels.

Once we had reduced the set of images, the raw flux at the position of Sgr A*[3] in each image was determined via two independent methods: (i) aperture photometry, where the flux was computed as the sum of all pixels within a small aperture centered on Sgr A*, from which the sum of pixels (normalized by area) within a larger annular region surrounding Sgr A* was subtracted to remove background contamination; and (ii) PSF photometry, where we used StarFinder (Diolaiti et al., 2000) to automatically identify and extract PSFs from the reduced images, thereby obtaining source fluxes.

Finally, we calibrated the raw flux with the fluxes of nearby stars of known and stable brightness, and converted it to a physical flux. For the extinction correction we used the values $A_L = 1.8$, $A_K = 2.8$ and $A_H = 4.3$ (Genzel et al., 2003b).

For those observations taken in polarimetric mode, we added the fluxes obtained in ordinary and extraordinary images to obtain an integrated flux (for further details see Trippe et al., 2007).

The resulting lightcurves for the combined source Sgr A* + S17 are presented in Figure 4.1. Several weak flares are seen (labelled 1-4 and 6-7). On the night of 4 April and under good conditions (seeing $\sim 0.55 - 0.9$ and Strehl ratios $\sim 0.45 - 0.65$), a very strong flare was seen in L′-band at the position of Sgr A*, beginning just before 06:00 UT, April 4, and lasting for roughly 2 hours. We present the lightcurve of this flare in detail in Figure 4.2.

Since Sgr A* was confused with S17 on April 4 2007, S17 also contributes flux to the lightcurve shown in Figure 4.2. In addition, the quiescent state of Sgr A*, if it exists, is not well known so it is possible that the quiescent state and possibly other L′-band sources such as a small dust cloud close to Sgr A* (Clénet et al., 2005) also contribute to the minimum flux of Sgr A* on the night of April 4. It is also not clear from the lightcurve whether Sgr A* ever reaches a level of non-activity during our L′-band observations. If we take the mean of the group of points where the lowest flux for the night was recorded between $t \sim 295$ to 300 minutes, this leads to an upper estimate for the contribution of any nonvariable emission of 4.3 mJy.

The combination of the data quality and the strength of the flare activity make the April 4 flare presented here the best specimen of our entire dataset recording the L′-band activity of Sgr A* and spanning 2003 to 2007. The lightcurve shows very significant substructure on a timescale of ~ 20 minutes. This kind of substructure has been seen in previous Ks-band flares (Genzel et al., 2003b; Eckart et al., 2006b; Trippe et al., 2007), but is seen here for the first time in L′-band. This strengthens the case that the presence of substructure is a common feature of IR/NIR flares.

---

[3]confused in these observations with the star S17.
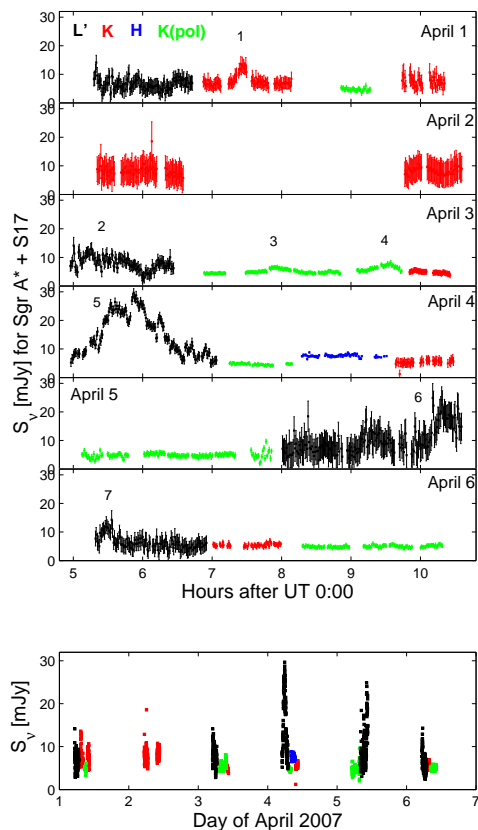
Figure 4.1 Lightcurve for Sgr A* + S17 for April 1-6 2007 IR/NIR observations with NACO at the VLT. Observations were taken at L' (black), Ks (red), H (blue) as well as in Ks-band using polarimetric mode (green). Several flare events are seen over the six nights of observations, labelled 1-7. Some nights show a more continuous level of variability (April 3), while on other nights there are long periods with no obvious variable emission. The L'-band flare from April 4 is the most significant event seen. A flare of equivalent strength in Ks band (given a colour of $\beta = 0.4$ in νL_ν) would reach $S_K \sim 20$ mJy. On April 5, another L'-band flare is seen under less favorable conditions which reaches $S_{L'} \sim 20$ mJy in L'-band.
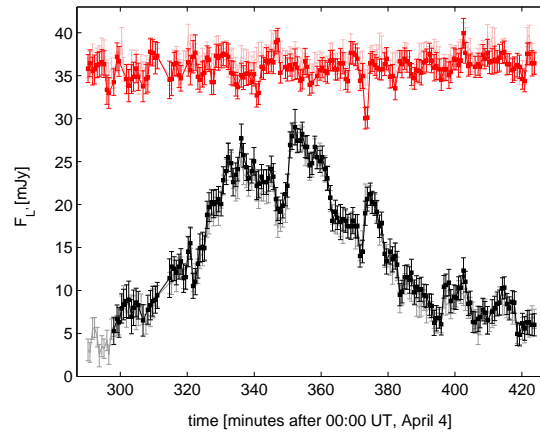
Figure 4.2 Extinction-corrected L′-band flux of Sgr A* on 4 April 2007, determined via PSF photometry (black data points) and via aperture photometry (grey data points). In red (PSF photometry) and light red (aperture photometry) is shown the flux of the nearby star S2 as a flux comparison, clearly demonstrating that the substructure is intrinsic to the Sgr A* source. S2 was confused at the time of observation with S13, and in the figure their combined flux is shifted upwards by 25 mJy. Sgr A* was confused with S17 and the flux shown also possibly has a contribution from a dust cloud as well as the unknown quiescent state of Sgr A*. The data are binned to a bin-width of 44.3s. The PSF photometry method only lists fluxes of sources detected with 3σ significance, which explains why the lightcurve derived by PSF photometry begins only at around ~ 300 minutes. We use the mean of these points with $t \lesssim 300$ minutes as an upper estimate of the background level (S17 + confused sources + quiescent state) upon which the flare emission is superimposed. If the minimum of the lightcurve is used instead, we obtain a background estimate of 2.4 mJy.

Limits on L′-band flaring activity ∼ 7-11 hrs UT.

On April 4 2007 we also obtained data in other wavelength bands (Ks-band polarimetry, H-band imaging and Ks-band imaging) for another ∼ 3.5 hours after the flare observed in L′-band (Figure 4.1). There was no obvious variability in these wavelength bands. We find that our measured Ks-band flux for Sgr A* + S17 of $S_K = 5.1 \pm 0.4$ mJy is consistent with the measurement of Do et al (2008) for S17 alone (5.5 mJy, dereddened according to $m_K = 2.8$ as assumed in this paper; no error was given). It is also consistent with our own past measurements of S17's magnitude ($m_K = 4.8$ mJy), although our error on this value is very large and on the order of 2 mJy. The H-K color of the combined Sgr A* + S17 source is $\beta = 2.6 \pm 0.7$, consistent with that of a pure stellar source ($\beta = 3.0$). From this and the lack of significant variability in the emission we would conclude that in H and Ks band the emission is dominated by S17. We note that in deconvolved images of this dataset we *do* see an elongation of the source in Ks band, and resolve two distinct sources in H band. Of these two H-band sources we can not be sure whether the source coincident with Sgr A* is stellar (e.g. from faint unresolved S-stars surrounding the black hole) or whether it might be quiescent/flaring emission. Due to the close proximity of the sources (only 3 pixel separation) it was not possible to determine the Ks-band fluxes of each source accurately.

In L′-band the lowest measured luminosity lies above the extrapolation of the (Sgr A* + S17) H-K measured color and we can conclude that within the timespan of our L′-band observations we did not reach the flux level of S17, which would be expected at ∼ 1 mJy. The remaining flux we see may be due to a further contamination of the L′-band flux by a confused source (e.g. a small dust cloud known to be an L′-band source nearly coincident with Sgr A*, ∼ 4.7 mJy Clenet et al 2005, although this seems unlikely given the high flux), or it might also be due to the fact that the flare activity never ceased within our L′-band observation time interval. Since flares are redder than the stars, we can not rule out that some low-level flaring continued to occur after ∼ 430 minutes while we observed in Ks- and H-bands.

To make some estimation of the L′-band flux during the time interval within which we observed in Ks and H bands we must extrapolate from our Ks-band measurements, which introduces large uncertainties. We can reasonably assume that any flaring emission was below $S_K \sim 2.1$ mJy during the Ks and H-band observations (our lower limit on the flux of S17 is 3 mJy; note this is also consistent with extrapolating the flux of the deconvolved, separated source in the H-band images to Ks-band with a slope of $\beta = 3$). Although the flare color at low flux levels is not well established, if we take a flare color of $\nu L_\nu = 0.4$ we can estimate that the combined source of Sgr A* + S17 should not have been at a flux level higher than 4.7 mJy in L′-band during this time. However, if the flare were redder at low flux levels or if some flux is contributed from the dust cloud near Sgr A* then the limit on the flux level could be higher. We obtain an upper limit of 9 mJy if we add the lowest flux detected during the L′-band observations (4.3 mJy), using it as an upper limit on the magnitude of any nonvariable contamination.

4.2.2   X-ray Observations

On the 4th of April 2007, the VLT observations described in Section 4.2.1 overlapped with those of XMM-Newton. The observations and data reduction of the X-ray flare are published by Porquet et al (2008), and will not be repeated here. The X-ray lightcurve is presented in Figure 4.3, where it is compared with the L′-band lightcurve.

The X-ray flare was very bright. The 2-10 keV spectrum of the flare showed a soft spectrum: a

power law fit correcting the underlying model for dust scattering and absorption gives a power law slope of $\Gamma = 2.3 \pm 0.3$ (error bars given at the 90% confidence level), equivalent to a νL_ν spectral index of $\beta = -0.3 \pm 0.3$. The bright flare observed on April 4th (labelled #2 in Porquet et al., 2008) is the second brightest flare observed so far from Sgr A* with an amplitude of about 100 compared to the quiescent state. Porquet et al. (2008) show that this flare and the brightest X-ray flare observed in October 2002 (Porquet et al., 2003) have similar light curve shape, duration, and spectral characteristics (photon index).

4.2.3 Mid-Infrared Observations

VISIR, the VLT Imager and Spectrometer for the mid-infrared, mounted on the ESO/VLT telescope Melipal (UT3) at Paranal, Chile (Lagage et al., 2004; Pantin et al., 2005), observed the Galactic Center from 2007-04-04 05:29:00 to 2007-04-04 10:34:00 (UT). We collected the data with the imaging `PAH2_2` filter on, at 11.88 ± 0.37 μm in the atmospheric window "N". The Small Field mode (`SF`) was employed, resulting in a field of view of 256×256 pixels (19.2 arcsec^2), each pixel corresponding to 0.075 arcsec^2.

We performed the calibration of the `PAH_2` filter on 2007-04-04 05:16:24 (UT) with a 109.9s observation of the standard star HD 102461 (9.237 Jy in the `PAH2_2` filter; Cohen et al., 1999).

The basic 'chopping and nodding' technique was applied to acquire the data, which were then reduced with the standard VISIR pipeline[4]: this involved flatfielding, bad pixel correction and combination of a stack of chopped and nodded frames to produce a final set of 79 consecutive images.

We determined the position of Sgr A* using the precise positions of the SiO maser sources IRS 7, IRS 9 and IRS 10EE, distributed about Sgr A* (Reid et al., 2007). No point source at the position of Sgr A* is detected in either the individual images or the collapsed image of the entire night. We also performed a Lucy-Richardson deconvolution with HD 102461 as PSF with again no source detection. The flux from a box of 0.375 arcsec^2 centered on the position of Sgr A* is constant with an average value of 123 ± 6 mJy. This flux may be attributed to the weak and diffuse dust ridge on which Sgr A* lies, and our measured value is consistent with previous VISIR observations (Eckart et al., 2004; Schödel et al., 2007).

To determine an upper limit of the brightness of the simultaneously observed flare, we subtracted an average image of the quiescent phase (12 images from 07:17 to 08:00) from an average image of the flaring phase (12 images from 05:30 to 06:13[5]). We included a slight shift in the relative positions (less than half a pixel) of the images, degraded the mean images with Moffat functions to mimic the slight differences of atmospheric conditions between them, and finally destriped the subtracted image. Over a region of ~ 3 arcsec^2 centered on Sgr A*, north of the minispiral, the subtracted image displays a relatively flat background.

To quantitatively estimate our detection limit, we proceeded by simulating an artificial flare in the data. We included a weak point source of a given flux (with VISIR's PSF) at the position of Sgr A* in the substracted image. We increased the point source's flux until it was detected at a significance of 3σ and took this value as an upper limit on the flare's mean flux. We thus estimate that Sgr A* could not have been brighter than ~ 12 mJy at 11.88 μm (3σ, not dereddened). Note

---

[4]see http://www.eso.org/instruments/visir/

[5]Note that VISIR observations started 5 min after the beginning of the X-ray flare, which was from 05:25 to 06:13
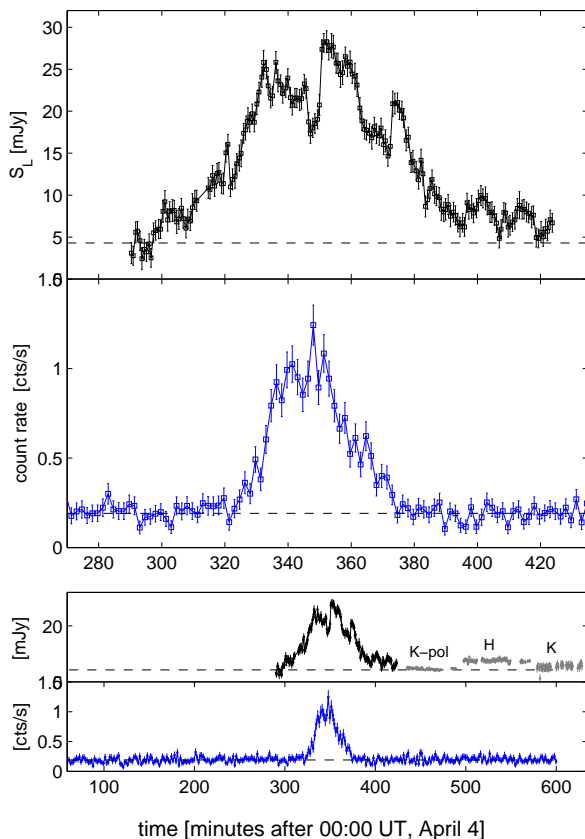
Figure 4.3 Comparison of the L'-band and 2-10 keV lightcurves. The top two panels show the two flares over the period of L'-band observations. In the lower two panels, a larger time interval is shown. We also show subsequent data taken in other wavelength bands (Ks-band polarimetry, H-band imaging, and Ks-band imaging) subsequent to the L'-band flare indicating that the flare activity ceased in both wavelength bands after roughly 4:00 UT. In the same night of observations three more X-ray flares were seen (Porquet et al 2008); the first of these started at UT 11:32 (692 minutes), i.e. roughly an hour after the last of the NIR observations. The dashed lines indicate our estimates of the background levels (i.e. emission that is not flaring emission) at each wavelength. In the case of the IR lightcurve this may be an overestimate.

that this value is compatible with VISIR's empirical sensitivity at this wavelength: $7 \text{ mJy}/10\sigma/1$ hr (median value for different atmospheric conditions).

The value of the extinction correction in the MIR depends critically on the strength and shape of the silicate absorption feature at $\sim 9\mu$m. The values in the literature are published as ratios relative to A_K or A_V, so we use the value $A_K = 2.8$ mag ($A_V = 25$) mag to ensure consistency across our multiwavelength observations. The closest extinction measurement to our observation wavelength, $\lambda = 11.88\mu$m, was made by Lutz (1999) for a wavelength of $\sim 12.4\mu$m. We consider three theoretical models (Chiar & Tielens, 2006; Draine & Lee, 1984; Roche & Aitken, 1984) for the shape of the silicate profile in the region, to allow us to extrapolate the value measured at 12.4μm to 11.88μm. These models each use different sources as template profiles but are all very similar in slope around 12 μm and result in very similar values of extinction when normalized to the Lutz (1999) value at 12.4 μm. The thus determined extinction value is $A_{11.88\mu\text{m}} = 1.7 \pm 0.2$ mag. With this value, the dereddened 3σ upper limit on emission from Sgr A* during the flare is $F_\nu^{\text{MIR}} \sim 57$ mJy.

4.3   Results

4.3.1   Simultaneity of infrared and X-ray flare

We have obtained complete, fully sampled lightcurves in L′-band and X-ray. The X-ray lightcurve showed no other events during either a ~ 15 hour period before and ~ 5 hours after the bright X-ray flare. In the IR/NIR, in the remaining observations of about $3\frac{1}{2}$ hours following the L′-band flare, there were no other flares or obvious variable emission above a level of $S_K \approx 2.4$ mJy (implying $< 12\%$ the equivalent Ks-band flux of the peak of the L′-band flare, using $\beta = 0.4$). We translated this to a more conservative limit (see Section 4.2.1) in L′-band of $S_{L'} < 9$ mJy ($< 32\%$ the peak L′-band flare flux). At least on this occasion, both infrared and X-ray emission can thus be best characterized as isolated 'flare' events.

From a correlation analysis, the L′-band and X-ray flares are found to be simultaneous to within ~ 3 minutes. In particular we do not see any significant delay or asymmetry in the longer wavelength emission relative to the peak of the X-ray flare, thus excluding that adiabatic expansion of an initially optically thick blob plays a role in the infrared and X-rays.

4.3.2   General Lightcurve Shape

This multiwavelength observation allows us to make the most detailed lightcurve comparison so far, of simultaneous IR and X-ray flares from Sgr A*. From the comparison of the two lightcurves shown in Figure 4.3 it appears that the L′-band flare begins first. The L′-band lightcurve rises before any significant X-ray emission is seen, and L′-band emission remains after the X-ray emission has subsided. It appears that the two events have different durations from one another, and that the infrared event lasts longer overall than the X-ray event.

Taking the uncertainties on the background levels into account, we measure FWHM durations for each (background-subtracted) lightcurve of $\text{FWHM}_{IR} = 66 \pm 8$ and $\text{FWHM}_X = 28 \pm 0.5$ minutes. Thus we find that the FWHM of the L-band flare is ~ 2 times that of the X-ray flare.

4.3.3   Substructure

One very striking feature of the L′-band lightcurve is the substructural variations seen on a timescale of ~ 20 minutes. The variations in flux are large: up to $\sim 30\%$ the peak flux. There are no apparent features that would correspond to these in the simultaneous X-ray lightcurve.

   Although the X-ray lightcurve has lower SNR than the L′-band lightcurve, the error bars are only on the order of $\sim 10\%$ the peak flux, and thus cannot hide substructures as large as those in the L′-band lightcurve. From this we conclude that the lack of substructure in the X-ray lightcurve is not due to lower SNR, and that this property is in fact intrinsic to the simultaneous IR/X-ray lightcurves.

4.3.4   Shortest time-scale variations

In the L′-band lightcurve, in particular at $t \sim 350$ minutes but also near to $t \sim 370$ and 395 minutes, very rapid changes in flux (factors 120% to 170%, significance $> 3\sigma$) are observed within a very short timescale, $\Delta t < 47$ seconds.

   Such short term variations place a limit on the size of the flaring source, or at least the size of the part of the source providing the sudden change in flux (which is a significant fraction, $\sim 30\%$, of the total flux). Since such variations cannot propagate within the source faster than the speed of light c, the source size R_F is immediately constrained to be

$$R_F < c\Delta t = 1.2 R_S.$$

   A caveat to this constraint is that we have not considered various relativistic factors; given the small size obtained and the fact that we think the flare might occur at very small radii in the accretion flow, relativistic effects might be an important factor in influencing the time variability of the source. Relativistic beaming near the event horizon is a possible source of magnifying the amplitude of variations due to an underlying spatial structure in the infrared emission. Such beaming effects could be considerable (Hamaus et al., 2009; Broderick & Loeb, 2005).

4.3.5   Power Spectra

Whether or not the substructures seen in the L′-band lightcurve are indicative of a QPO or are merely spurious peaks in a red noise process is a matter of current debate (e.g. Do et al., 2009a; Meyer et al., 2008). Since the putative QPOs inevitably turn out to be too weak to stand a significance test from a single observation night's worth of data, we turn our focus to longer timescales. H-band and Ks-band polarimetric data that were taken following the L′-band measurements show no evidence of any variable emission, and this clearly holds an implication for the variability behaviour of the source on longer timescales.

   Figure 4.4 shows the periodogram of the L′-band data compared with that of the X-ray lightcurve. We use the ordinary periodogram with the RMS-squared normalization (see, for example Uttley et al., 2002) which allows us to compare lightcurves taken with different instruments (and here at different wavelengths). For a consistent comparison between the IR and X-ray variability we took the mean from the same time interval, i.e. the maximum time overlapping time interval of the IR and X-ray observations. For timescales $\lesssim 130$ minutes (frequencies > 0.008 min^{-1}) we show the power spectrum of the L′-band data only. We use our limits on the variable
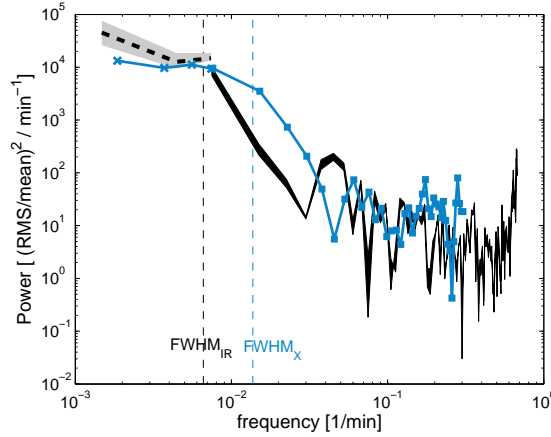
Figure 4.4 Power spectra of the L′-band (black) and X-ray (blue) lightcurves. Our constraint on the periodogram at low frequencies from Ks and H band data is shown in gray (with the interval mean shown as black dashed line). The RMS-squared normalization was used, where the mean of the IR and X-ray lightcurves was taken from the same time interval. A peak is seen around the 20 min timescale (~ 0.04 min^{-1}), while there is no corresponding peak in the X-ray power spectrum. The two dashed lines indicate the corresponding FWHM frequency for the Fourier transform of a Gaussian given the FWHM durations of the IR and X-ray flares.

emission in Ks and H bands to constrain the periodogram at lower frequencies. Some uncertainty in the normalization of the IR power spectrum comes about through our uncertainty in the mean value given the extrapolation from Ks-band to L′-band. There is an apparent peak at ~ 20 minute timescales. Whether it is a real QPO or the spurious peak of a red noise spectrum, it is noteworthy that the putative QPO peak of the L′-band data has no corresponding feature in the X-ray power spectrum. This is consistent with our observation that the substructures of the IR lightcurve are not present in the X-ray lightcurve, which is comparatively smooth.

At low frequency we also see the difference in widths of our lightcurves; the power spectrum of the X-ray lightcurve resembles a Gaussian at low frequencies which is as expected for the power spectrum of a single Gaussian-like flare event. The power spectrum of the IR lightcurve resembles a narrower Gaussian, again expected from the fact that the IR lightcurve was of longer duration than the X-ray lightcurve. We note then that the clear flattening of the power spectrum towards low frequencies again suggests that the IR flares are discrete events.

4.3.6   Spectral Energy Distribution

The 'flare state' SED for the observations of Sgr A* on April 4, as determined by our multiwavelength observations, is shown in Figure 4.5.

For the νL_ν value at L′-band we computed the mean of the extinction corrected, background subtracted L′-band flux. We chose to take the mean value rather than the peak value since the MIR limit and X-ray spectra were both determined as averages over the flare interval. The error in the L′-band data point is computed as the standard deviation of the lightcurve.
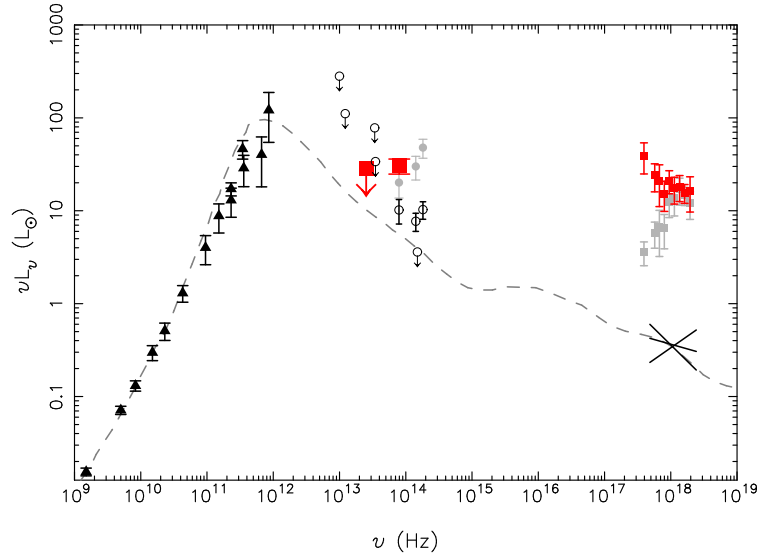
Figure 4.5 The Spectral Energy Distribution of Sgr A*: in black are radio to submm measurements of the quiescent state (Markoff et al., 2001; Zhao et al., 2003). Note that these measurements are time averaged measurements and the errorbars include variable emission of up to 50%. As open black circles are shown 30 μm, 24.5μm and 8.6 μm upper limits taken from Melia & Falcke (2001), the upper limit at 8.6 μm from Schödel et al. (2007) and the limit on the quiescent state at 2 μm from Hornstein et al. (2002). The quiescent state values from Genzel et al. (2003b) are shown as the open black circles with errorbars, and the flare values from the same paper as gray filled circles. The X-ray quiescent state is shown as the black bow-tie (Baganoff et al., 2003). The dashed line shows a model for the quiescent state (Yuan et al., 2003). Our new measurements for the SED of a flaring state of Sgr A* are shown in red: (i) the MIR (11.88 μm) upper limit is shown as the downwards-pointing arrow. The MIR upper limit is determined over an interval 05:30 to 06:13 (see discussion in Section 4.2.3). (ii) The L′-band measurement is shown as the red square with errorbars. This corresponds to extinction corrected, background subtracted mean value of the L′-band observations, 19.1 ± 3.6 mJy (in this case we used the minimum of the lightcurve, 2.4 mJy as the background estimate). Since the MIR observations did not start until 5:30 (approximately half an hour after the onset of the NIR flare), the mean was computed over the MIR time interval rather than the entire L′-band flaring interval. Also shown next to the L′-band data point is how the L′-band measurement would continue into Ks and H band with a slope of 0.4, characteristic of the L′-H slope of a number of 'bright' observed flares in the literature (Hornstein et al., 2007; Gillessen et al., 2006) and also consistent with the slope of the peak flare values of Genzel et al. (2003b). (iii) Two possible X-ray spectra are shown, neither of which is model-independent. The red points indicate the power law fit, of Porquet et al. (2008), while the grey points show the blackbody fit of the same paper. The X-ray spectrum was scaled by a small factor since it incorporated data from an extra five minutes before the MIR observations began.

For the X-ray data, it is difficult to show an intrinsic, dust and absorption-corrected X-ray spectrum without the assumption of a model. This is because the inversion of a raw counts/channel X-ray spectrum is generally non-unique and unstable to small changes in the counts/channel spectrum (Arnaud, 1996). To determine the best fitting spectrum, a model is calculated and 'folded', or convolved with the instrumental response after which the folded model spectrum is compared to the observed counts in each channel. Once one has found a best fit, the process can be reversed for the best fitting model and one obtains an intrinsic, but model dependent, spectrum.

Because of this, we can not show a single, model-independent X-ray measurement on the SED for the April 4 flare. Instead, we show two possible X-ray spectra as obtained by Porquet et al. (2008) (i) assuming a power law shape, with $\Gamma = 2.3 \pm 0.4$ and $N_H = 12.8^{+2.5}_{-2.1} \times 10^{22}$ cm^{-2} (at the 90% confidence level, using the χ^2 statistic; see Appendix B in Porquet et al., 2008), and (ii) assuming a blackbody model, with parameters $N_H = 7.3^{+1.6}_{-1.3} \times 10^{22}$ cm^{-2} and $kT = 1.5^{+0.1}_{-0.1}$ keV. The blackbody fit had the lowest N_H of the models investigated in that paper. Both models show a soft spectral index above $\nu \sim 10^{18}$ Hz. We scaled the X-ray data, which was determined over the full X-ray flaring interval, by a factor 0.95 to account for the fact that the interval over which the MIR upper limit was calculated was shorter by 5 minutes (the scaling factor was determined as the ratio in fluxes between these two intervals).

In both L'-band and X-rays, there is a substantial increase in flux above the quiescent level. The absence of any detectable emission at 11.88 μm implies that the flare emission spectrum must rise from 11.88 μm to 3.80 μm. This appears consistent with a (νL_ν) spectral index of $\beta = 0.4$ (Hornstein et al., 2007; Gillessen et al., 2006; Genzel et al., 2003b).

The rise in νL_ν from the MIR towards NIR wavelengths suggests that the population of electrons producing the L'-band flare must have a different distribution of electron energies to those in the submm bump. This might be an power law tail of transiently accelerated electrons, for example, or a small group of electrons heated to a high temperature. What this observation shows is that a NIR flare cannot be due to a small change in *overall* properties of the submm bump (such as, for example, a global increase in magnetic field which temporarily increases the emitted synchrotron emission of the quiescent state). The flare event must involve only a small fraction of the quiescent state electrons, either in some kind of acceleration process that acts globally but inefficiently within the accretion flow, or via a more efficient but very localized acceleration process. As mentioned in Section 4.3.4, the short time scale variability of the source also points towards a localized event.

4.4 Modelling the flare state SED of Sgr A*

We studied the flare state SED of Sgr A* under four simple SED models. These models explore different emission scenarios for the IR/X-ray flare and correspond to scenarios where the IR and X-ray flares are due to synchrotron and inverse Compton emission mechanisms. For the fitting of the SED models to the data we use the X-ray spectral fitting program XSPEC (Arnaud, 1996). To incorporate our infrared data points we add an extra data channel with the L'-band extinction corrected flux; the instrumental response for this data channel is an identity matrix. The four XSPEC models we used are:

1. `icmodel`: IR emission is synchrotron emission by transiently heated/accelerated electrons;

X-ray emission is due to the inverse Compton scattering of submm photons from the 'quiescent' population of electrons by the population of electrons producing the IR emission.

The seed photon spectrum comes from the quiescent population of electrons and its spectrum and total luminosity is fixed (we use the model spectrum of Yuan et al., 2003). R_Q, the size of the region containing the quiescent state (submm-emitting electrons) electrons is a free parameter and controls the photon density of submm photons available for inverse Compton scattering.

The IR synchrotron emission is modelled based on a thermal distribution of electrons. There are three parameters that pertain to the transiently heated population of electrons producing IR synchrotron emission: B, the magnetic field, θ_E, the dimensionless electron temperature (θ_E denotes the typical energy γ of the electron distribution; it is equal to kT_e/mc^2, where T_e is the temperature of the thermal electron distribution), and N, the total number of IR synchrotron emitting electrons.

2. `sscmodel`: IR emission is synchrotron emission by transiently heated/accelerated electrons; X-ray emission to IR/NIR photons of the transiently heated/accelerated (flare) electron population that are inverse Compton scattered by the same population (i.e. SSC).

   The IR synchrotron emission is again modelled based on a thermal distribution of electrons. This IR synchrotron emission can be again computed from the parameters: B, magnetic field, θ_E, the dimensionless electron temperature (the typical γ of the electrons, see `icmodel`), and N, the total number of IR synchrotron emitting electrons.

   In this model it is the parameter R_F, the size of the region containing the flaring (IR-emitting) electrons that controls the photon density of the seed photon spectrum.

3. `powerlaw`: IR emission is synchrotron emission from a power law energy distribution of accelerated electrons. The parameter of interest in this model is the particle index of the power law electron distribution, p, i.e. $N(\gamma) \propto \gamma^{-p}$.

4. `powerlawcool`: IR emission is again synchrotron emission from an electron distribution with continuous injection of power law electrons and the addition of synchrotron cooling. Parameters of this model are p, the particle index of the injected electron spectrum, and the magnetic field B, which determines the cooling time of electrons and thus the energy/frequency at which the cooling break occurs.

The two models `icmodel` and `sscmodel` were developed especially for this work, while `powerlawcool` was a simple adaptation of the existing XSPEC model `powerlaw` to incorporate the cooling break. Specific details of the `icmodel`, `sscmodel` and `powerlawcool` models are listed in the Appendix.

For each model we also take into account the effect of photoelectric absorption and dust scattering on the X-ray spectrum via the XSPEC routines `scatter` and `wabs` (for more details, see Porquet et al., 2008). These effects were not applied to the NIR data. For the dust scattering (`scatter`), we fix $A_V = 25$ to match the dust extinction corrections used for the L'-band and MIR data. For photoelectric absorption (`wabs`) we allow the parameter N_H to be determined.

As an extra constraint, we add an extra data point at H-band (1.65 μm) which corresponds to a constraint on the νL_ν slope from L'-H band of $\beta = 0.4 \pm 0.2$. We find that adding this constraint generally results also in models which do not violate the MIR 3σ upper limit. We ran models also without this extra constraint and very similar best fit values were obtained.

Table 4.1.   Models: Fit Parameters

Parameter	Fit to Mean Fluxes & NIR spectral index							
	icmodel		sscmodel		powerlaw		powerlawcool	
N_H [$\times 10^{22}$ cm^{-2}]	11.7	$(9.9, 14.3)$	11.5	$(9.7, 13.7)$	11.5	$(10.6, 12.7)$	12.4	$(11.0, 12.1)$
B [Gauss]	210	$(30, 2900)$	6000	$(2200, 7900)$	< 0.1, or > 60		6.1	$(0.1, 60)$
θ_E [$kT_e/m_e c^2$]	140	$(50, 210)$	11	$(9, 16)$	-		-	
N_e [$\times 10^{40}$ electrons]	4.7	$(0.2, 130)$	1.5	$(0.7, 4.2)$	-		-	
R_Q [R_S]	0.046	$(0.001, 0.27)$	-		-		-	
R_F [R_S]	> 0.02		0.0013	$(0.0009, 0.0020)$	-		-	
p	-		-		2.88	$(2.82, 2.94)$	2.4	$(2.1, 3.1)$
χ^2 / d.o.f.	70.1 /74		69.9 /74		72.4 /77		70.4/76	
reduced χ^2	0.95		0.94		0.94		0.93	
Violates 3σ MIR upper limit?	No		No		Yes		No	

Note. — Summary of best fit parameters for different scenarios: synchrotron + submm IC (`icmodel`), synchrotron + NIR SSC (`sscmodel`), simple power law (`powerlaw`), power law with cooling break (`powerlawcool`). In each case a NIR νL_ν slope of $\beta = 0.4 \pm 0.2$ was enforced in order to add enough constraint to the parameters. We found that models which violated the NIR slope by $\gtrsim 2\sigma$ usually violated the 3σ MIR limit also. Listed is also whether the model violates the MIR limit. Next to each value we provide the 90% confidence interval for each parameter.

Table 4.1 lists the parameters of the fitted models. Figure 4.6 shows the SED corresponding to the best fitting case for each model. In the next subsections we go through each model in detail.

4.4.1   `icmodel`: inverse Compton scattered submm bump photons

A best fit model for the case of submm photons scattered by IR-emitting electrons is shown in Figure 4.6. The model is a satisfactory fit to the data. The typical electron energies involved appear reasonable ($\gamma \sim 140$). However, the magnetic field strength of 210 G is high compared to that expected for the inner regions of the accretion flow ($10 - 30$ G), and the parameter R_Q has a best fit value of 0.046 R_S, which as we will argue is an unreasonably small size to contain the quiescent state of Sgr A* (stated another way, it corresponds to a much higher photon density of submm photons within the flaring region than can be expected).

To understand whether the small value of R_Q is really 'too small', we must be sure of how the parameter R_Q should be interpreted. We note that R_Q is in fact constrained through the quiescent photon energy density required to produce X-ray emission of the amplitude that we see in the X-ray flare. Since photon density is defined through $U_{ph} = L/cA$, with A the surface area of the region emitting the luminosity L, we see that R_Q can be interpreted as a constraint on the surface area of the (quiescent) emission region.

Thus the true quiescent region's geometry must have a surface area equivalent to the surface area of a sphere of radius R_Q in order to reproduce the required photon density. For example, a torus situated at the last stable orbit, $R_{\mathrm{LSO}} = 3R_S$ would have an equivalent surface area to our best fit R_Q for a ring thickness of 2×10^{-4} R_S: extremely thin.

New observations of the size of Sgr A* at 1.3 mm, (Doeleman et al., 2008) approaching the peak of the submm bump, suggest that the quiescent emission region may not be centred on the black hole. The reason for this is the fact that the measured size for Sgr A* at 1.3mm is smaller than the minimum apparent (gravitationally lensed) size allowed for an object very near a black hole. If the quiescent emission region is indeed offset from the position of the black hole then we no longer require an extremely thin ring containing most of the quiescent region electrons. However, this still does not solve the size issue: at the 90% confidence level, the largest value of R_Q that is compatible with the data, $R_Q = 0.27$ R$_S$ (0.54 R$_S$ in diameter) is still far below the measured FWHM size at 1.3 mm of ≈ 3.7 R$_S$.

Another issue stems from the fact that our model does not take into account a stratified region (i.e. the property that the observed size changes with wavelength, Bower et al., 2004; Shen et al., 2005) in the calculation of the photon density from L_{submm} and R_Q. Within the true (non-homogeneous) quiescent source the local density of quiescent photons will change with position. It may be more realistic, rather than to input the photon density via the variable parameter R_Q, to input the known photon density of a known model for Sgr A* which satisfies all the observations including the size measurements. As a demonstration of how we can implement this we again take the model of Yuan et al. (2003, see Figure 4.5) for which we have obtained tables of the quantity $n(\nu, R)$ at different radii R. This model has been shown to predict sizes at 3.5 and 7 mm consistent with those observed (Yuan et al., 2006).

Implementing this model, the free parameter replacing R_Q is the radial position of the flare from the the central black hole, r_{pos}. This position will determine the local photon energy density that is to be inverse Compton scattered by the flare electron population. When we incorporate
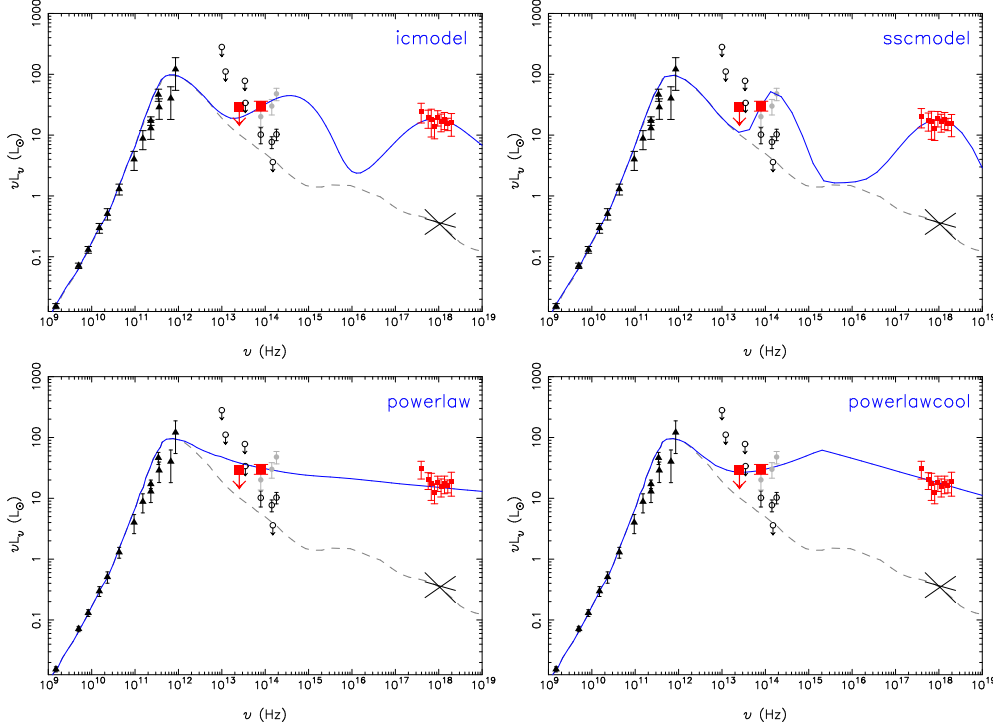
Figure 4.6 The best fits of the four XSPEC models for the April 4 flare IR and X-ray data. The X-ray data points are the unfolded spectrum for the given model (blue solid line); only the PN unfolded spectra are shown, with the data points binned for plotting purposes. (i) `icmodel`: The solid blue line shows the best fit IC model for the fit constraints of the April 4 flare, which satisfies the MIR limit and the NIR spectral index. The dashed blue line shows the best fit model holding the magnetic field fixed at B=30 G. This model violates the NIR spectral index and comes close to violating the MIR upper limit. It does however allow a larger size for the quiescent region, $R_Q = 0.27\ R_S$. This is however still far from the size/photon densities expected from size measurements of Sgr A*. (ii) `sscmodel`: Best fit SSC model. In this case the magnetic field and density are extremely high. The source becomes self-absorbed in the NIR, and the spectrum shows strong curvature from L′ to H-band. (iii) `powerlaw`: Best fit power law model. This model violates both MIR limit and NIR spectral index. (iv) `powerlawcool`: A more feasible synchrotron model with a cooling break. This model corresponds to the steady state solution for a system with a constant injection of power law electrons where the energy loss of the electrons due to synchrotron emission is taken into account.
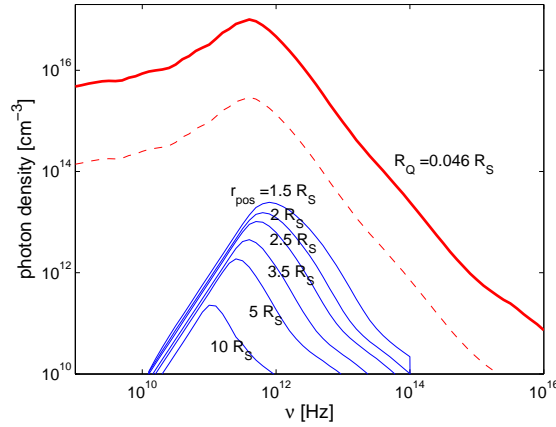
Figure 4.7 Comparison of the photon density at each frequency in (i) the best fit IC model with $R_Q = 0.046R_S$ (red) and (ii) different radii between 1.5 R_S and 10 R_S in the Yuan et al. (2003) model (blue). The dashed red line shows the the photon density spectrum for $R_Q = 0.27$, at the 90% confidence level for the parameter R_Q. The photon densities of Yuan et al. (2003) are in general 2 to 3 orders of magnitude too low, which shows why there is no well fitting IC model for the multiwavelength observations of the April 4 flare, given the photon densities of the Yuan et al. (2003) model.

the model's photon density into our inverse Compton code however, we find it difficult to find a reasonable fit for any r_{pos}.

One can understand why this is through Figure 4.7, which shows the energy density spectrum for (i) our simple 'one-size' models, for the best fit R_Q as well as a $\sim 3\sigma$ upper limit (i.e. corresponding to the lowest energy density spectrum allowed to produce acceptable X-ray IC scattering) compared with (ii) the energy density spectra for various inner radii of the Yuan et al model. As we can see, the photon density in the model is just too low over the entire frequency range to reproduce a bright, soft, X-ray flare via inverse Compton scattering.

Finally, although we were fitting an IC model to the flare, we must not forget about the fact that the electrons producing the NIR and IC emission must also be producing SSC emission. In fact, assuming the IC scenario to be the cause of the X-ray flare, we can put a lower limit on the size of the flare emission region R_F, by requiring the *absence* of an SSC contribution. To estimate this, we slowly varied R_F from its maximum value (R_Q) and observed at which point SSC emission began to overwhelm the IC X-ray emission[6]. We found that the flare region must be more than 0.02 R_S in size. This would imply a density of $n_e \lesssim 8 \times 10^8 \mathrm{cm}^{-3}$, which could be compatible with the kinds of densities ($n_e \approx 10^7 \mathrm{cm}^{-3}$) expected for the inner regions of an accretion flow near Sgr A* (Yuan et al., 2003)

---

[6]For the electron energies of our IC models, the SSC emission peak always occurred higher than X-ray frequencies, so the SSC spectrum had a hard νL_ν spectral index and is not a valid solution.

4.4.2 `sscmodel`: inverse Compton scattered NIR flare photons

The critical frequency for synchrotron emission (ν_c, the frequency at which a synchrotron-emitting electron emits most of its energy, and thus the energy at which the νL_ν spectrum turns over, see Section 4.6.1) is linear in B and quadratic in γ. Thus to obtain an SSC peak below 10^{18} Hz the electrons must have very low energies of $\gamma \approx$ 10-15. If the electrons were to have such low energies, it follows that a very large B is needed to produce a synchrotron peak above NIR frequencies so that an increasing νL_ν spectral index is observed in the NIR.

Thus it makes sense that our best fit SSC model, shown in Figure 4.6, corresponds to low electron energies and high magnetic field strength. The magnetic field strengths required are enormous, a factor of $\gtrsim 200$ greater than the typical magnetic fields of the quiescent state. At the same time, a dramatic decrease in the ratio of θ_E/B will have the effect of suppressing the SSC emission. Accordingly the density required from the small size, $n_e \approx 9 \times 10^{11} \mathrm{cm}^{-3}$, is equivalent to a density enhancement on the order of 10^4 above densities typical for the inner regions of the accretion flow and is also unrealistic. The high densities required even have the result that the synchrotron spectrum at IR/NIR wavelengths becomes self-absorbed. The self-absorption results in a very steep spectrum at IR wavelengths, and it shows significant curvature. Overall, due to the extreme physical conditions required to create the observed X-ray emission via SSC, we rule it out as the emission process behind the April 4 X-ray flare.

4.4.3 `powerlaw`: single power law synchrotron emission

We have found that neither the IC nor SSC scenarios are entirely satisfactory as explanations for the simultaneous observations of April 4. Therefore, it is worthwhile to investigate other possible scenarios for the production of the X-ray flare. One such possibility is that both IR and X-ray flares are synchrotron emission.

A power law energy distribution of electrons

$$N(E)dE \propto E^{-p}dE$$

in the presence of a magnetic field, will create a synchrotron emission spectrum

$$\nu L_\nu \propto \nu^{(3-p)/2}.$$

While the `powerlaw` model gives a reasonable fit to the L$'$-band and X-ray data, it violates the MIR limit and gives a soft νL_ν spectral index in the NIR. This model is also unrealistic since for reasonable magnetic field strengths $B \approx 10-30$ G we expect electrons within the energy range of our power law distribution to have very short cooling timescales. Either very low ($B < 0.1$G) magnetic fields are needed or very high ($B > 60$G, together with a very flat spectrum of injected electrons $p \sim 1.9$) to prevent a cooling break occurring between IR and X-ray wavelengths (i.e., this motivates our next model `powerlawcool`). We can thus definitively rule out this scenario.

4.4.4 `powerlawcool`: power law synchrotron emission with cooling break

It is well known for synchrotron emission sources to exhibit various breaks in their spectra due to cooling processes(e.g. Pacholczyk, 1970). One of the lowest frequency breaks likely to occur is

due to synchrotron losses. The electrons responsible for the emission above this cooling break lose energy due to synchrotron cooling faster than they can typically escape (which they do on roughly the dynamical timescale). If the source of acceleration in the plasma occurs continuously (i.e. there is a continuous injection of electrons from the heating/acceleration process), a steady state solution exists where the spectrum follows the usual synchrotron spectral index of $\beta = (3 - p)/2$ (with p the particle index) at energies below a characteristic energy, the 'cooling break', while above this energy the spectral index flattens to $\beta = (2 - p)/2$, corresponding to a particle index of $p + 1$ (Yuan et al 2003, Kardashev et al 1962). The position of the cooling break corresponds to the electron energy (or, in the emitted spectrum, the frequency) at which the cooling time is equal to the escape time. The escape time is uncertain but for our simple estimate we will use the dynamical time:

$$\tau_{cool} = 8 \left(\frac{B}{30 \text{ G}} \right)^{-3/2} \left(\frac{\nu}{10^{14} \text{ Hz}} \right)^{-1/2} \text{ min} \tag{4.1}$$

$$\tau_{esc} \approx \tau_{dyn} = \sqrt{\frac{R^3}{2GM}} \approx 5 \text{ min} \tag{4.2}$$

with $R \approx 3.5 \ R_S$ the radial position within the accretion flow. The cooling break therefore occurs at a frequency of

$$\nu_{cool} = 2.56 \left(\frac{B}{30 \text{ G}} \right)^{-3} \times 10^{14} \text{ Hz} \tag{4.3}$$

This model has more freedom than the power law model, and the data provide less constraint on physical parameters than in the IC or SSC (because in those cases the IR and X-ray flares arise from different emission mechanisms). We can determine what magnetic field strengths are necessary for such a model since the magnetic field B directly influences the position of the cooling break.

Such a cooling break model fits the data well. The magnetic field strengths we find for this case are of the order of the magnitude of those expected for the inner regions around Sgr A*.

4.5 Flare Evolution: Lightcurve Shape and Substructure

The SED modelling we presented in the last section only examined the mean properties of the flare emission. Our observations hold a great deal more valuable information in the time-dependent properties of the lightcurves. It is interesting to examine what different emission scenarios imply for the evolution of simultaneous flare in the IR and X-ray bands. There are two outstanding features of the simultaneous lightcurves that need to be understood: the broadness of the NIR lightcurve in comparison to the X-ray lightcurve, and the substructures seen in the NIR lightcurve but not in the X-ray lightcurve.

The synchrotron and IC luminosities depend on B, θ_E (think γ)[7], N and the size of the quiescent region R_Q as

$$L_{\text{synch}} \propto N\theta_E^2 B^2 \tag{4.4}$$

---

[7]We use θ_E and not γ in our arguments because θ_E represents a characteristic energy of the entire population of electrons, while γ more properly denotes the energy of each electron in the population.

$$L_{\text{IC}} \propto N\theta_E^2 R_Q^{-2} \qquad (4.5)$$

The SSC luminosity depends not on R_Q but on the size of the flaring region R_F as

$$L_{\text{SSC}} \propto N^2\theta_E^4 B^2 R_F^{-2}. \qquad (4.6)$$

The (changing) parameters governing the overall flare evolution are probably $N(t)$ and the electron temperature $\theta_E(t)$. For the case of submm photon IC, these are the only parameters that can affect both the optically thin synchrotron luminosity (not dependent on flare or quiescent region size) and the IC scattered luminosity (not dependent on magnetic field).

For the submm IC case, both the synchrotron and inverse Compton luminosities depend on the same powers of N and θ_E. This means that if only N or θ_E were to change throughout a flare, the X-ray lightcurve should follow the same functional form as the synchrotron lightcurve. That is, *both lightcurves should have the same width, or duration.* We can take this either

- as further evidence against the submm photon IC scenario, or

- to imply that *if* the X-ray flare is to be explained by the submm IC scenario, then the observed lightcurve widths can only be produced if some parameter aside from N and θ_E also varies throughout the flare.

If we consider the second possibility, then the magnetic field, B, is perhaps the most obvious choice for the varying parameter. The dependence of the lightcurves on B means that for a change in B to create a broader NIR lightcurve, the magnetic field must *decrease* during the flare. The process must reverse itself towards the end of the flare: the magnetic field must increase again towards initial values. Such behavior could, for instance, occur if stored magnetic energy in a small region were released to accelerate electrons, as in a reconnection event. Remember however the high magnetic fields required ($B \sim 200$ G) for the submm IC picture with `icmodel` in Section 4.4, which makes it difficult to decrease the magnetic field during a flare unless we accept even higher values for the magnetic field before and after the flare.

The only other possibility to explain the lightcurve durations in the submm IC scenario is that the photon density increases during the flare (i.e. effectively through the parameter R_Q). Although it is not realistic for the overall photon density of quiescent state photons to change much with time, the photon density experienced by the flare electrons could increase as it moves inwards within the accretion flow towards higher submm photon density. Again, to explain the second half of the flare, for this possibility the position of the flare within the accretion flow must move outwards towards lower photon density to increase the IR emission relative to X-ray emission as the flare declines.

As far as the substructure is concerned we can see from the same relations that a variation in the magnetic field affects the synchrotron luminosity but not the IC luminosity of submm-bump scattered photons. Within the IC picture then, it would be quite natural for the variations seen in the L′-band luminosity to be due to fluctuations in the magnetic field. The IC luminosity of submm bump photons, not dependent on B, would remain unaffected by such fluctuations. If relativistic effects are also taken into account (Doppler boosting in particular) then the magnetic field fluctuations we are talking about are actually the fluctuations in the magnetic field of the *observable* region at any given time.

However, if the magnetic field were as high as that found in the SED modelling section for the IC model ($B \sim 210$ G), then there would be a cooling break below IR frequencies and this picture could no longer work, since above the cooling break the lightcurve traces the pure rate of energy injection (no longer with any dependence on magnetic field). We are faced with a dilemma (in addition to the small size of the quiescent region which is required), where high magnetic fields are required to find an acceptable solution for the observed SED of the flare, but low magnetic fields are needed to keep the cooling break above IR frequencies, and we can not have both at once.

If we now examine the SSC scenario, the SSC luminosity goes quadratically in the quantity $N\theta_E^2$, which means that a synchrotron lightcurve has a natural width that is a factor $\sqrt{2}$ times the width of its SSC emission (for example, if the lightcurves can be described by Gaussian profiles $f(t) \propto \exp(-k(t - t_0)^2/w^2)$. Thus a longer duration synchrotron lightcurve is expected in the synchrotron case.

The observations of substructure however are not naturally explained. Within the SSC scenario both the SSC luminosity and the synchrotron luminosity are proportional to B^2, and fluctuations should thus induce variations of similar strength in both L'-band and X-ray lightcurves. As discussed in Section 4.3.3, substructure would be distinguishable in the X-ray lightcurve if it were of similar amplitude to that of the L'-band lightcurve.

Finally, there is the synchrotron scenario with a cooling break. Understanding simultaneous light curves in this scenario is more sensitive to the time dependent evolution of the electron distribution itself and thus self-consistent time-dependent modeling is required. We can make at least some qualitative predictions for the light curves of this model: as far as the difference in light curve widths is concerned, it seems it would be necessary for the cooling break to increase in frequency during the flare which would, as for the submm IC case, require a decrease in magnetic field during the flare (see Equation 4.3). In contrast to the submm IC case, for this case the decrease in magnetic field could occur together with plausible values for the magnetic field.

It also turns out that obtaining substructure in the IR light curve at the same time as producing a smooth X-ray light curve could be quite natural in the cooling break synchrotron model. Below the cooling break the emitted synchrotron spectrum is sensitive to variations in the magnetic field which is expected to be clumpy; while above the cooling break on the other hand the synchrotron emission traces rather the rate of energy injection alone. This could be expected to be rather smooth.

We think these aspects add very much to the plausibility of the synchrotron scenario as a viable mechanism for the production of the NIR/X-ray flare.

4.6 Discussion

4.6.1 Why inverse Compton scenarios don't work

Here we give some analytical arguments that clarify which essential features of our multiwavelength observations lead us to exclude the inverse Compton processes as possible emission scenarios.

There are three equations (see Rybicki & Lightman, 1986) which essentially describe all important relationships between seed, synchrotron and scattered spectra involved in one inverse Compton scattering process. The first of these is the relationship that describes the shift in

frequency of a seed photon upon encountering an electron of energy γ:

$$\nu_{IC} = \gamma^2 \nu_{seed}$$

For the submm IC case, photons are scattered from the submm bump, at $\nu_{seed} \sim 10^{12}$ Hz. For the X-ray slope to be soft ($\nu_{IC} < 10^{18}$ Hz) this equation restricts the electron energies of the electrons involved in the flare:

$$\gamma \lesssim 1000.$$

Secondly, the frequency at which these electrons are themselves emitting synchrotron emission is dependent upon γ and B [8]:

$$\nu_c = 4.2 \times 10^6 B \gamma^2. \tag{4.7}$$

Since we have already made a restriction on the electron energies, then if we require $\nu_c \gtrsim 10^{14}$ Hz (for a hard νL_ν spectral index in the IR), then we find that the magnetic field is also restricted:

$$B \gtrsim 25 \text{ G}.$$

Thirdly, there is the equation relating the ratio of IC to synchrotron luminosity:

$$\frac{L_{\text{compt}}}{L_{\text{synch}}} = \frac{U_{\text{ph,seed}}}{U_B} \tag{4.8}$$

where $U_{\text{ph,seed}}$ is the energy density of seed photons, $U_{\text{ph,seed}} \simeq L_{\text{ph,seed}}/cA$, and A the surface area of the electron population producing the seed spectrum.

In the submm case $L_{\text{ph,seed}}$ is L_{submm}, and the equation can be rewritten for $R_Q = \sqrt{A/4\pi}$ as

$$R_Q \simeq 0.013 \left(\frac{L_{\text{F}}}{L_\odot}\right)^{1/2} \left(\frac{L_{\text{Q}}}{L_\odot}\right)^{1/2} \left(\frac{L_{\text{IC}}}{L_\odot}\right)^{-1/2} \left(\frac{B}{40 \text{ G}}\right)^{-1} R_S \tag{4.9}$$

With this we obtain an uncomfortably low constraint on the size of (the most luminous part of) the quiescent region of $R_Q \lesssim 0.1 R_S$, similar to the small sizes we found were required in the SED model fitting of Section 4.4.

We can repeat the above series of arguments for the SSC case to obtain

$$\begin{aligned} \gamma &\lesssim 100 \\ B &\gtrsim 2400 \text{ G} \\ R_F &\leq 0.002 \text{ R}_S \end{aligned}$$

A constraint on the size of the flare emitting region itself also enables a constraint on the density of the flare emission region:

$$n_e \simeq 2.4 \times 10^9 \left(\frac{L_{\text{F}}}{L_\odot}\right)^{-2} \left(\frac{L_{\text{SSC}}}{L_\odot}\right)^{3/2} \left(\frac{B}{40 \text{ G}}\right) \left(\frac{\gamma}{100}\right)^{-2} \text{ cm}^{-3}$$

---

[8]Note that the formula we give here is for the case where electrons are spiralling exactly perpendicular to the magnetic field direction; i.e. the above equation actually contains a $\sin\theta$ term (θ the pitch angle of the electrons to the magnetic field) which is at maximum 1. If we took a smaller constant value (more realistic for an electron distribution with isotropically distributed pitch angles) then the results which follow would be even more restrictive.

and we obtain that $n_e \gtrsim 10^{10}$ cm^{-3}. As with the density we found in the SED modelling of Section 4.4, this is a very high density, several orders of magnitude higher than the density inferred for the inner regions of the accretion flow around Sgr A*($\sim 10^7$ cm^{-3}: Yuan et al., 2003).

As for the submm IC case, the driver for the high magnetic fields and densities in the SSC case is the restriction on the electron energies required by the soft X-ray slope, which in combination with a positive IR slope forces the magnetic field to very high values. Adding to that the high luminosity ratio, L_X/L_{IR}, the size of the flare region is driven to very small values which in turn forces the density to very high values.

These arguments show that for both cases there are three main properties which in combination are driving (i) in the submm IC case, the magnetic field to higher values than $B \approx 30$ G and the IC region to small sizes, and (ii) in the SSC case, to extremely high magnetic fields and electron densities. These are:

1. the soft X-ray spectral index

2. the hard MIR-IR spectral index

3. the high luminosity ratio, L_X/L_{IR}.

4.6.2 Comparison with past multiwavelength studies

Past multiwavelength observations of Sgr A* have favored models where the X-ray emission is due to inverse Compton scattering processes, with various possible combinations of seed photons and seed electrons from those producing the quiescent (submm) and flaring (IR) states. The obvious question is: why do we not find the same?

Eckart et al. (2004) modelled both IR and X-ray flares as SSC emission. However, that the flares at IR wavelengths are SSC emission is ruled out since the polarization of the IR flares points to a synchrotron origin.

Eckart et al. (2006c) modelled the X-ray flare as SSC emission via the prescription of Marscher (1983), and in their model the X-ray emission had a hard νL_ν index of $\beta = 0.4$ to match their X-ray observations. A hard νL_ν index in the X-ray will provide no constraint on the energies of the electrons producing the IR flare, which explains why these studies found this model to be acceptable with reasonable sizes for the quiescent state of Sgr A*. The X-ray flares of their study were however quite weak and the photon index may not have been well constrained (Porquet et al., 2008, Mascetti et. al. 2008 (submitted)).

A similar story applies to other investigations of the X-ray flares with IC and SSC processes: for example, for the SSC case of Liu et al. (2006b) the X-ray emission was again modelled for a hard spectral index in νL_ν; again, there was no restriction on the electron energies for such a case and a model can be found with reasonable physical parameters.

Yusef-Zadeh et al. (2006a) suggested two scenarios where the X-ray emission could be due either to (i) submm photons upscattered by electrons producing IR emission, the scenario we considered in Section 4.4.1, or (ii) IR (flare) photons upscattered by the electrons producing the quiescent state of Sgr A*.

The first case is the case we explored in Section 4.4.1. In Yusef-Zadeh et al. (2006a) however, the treatment involves a power law distribution of electrons and the differential flux is calculated for the corresponding power law section of the inverse Compton scattered spectrum only. Since the X-ray spectral index in this model was considered to be hard in νL_ν ($\beta = 0.4$), we have

the same situation as with the previous cases; there is no restriction on the electron energies producing the IR flare. Therefore, with electrons up to $\gamma \sim 6000$, it was possible to find a model that worked using a reasonable quiescent region size ($R_Q \approx 10\ R_S$).

The second case is a scenario we did not consider in our modelling. In fact it can be shown that the inverse Compton luminosity via this process (IR photons scattered by submm-emitting electrons) can never exceed the luminosity of the IC case we considered previously (submm photons scattered by IR photons).

For the case of IR photons scattered by submm-emitting electrons, the luminosity is (here using ν to denote a photon)

$$L_{IC}(\text{IR } \nu,\ \text{submm e}^-) = \frac{2R_F L_{submm} L_{IR}}{R_Q^3 c B^2}$$

where we have made use of the fact that only some proportion of the quiescent electrons (those within the flaring region where the photon density of IR photons is highest) are available to inverse Compton scatter photons:

$$L_{synch} = \frac{R_F^3}{R_Q^3} L_{submm}.$$

For the submm IC case that we already considered we have

$$L_{IC}(\text{submm } \nu,\ \text{IR e}^-) = \frac{2L_{submm} L_{IR}}{R_Q^2 c B^2}$$

and the ratio of the two is

$$\frac{L_{IC}(\text{IR } \nu,\ \text{submm e}^-)}{L_{IC}(\text{submm } \nu,\ \text{IR e}^-)} = \frac{R_F}{R_Q}$$

Thus the X-ray luminosity provided by the IR seed photon case is always going to be, at best, comparable to the X-ray luminosity produced in the submm seed photon case and will never dominate the emission. In Section 4.4.1 we found it was difficult to find a solution that did not involve an unrealistically small size for the quiescent region of Sgr A*. The contribution of IC emission through the scattering of IR seed photons by submm-emitting electrons is at best comparable to this emission and can not satisfy the observations either.

We also compare expectations for the inverse Compton scattered vs. synchrotron lightcurves for this scenario. The different widths of the lightcurves is as difficult to understand as in the case of inverse Compton scattered submm bump photons; again, the only way out may be for the magnetic field to decrease during the flare, and to be restored at the end of the flare. Additionally, if the IR flare provides the seed photons for the X-ray flare, then we should expect to see substructures in the X-ray lightcurve of the same order as and simultaneous with those in the IR lightcurve. Fluctuations in the magnetic field could not help this scenario because the IR flare is directly providing the seed photons for the X-ray flare in this case. Therefore we conclude that the time-resolved features of the lightcurves do not support this emission scenario either.

Overall, we have covered all reasonable conceivable inverse Compton scenarios for the origin of the X-ray flare simultaneous with our IR flare and have concluded that none of these inverse Compton scattering scenarios are viable.

Of past investigations, the most similar synchrotron model to those we present in this paper is the one-component synchrotron model presented by Yuan et al. (2004, see Figure 3). To our knowledge, this is the only previous work to suggest that both IR and X-ray flares are produced by synchrotron emission. Interestingly, in that paper, a one-component model for the electron distribution is ruled out on the basis that the X-ray spectrum is too soft ($\Gamma \sim 2$) to be consistent with the X-ray flares observed by Chandra.

4.6.3 The electron energy distribution

In Section 4.4 where we investigated inverse Compton scenarios for the simultaneous IR/X-ray flare (`icmodel` and `sscmodel`) we assumed a thermal distribution for the energy distribution of the relativistic electrons. The reason for this choice was for ease of calculation since the synchrotron emission of a thermal distribution of electrons is described by well known formulas (see Appendix). The thermal distribution is also an expected result of turbulent heating and radiative cooling processes and has been used elsewhere in models for the flares of Sgr A* (Liu et al., 2006b). Nevertheless, one might worry that through our assumption of a thermal distribution of electron energies we have limited ourselves to a special case and that there may exist other distributions of electron energies that allow the inverse Compton scenario to be an explanation for the April 4 IR/X-ray flare after all. Although we do not expect our results to be particular to the thermal distribution given that the arguments we developed in Section 4.6.1 were not specific to any particular arrangement of the electrons, we would like to here corroborate this expectation through modeling.

To investigate the senstivity of our results to the form of the electron distribution we investigated power law models for the NIR synchrotron emission with the inclusion of inverse Compton scattering. We take power law models of the form $n(\gamma) \propto \gamma^{-p}$ between energies of γ_{min} and γ_{max} and calculate the synchrotron and inverse Compton emission by integrating the synchrotron spectrum of a single electron of energy γ over all electrons in the distribution. We fixed the parameter $\gamma_{min} = 20$, assuming that the electrons are accelerated out of the population of electrons ($\gamma \approx 10 - 20$) that create the quiescent state synchrotron emission, but we also found that the results are not at all sensitive to the value of γ_{min} as we show in Figure 4.8 where we show also a model with $\gamma_{min} = 1$. As we did for our previous set of models, we fit the calculated SEDs to the observed data using XSPEC, naming this model `powerlawicmodel`.

We tested three models, with $p = 2$, $p = 0$ and $p = -2$, corresponding to falling, flat and rising electron distributions respectively. In Figure 4.8 we show the emitted SED and the electron distributions that correspond to the best fit in each case. The distribution of electron energies is irrelevant to finding a good fit to the observed data, and the SEDs for the best fits for all models appear similar. Amongst the best fit models the electron distributions show a lot of variety. For a power law of electrons with index $p = -2$ to which we also add an exponential cutoff, we find that the electron distribution of the best fit approaches the thermal distribution corresponding to the best fit for `icmodel`, as we would expect.

Interestingly, for this variety of models, the electron distributions all meet at a particular energy, $\gamma \approx 1000$. It appears that this energy is important (*even, the only important energy*) for the submm IC scenario, and we note that it corresponds exactly to the upper limit on electron energy that we found in Section 4.6.1, for the submm IC case.

In Table 4.2 we give parameter values for the power law model with $p = 2$. We find that in
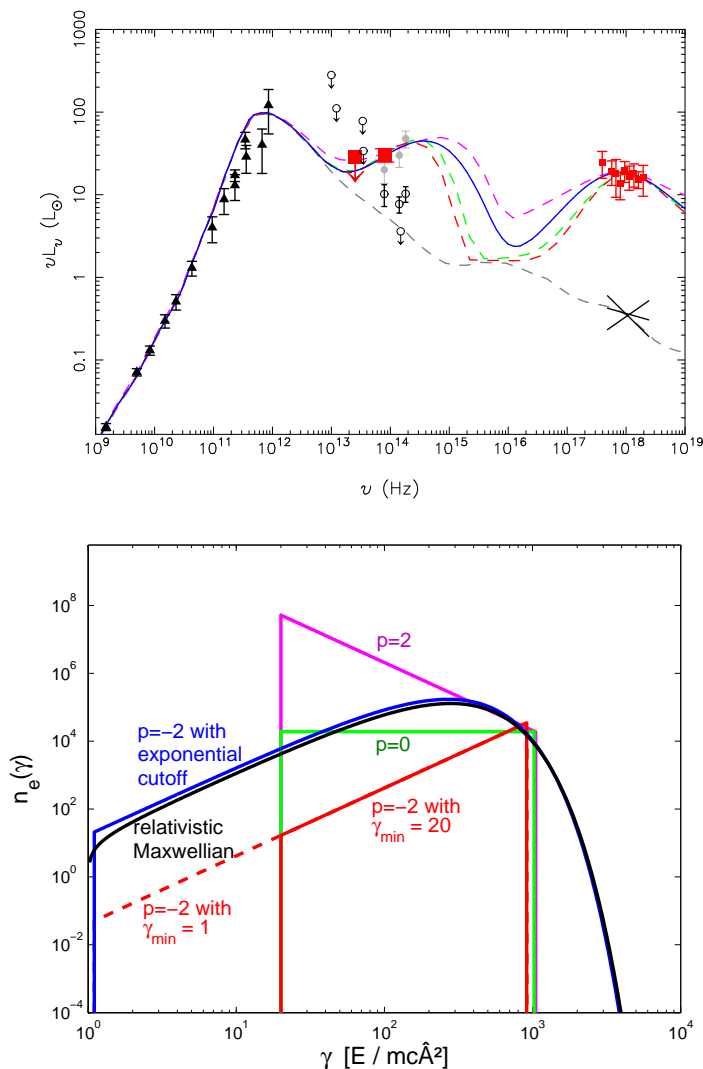
Figure 4.8 *Upper panel:* Best fit SEDs where the NIR synchrotron emission is produced by a power law distribution of electrons with index $p = 2, 0, -2$ (magenta, green and red dashed lines). The best fit model for a thermal distribution of electrons is shown in solid blue. All models appear relatively similar. Note that the (model-dependent) X-ray data is only shown for the thermal distribution of electrons case, but it should be similar for the other models. *Lower panel:* The electron energy distributions of best fit submm IC models each assuming a different underlying form for the energy distribution. We compare power law models ($n(\gamma) \propto \gamma^{-p}$) of index p = 2, 0 and -2 (magenta, green and red respectively). We also demonstrate that in a power law model of index -2 with an exponential cutoff (blue) we found the same energy distribution as in the thermal distribution case (in black; note that we used analytical equations to calculate the synchrotron emission for the thermal case in `icmodel` and `sscmodel` of Section 4.4). Although the electron distributions all look very different, they all cross at an energy $\gamma \approx 1000$.

Table 4.2.   Models: Fit Parameters

Fit to Mean Fluxes & NIR spectral index		
Parameter	powerlawicmodel	
N_H [$\times 10^{22}$ cm^{-2}]	11.8	$(10.0, 14.3)$
B [Gauss]	330	$(22, 2100)$
γ_{max} [ ]	1100	$(280, 1600)$
N_e [$\times 10^{40}$ electrons]	20	$(1.7, 1900)$
R_Q [R_S]	0.028	$(0.00003, 0.32)$
R_F [R_S]	> 0.02	
p	2.0	
χ^2 / d.o.f.	70.3 /75	
reduced χ^2	0.94	
Violates 3σ MIR upper limit?	No	

Note.   —   Summary of best fit parameters for powerlawicmodel fixing $p = 2$.   The constraints on the parameters are very similar to those found for the icmodel of Section 4.4 and appear to obey the constraints of Section 4.6.1.

general the parameters, in particular the confidence intervals, are similar to those in Table 4.1 for icmodel. Of particular interest is to see whether a larger value of R_Q can be accommodated to revalidate the inverse Compton scenario. The upper limit (90% confidence) for this parameter however of $R_Q < 0.32$ however, is still very small and does not allow for the this scenario to be compatible with the size measurements of Sgr A*. It appears that our finding for the submm IC scenario, where we find the implied size for the submm-emitting region must be much smaller than the observed size, is robust and is not sensitive to the form of the electron distribution.

Beyond assuming a particular form for the electron distribution, we should keep in mind that in reality the electron energy distribution is an evolving function that depends on the details of injection/escape and electron cooling. A truly self-consistent approach would allow the electron distribution function to be determined from the parameters themselves (such as, e.g. the magnetic field, which determines how long the electrons take to cool and thus has an important effect on the shape of the electron spectrum). The synchrotron spectrum would then be calculated directly from the time-dependent energy distribution function.

As an example of why the electron distribution should be self-consistently calculated from the model parameters, we note that both of our inverse Compton models require high magnetic fields. Even for the submm IC model with the lower of the two magnetic fields, the cooling timescale (Equation 4.1) is shorter than the dynamical timescale already at IR frequencies. The electron distribution in the case of such high magnetic fields would then be already dominated by cooling at L′-band wavelengths. In essence, a further requirement on our models is that we hope to find a solution with $B \lesssim 30$ G in order to keep the cooling break above the NIR band. However, as we have found in our analysis, there are certainly no solutions for the SSC model with such low magnetic field, and the submm IC only accommodates such a low magnetic field at the edge of its 90% confidence region.
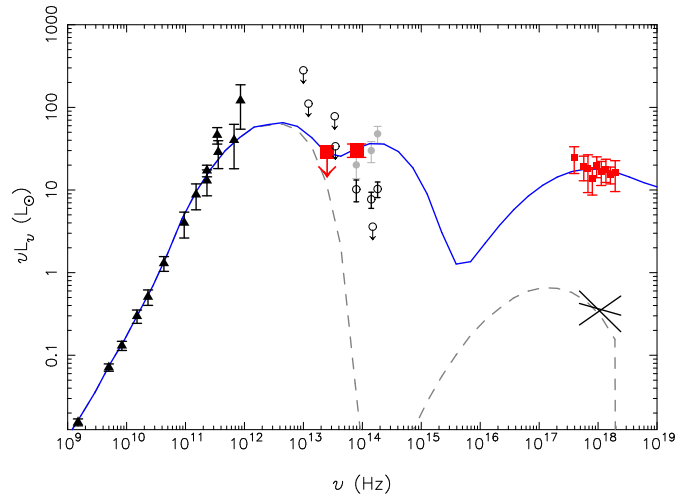
Figure 4.9 An submm inverse Compton model for the X-ray flare using a different model (the jet model, Falcke & Markoff, 2000) as template for the submm photon spectrum. The dashed gray line shows the jet model which is used as the source of seed photons. The solid blue line shows the best fit XSPEC model.

4.6.4   The jet model

The model spectrum we used to calculate the photon density of submm photons in `icmodel` was that of Yuan et al. (2003). However, this is not the only model that describes the quiescent spectrum of Sgr A*; the quiescent spectrum is also well described by a jet model (Falcke & Markoff, 2000).

To test whether our conclusions were robust with respect to the assumption of a quiescent model spectrum we created a new XSPEC model in which the submm spectrum to be upscattered was that of Falcke & Markoff (2000). Figure 4.9 shows the best fit model for this case, and the best fit parameters are very similar to those of `icmodel`, with somewhat higher magnetic field ($B \approx 300$ and lower electron temperature $\theta_E \approx 80$). The size of the quiescent region, R_Q is still very small ($R_Q \approx 0.02$) for the best fit model. Thus we can conclude that our findings are also not sensitive to the particular model we used to model the submm photon density.

4.6.5   Substructure in the context of an orbiting hot spot model

It is worth making a closing comment on our results in the context of the orbiting blob model (Genzel et al., 2003b; Broderick & Loeb, 2005; Meyer et al., 2006; Trippe et al., 2007), where the substructures observed commonly in the IR/NIR lightcurves are postulated to be due to relativistic beaming on the approaching side of the hot spot's orbit about the SMBH.

Due to the fact that the X-ray lightcurve is so smooth, and the substructure only shows up in the NIR lightcurve, then naively, the hot spot model does not seem to be compatible with the observed lightcurves; if relativistic beaming is occurring, it is not obvious how such structures could *not* also show up in the X-ray lightcurve.

We think this aspect of the multiwavelength emission from Sgr A* certainly deserves consid-

eration in models describing the flare emission from Sgr A* via a hot spot model. The different widths of the lightcurves are an additional important clue in this regard. Conversely, it is also obvious that given its likely proximity to the SMBH of $\approx 4 \times 10^6$ $M_\odot$ relativistic effects can have a considerable influence on the observed emission from Sgr A* and should be taken into account in models that try to explain multiwavelength properties of flares from Sgr A*.

4.7   Conclusions

We have presented the results of a simultaneous multiwavelength campaign at L′-band, X-ray and MIR wavelengths carried out on April 4 2008. We summarize the main observational results as follows:

- The L′-band and X-ray flares were simultaneous to within 3 minutes.

- The L′-band flare is much broader overall than the X-ray lightcurve.

- The L′-band flare showed significant substructure with a timescale of ∼20 minutes, while the X-ray flare showed no corresponding significant substructure.

- The νL_ν spectrum increases between 11.88 μm and 3.8 μm.

- The X-ray flare was very bright and soft in νL_ν ($\beta = -0.3 \pm 0.3$; Porquet et al., 2008).

- The emission region must be small, $< 1.5 R_S$.

We have drawn conclusions about the emission mechanism behind the flares which can be traced essentially to the hard MIR-IR νL_ν spectral index, the soft X-ray νL_ν spectral index, and the high ratio of X-ray to IR luminosity. Our conclusions are:

- We strongly disfavor the SSC case due to the extremely high magnetic fields and electron densities required to reproduce the observed data. Both quantities are several orders of magnitude larger than the values expected for the inner regions of the accretion flow about Sgr A*.

- We disfavor the submm IC case due to the high submm photon densities required to produce the observed X-ray emission, which imply a quiescent region size much smaller than implied by the size measurements. The IC case is also only marginally compatible with physically plausible magnetic fields of $10 - 30$ G.

- We also disfavor a different IC case (where the X-ray flare is due to IR seed photons upscattered by quiescent state submm-emitting electrons) since the inverse Compton scattered luminosity in this case is always dominated by the inverse Compton scattered luminosity of submm photons scattered by IR-emitting electrons.

- We favor a synchrotron scenario where the emitted spectrum flattens towards X-ray energies due to a cooling break. This scenario can be achieved with physically plausible magnetic field strengths and holds promise to explain more detailed structures of the lightcurves.

- For both the synchrotron and IC cases, the relatively shorter duration of the X-ray flare and perhaps the substructure of the IR emission is most plausibly understood as a result of a transient decrease of the magnetic field in the region of the flare. Such a decrease may point toward flares being triggered by conversion into electron heating of stored magnetic energy, such as a magnetic reconnection event.

Appendix

`icmodel` and `sscmodel`

Both `icmodel` and `sscmodel` are subsets of a single model with five parameters B, N, θ_E, R_F and R_Q.

For this model, we assume a spherical homogeneous emission region (containing the transiently heated/accelerated electron (flare) population emitting in the IR) of size R_F and of electron density $n_e = N/(4\pi R_F^3)$. The region contains a homogeneous magnetic field of strength B. We choose to model the electron distribution with the thermal electron distribution (i.e., a relativistic Maxwellian)

$$n(\gamma) = \frac{n_e \gamma^2 \sqrt{1 - 1/\gamma^2}}{\theta_E K_2(1/\theta_E)} \exp(-\gamma/\theta_E)$$

with $\theta_E = kT_e/m_e c^2$ the dimensionless electron temperature, and $K_2(x)$ a modified Bessel function of the second kind. The thermal distribution is a good example of an electron distribution of a characteristic energy (i.e. $\gamma \sim \theta_E$), and is an expected result of turbulent heating processes (Liu et al., 2006b).

The emission coefficient is approximated by (Mahadevan et al., 1996)

$$j_{\nu,\text{th}} = \frac{n_e e^2}{\sqrt{3} c K_2(1/\theta_E)} \nu M(\frac{2\nu}{3\nu_b \theta_e^2}),$$

in units of erg s^{-1}cm^{-3}Hz^{-1}ster^{-1}, and with

$$M(x) = 4.0505 a x^{-1/6} \exp(-1.8896 x^{1/3})(1 + 0.40b x^{-1/4} + 0.5316 c x^{-1/2}).$$

The absorption coefficient is

$$\alpha_{\nu,th} = j_{\nu,th}/B_\nu(T_e) = j_{\nu,th} \; \frac{c^2}{2h\nu^3} \; (\exp(h\nu/kT_e) - 1)$$

and the resultant synchrotron spectrum is computed for our spherical flare region (including optical depth effects) by the equation of radiative transfer

$$L_{\nu,\text{S}} = 4\pi \int_0^{R_F} \frac{j_\nu}{\alpha_\nu} \left(1 - \exp(-\alpha_\nu \sqrt{R_F{}^2 - r^2}\right) 4\pi r dr$$

which for small optical depth (an optically thin flare) simplifies to

$$L_{\nu,S} = 4\pi \left(\frac{4\pi}{3} R_F^3\right) j_\nu.$$

We compute the Inverse Compton scattered luminosity in our model through (Blumenthal & Gould, 1970)

$$L_{\nu,\text{IC}} = \frac{4\pi}{3} R_F^3 (h\nu)^2 \int_\gamma n(\gamma) \int_\epsilon (dN_{\gamma,\epsilon}/dtd\epsilon_1 d\epsilon) d\epsilon d\gamma$$

where γ, ϵ and $\epsilon_1 = h\nu$ are the electron energy, initial and scattered photon energies respectively, and the quantity

$$dN_{\gamma,\epsilon}/dtd\epsilon_1 d\epsilon = 3\sigma_T c\, n_{ph}(\epsilon)/4\gamma^2\epsilon \left[2q\ln q + (1+2q)(1-q) + \frac{(\Gamma_e q)^2 (1-q)}{2(1+\Gamma_e q)} \right]$$

where $\Gamma_e = 4\epsilon\gamma/mc^2$ is the Compton factor, $q = \epsilon_1/\Gamma_e(\gamma mc^2 - \epsilon_1)$. The photon density $n_{ph}(\epsilon)$, of flare state photons is determined from the model flare's luminosity by $n_{ph}(\epsilon) = n_{ph}(\nu)/h = L_\nu/(4\pi h^2\nu c R_F^2)$. Instead of modelling the quiescent state ourselves, we use the luminosity given by the quiescent model of Yuan et al. (2003), which reproduces the observations quite well. Using this quiescent model as input spectrum $L_{\nu,Q}$ then, the photon density of quiescent state photons is $n_{ph}(\epsilon) = L_{\nu,Q}/(4/3\pi h^2\nu c R_Q^2)$.

We implement `icmodel` and `sscmodel` via the above prescription, with only one difference concerning the parameters R_Q and R_F. For `icmodel`, R_F is not an input parameter, and is merely set to $R_F = R_Q$ (this simply ensures that a minimum of SSC emission is produced, so that a solution where the X-ray emission is due to inverse Compton scattering of submm photons may be found). Similarly for `sscmodel`, R_Q is not an input parameter, but is set to an arbitrarily high value (in this case to ensure that very little inverse-Comptonized submm emission is produced and a solution is found where the X-ray emission is due to SSC of IR/NIR photons).

`powerlawcool`

This model can be written as

$$\nu L_\nu \propto \begin{cases} \nu^{(3-p)/2} & \nu_{\text{min}} < \nu < \nu_c, \\ \nu^{(2-p)/2} & \nu_c < \gamma < \nu_{\text{max}}. \end{cases}$$

The cooling break, ν_c (Equation 4.3) occurs at $\nu_c = 2.56\,(B/30\ \text{G})^{-3} \times 10^{14}$ Hz, and the index p corresponds to the particle index in the underlying electron distribution:

$$n(\gamma) \propto \begin{cases} \gamma^{-p} & \gamma_{\text{min}} < \gamma < \gamma_c, \\ \gamma^{-(p+1)} & \gamma_c < \gamma < \gamma_{\text{max}}. \end{cases}$$

Chapter 5

Time Dependent Flare Models

Abstract: The emission from Sgr A*, the supermassive black hole in the Galactic Center, shows order of magnitude variability ("flares") a few times a day that is particularly prominent in the near-infrared (NIR) and X-rays. We present a time-dependent model for these flares motivated by the hypothesis that dissipation of magnetic energy powers the flares. We show that episodic magnetic reconnection can occur near the last stable circular orbit in time-dependent magnetohydrodynamic simulations of black hole accretion – the timescales and energetics of these events are broadly consistent with the flares from Sgr A*. Motivated by these results, we present a spatially one-zone time-dependent model for the electron distribution function in flares, including energy loss due to synchrotron cooling and adiabatic expansion. Synchrotron emission from transiently accelerated particles can explain the NIR/X-ray lightcurves and spectra of a luminous flare observed 4 April 2007. A significant decrease in the magnetic field strength during the flare (coincident with the electron acceleration) is required to explain the simultaneity and symmetry of the simultaneous lightcurves. Our models predict that the NIR and X-ray spectral indices are related by $\Delta\alpha \simeq 0.5$ (where $\nu F_\nu \propto \nu^\alpha$) and that there is only modest variation in the spectral index during flares. We also explore implications of this model for longer wavelength (radio-submm) emission seemingly associated with X-ray and NIR flares; we argue that a few hour decrease in the submm emission is a more generic consequence of large-scale magnetic reconnection than delayed radio emission from adiabatic expansion.

5.1   Introduction

The monitoring of stellar orbits has established beyond reasonable doubt that the Galactic Center hosts a supermassive black hole whose mass is $\approx 4 \times 10^6 M_\odot$ (Schödel et al., 2002; Ghez et al., 2003). Observations from the radio to the X-rays reveal that coincident with the black hole is a weak active galactic nucleus (Sgr A*) whose broadband non-thermal spectrum peaks in the sub-mm at $\sim 10^{12}$ Hz (Zylka, Mezger, & Lesch, 1992). The total luminosity of Sgr A* ($\sim 300 L_\odot$)

is five orders of magnitude smaller than would be produced by accretion of ambient gas at the Bondi rate with a radiative efficiency of $\sim 10\%$ (e.g., Baganoff et al., 2003). Many nearby galaxies host supermassive black holes that are comparably underluminous (Di Matteo, Carilli, & Fabian , 2001; Ho, 2008). Thus, Sgr A* has become a critical testing ground for theoretical models of hot, radiatively inefficient accretion flows (RIAFs) that are common in the local universe.

In addition to a baseline level of quiescent emission, Sgr A* also shows short-timescale "flares" in the X-ray (Baganoff et al., 2001), near-infrared (NIR; Genzel et al., 2003b), and sub-mm (Zhao et al., 2003). The duration of the NIR (~ 80 min) and X-ray flares (~ 50 min) is comparable to the orbital period of matter near the last stable circular orbit around the black hole. The flare properties can thus help constrain the physical processes occurring close to the event-horizon of Sgr A*. There is currently some debate as to whether the high amplitude, short time-scale variability from Sgr A* truly consists of distinct "flares," or is instead the tail end of a power spectrum of variability (Meyer et al., 2008); for our purposes, these distinctions are not that critical and we shall refer to the high amplitude tail of Sgr A*'s variability as "flaring."

Flares from Sgr A* have been observed for about ten years and it is now possible to summarize properties common to most of them (for a more detailed discussion see, e.g., Dodds-Eden et al. 2009). Flares are more common in the NIR than in the X-ray. The flux can increase by up to a factor of ~ 20 above the detection limit in the NIR and up to a factor of ~ 160 in the X-rays. When both are present, the flares in the X-ray and NIR do not show a significant time-lag. The NIR flares are polarized, consistent with a synchrotron origin; the polarization angle can even change significantly during the flare (Eckart et al., 2006b; Trippe et al., 2007; Meyer et al., 2006). For relatively luminous flares (which have better statistics) the spectrum in the NIR is $\nu L_\nu \propto \nu^{0.4}$ (Gillessen et al., 2006; Hornstein et al., 2007; Dodds-Eden et al., 2009). The bright X-ray flares show a (well constrained) softer spectrum, with $\nu L_\nu \propto \nu^{-0.25}$ (Porquet et al., 2003, 2008). The fainter X-ray flares may be harder (Baganoff et al., 2001). Better statistics are however required to conclude if there are indeed two populations of X-ray flares. (Porquet et al., 2008). Flares observed in the sub-mm tentatively show a lag of ~ 100 minutes with respect to the NIR and X-ray flares (Marrone et al. , 2008; Yusef-Zadeh et al., 2008).

The aim of this paper is to develop a time-dependent model of the emission from Sgr A*. Although there have been a number of models presented for the average properties of the flares (e.g., Markoff et al. 2001; Yuan et al. 2004; Liu et al. 2006b), only recently has there been work studying the time-dependent emission in detail (Chan et al. 2009; Dexter, Agol, & Fragile 2009; Maitra et al. 2009). In this paper, we model the time-dependent emission from Sgr A* using a simplified model for the evolution of the electron distribution during a flare, which takes into account synchrotron cooling and other processes (e.g., adiabatic losses and escape). Our methodology complements more detailed treatments of the time-dependent emission from accretion disk simulations (e.g., Dexter, Agol, & Fragile 2009), which focus on the thermal plasma; by contrast, we model the full electron distribution function, at the expense of considering a one-zone model with no dynamics and with a specified magnetic field and size. Given the electron distribution function, we then calculate the resulting time-dependent radio to X-ray spectrum.

The observation of a rising νL_ν spectrum in the NIR requires that the peak synchrotron frequency for the emitting particles be $\gtrsim 10^{14}$ Hz, which in turn requires particles with Lorentz factors $\gamma \gtrsim 1000(B/30\,\mathrm{G})^{-1/2}$ (B is the magnetic field strength in Gauss, G). Unless $B \gg 30$ G (which is strongly disfavored by multiple observational constraints; Sharma, Quataert, & Stone 2007b), the observed NIR spectrum *requires* non-thermal particles having energies well above

that associated with the quiescent 100 GHz brightness temperature of $\simeq 3 \times 10^{10}$ K (Bower et al., 2006) (i.e., $\gamma \sim 10$). This is why we focus on modeling the non-thermal distribution function in this paper. Moreover, we also focus largely on synchrotron radiation as the source of the flaring in both the NIR and X-rays; the alternative possibility, that the X-rays are produced by inverse-Compton upscattering of lower energy photons, is disfavored, at least for luminous flares (Dodds-Eden et al. 2009; see also §5.3).

Because there is no first-principles understanding of what generates the flares from Sgr A* (i.e., the source of particle acceleration), our models are necessarily somewhat phenomenological. In an attempt to go beyond phenomenological modeling, we also present results from time-dependent magnetohydrodynamic (MHD) simulations of accretion disks in which magnetic reconnection close to the last stable orbit dissipates magnetic energy in a manner similar to that required to explain the observed flaring from Sgr A* (see Yuan et al. 2009 and Ding et al. 2010 for related ideas).

The remainder of this paper is organized as follows. Section 5.2 provides a concrete physical model for the flaring from Sgr A*, motivated by "flares" in MHD simulations of accretion disks; some of the input parameters in our lightcurve models are motivated by these numerical results, but the lightcurve models are more general and are independent of the simulation results. Section 5.3 presents our calculations of the time-dependent evolution of the non-thermal electrons and the resulting lightcurves in different wavebands. We summarize and discuss the implications of our work in Section 5.4.

5.2   Flaring in Accretion Disk Simulations

Global MHD simulations of RIAFs have been carried out extensively in the last decade, both with non-relativistic (e.g., Armitage , 1998; Kudoh, Matsumoto, & Shibata , 1998; Stone & Pringle , 2001; Hawley & Balbus , 2002; Igumenshchev, Narayan, & Abramowicz , 2003) and relativistic codes (e.g., De Villiers, Hawley, & Krolik , 2003; McKinney , 2006; Mościbrodzka et al. , 2009; Fragile & Meier, 2009). The basic structure of such flows consists of a thick dense disk (moderately magnetized with ratio of gas pressure to magnetic pressure $\beta \equiv 8\pi p/B^2 \sim 1 - 100$) surrounded by a hot magnetically dominated corona, with jets launched near the last stable orbit (the efficiency of jet production depends on the imposed magnetic geometry and the spin of the black hole; Beckwith, Hawley, & Krolik 2008). In addition, the plasma within the last stable orbit near the equator (i.e., "disk" material) is in radial free-fall and becomes magnetically dominated ($\beta \ll 1$; e.g., Stone & Pringle 2001). Here we suggest that the observed flaring from Sgr A* may be due to magnetic reconnection close to the plunging region near the last stable orbit.

Magnetic reconnection has been invoked in past work (e.g., Markoff et al., 2001; Baganoff et al., 2001; Liu et al., 2004), but here we show explicitly that reconnection events can occur in numerical simulations of hot, magnetized accretion flows. The simulations that we present are essentially identical to Stone & Pringle (2001); Sharma, Quataert, & Stone (2007b). The only difference is that we look for and find flaring activity, driven by reconnection, at short timescales comparable to the orbital period at the last stable orbit. Previous simulations were largely focused on the time averaged structure of the accretion flow, while here we study short timescale reconnection events.

5.2.1   Numerical Setup and Initial Conditions

The numerical methods and initial conditions used here are described in detail in Sharma, Quataert, & Stone (2007b) (and references therein) so we only briefly review the key points. As in our previous work, we have carried out two-dimensional non-radiative accretion flow simulations in spherical (r, θ) geometry using the widely used ZEUS-MHD code (Stone & Norman , 1992a,b). We solve the standard equations of MHD in the pseudo-Newtonian potential of Paczynski & Wiita (1980): $\Phi = -GM/(r - r_g)$, where $r_g = 2GM/c^2$. Although we are not using a conservative code, we can capture a reasonable fraction of the dissipated magnetic energy using an explicit resistivity of the form (Stone & Pringle , 2001)

$$\eta = \eta_0 dr^2 \frac{|\nabla \times B|}{\sqrt{4\pi\rho}}, \tag{5.1}$$

with $\eta_0 = 0.15$. The resistive terms in the induction and internal energy equations are included using the method of Fleming, Stone, & Hawley (2000). The plasma in the simulations with resistivity is hotter (especially in regions with high current density) than in the simulations without resistivity because most of the dissipated magnetic energy is captured as heat; the dynamics and flaring are, however, essentially identical.

There is no physics in our simulations that picks out an absolute density scale or spatial scale. To express the numerical results in units relevant for observations of Sgr A*, we present all of our results for an $M_{\rm BH} = 4 \times 10^6 M_\odot$ black hole with a time averaged accretion rate of $\dot{M}_{\rm in} = 10^{-8} M_\odot {\rm yr}^{-1}$; the latter is chosen for consistency with the measured Faraday Rotation (Bower et al. 2003; Marrone et al. 2007; Sharma, Quataert, & Stone 2007b).

We use a 120×88 logarithmic grid (in both r and θ) extending from $2r_g$ to $800r_g$. The resolution is $\Delta\theta \sim \Delta r/r \approx 0.05$. The boundary conditions are the same as in Sharma, Quataert, & Stone (2007b). Strict outflow boundary conditions are applied at both the inner and outer radial boundaries (plasma is not permitted to enter the computational domain); scalar quantities and θ & ϕ components of vectors are copied from the closest active zones. The magnetic stress is required to be positive ($B_r B_\phi \leq 0$) at the inner radial boundary so that matter is not pulled into the computational domain from the inner boundary. Reflective boundary conditions are applied at $\theta = 0$, π with B_r copied, and B_θ & B_ϕ reflected.

The simulations initialize a dense, constant specific angular momentum torus as in Stone & Pringle (2001); the initial density maximum of the torus is at $200r_g$. The calculations that we focus on initialize a single poloidal magnetic loop threading the initial torus, with field lines aligned with the surfaces of constant density; we will also briefly mention results for simulations with two initial magnetic loops in the dense torus (see Fig. 8 of Sharma, Quataert, & Stone 2007b). The results of disk simulations remain sensitive to the initial magnetic field geometry, even at late times (Sharma, Quataert, & Stone , 2007b; Beckwith, Hawley, & Krolik , 2008).

5.2.2   Simulation Results

The initial dense torus becomes unstable to the magnetorotational instability (MRI; Balbus & Hawley 1991), causing mass to flow in toward the central black hole in form of a thick (since the disk is non-radiative) accretion disk that remains threaded by the initial magnetic field. Because we initialize a coherent poloidal magnetic field loop threading the torus, a current sheet is formed in the equatorial region. To search for flaring, we first wait for sufficient time that a quasi-steady
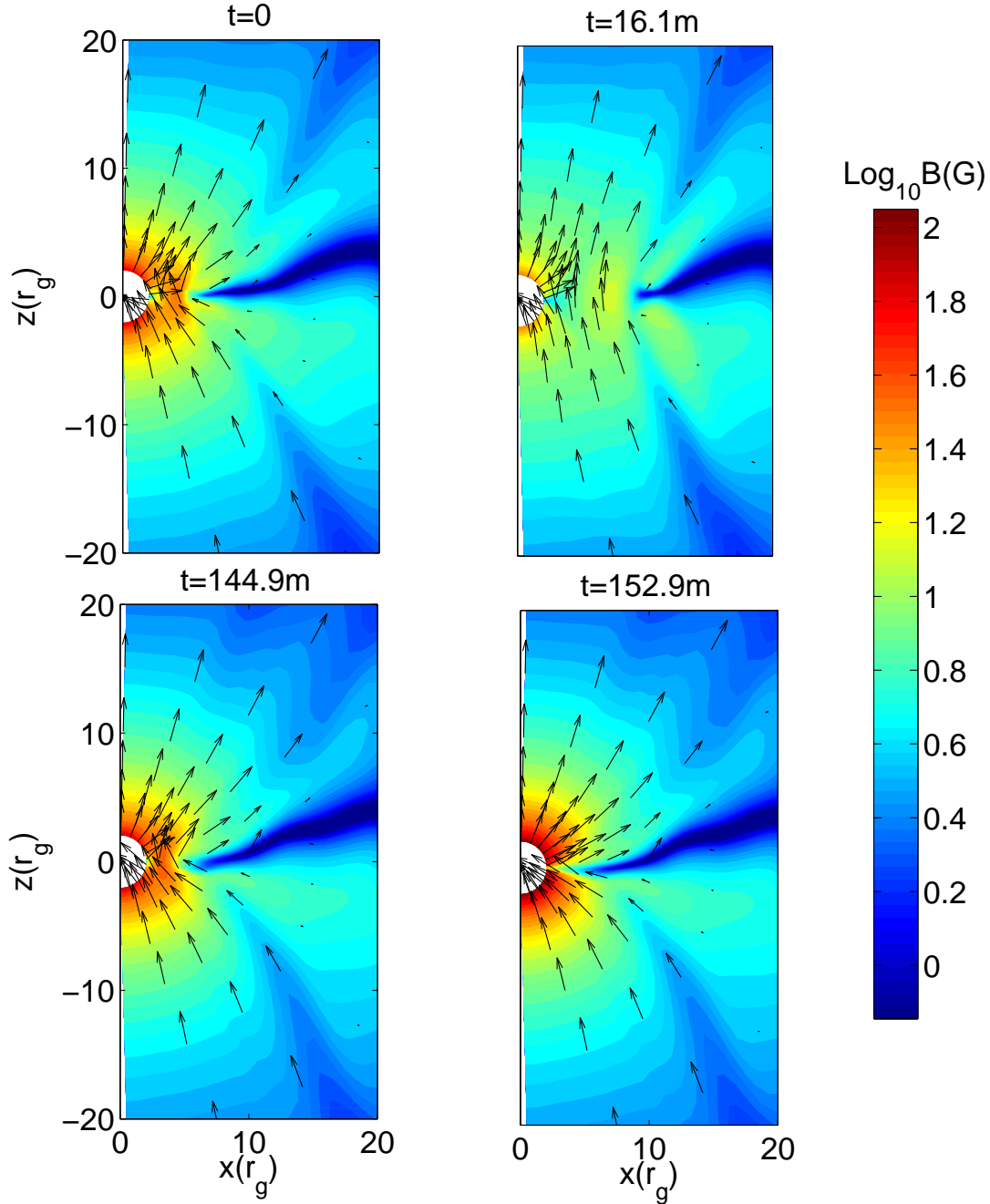
Figure 5.1 Two-dimensional contour plots of magnetic field strength (in G) at different times during one of the magnetic reconnection events identified in our simulations. Arrows denote the projection of the magnetic field unit vectors. Time $t = 0$ corresponds to the beginning of the magnetic reconnection event, and at $t = 152.9$ minutes the quasi-steady magnetic field structure and the equatorial current sheet are re-established. The snapshot just before t=0 looks similar to the quiescent state at $t = 152.9$. The magnetic field strength and times are plotted assuming $M_{\rm BH} = 4 \times 10^6 M_\odot$ and $\dot{M}_{\rm in} = 10^{-8} \, M_\odot \, {\rm yr}^{-1}$, as is reasonable for Sgr A*.

accretion flow is established at small radii (≈ 2 orbits at the initial density maximum). We then search for sudden temporal and spatial changes in physical quantities like the magnetic field strength and temperature, varying the spatial and temporal scales over which we analyze the results. For example, we analyzed the volume averaged magnetic field strength and temperature in the inner $6r_g$ of the simulation domain, sampled every ≈ 8 minutes (the orbital timescale at the last stable orbit is ≈ 17 minutes for Sgr A*). We find three magnetic reconnection events in this region in an interval of 4000 minutes. These are identified by a sudden decrease in the volume averaged magnetic field strength (from ≈ 60G to ≈ 20G) and an associated increase in temperature (by 10-100 times the quiescent value of $\approx 5 \times 10^{11}$ K). The temperature in these MHD simulations should be thought of as the ion temperature; the electron temperature is likely somewhat smaller. Thermal heating and nonthermal particle acceleration of both electrons and ions occurs during magnetic reconnection in solar flares (Lin et al. 2003). However, the quantitative details of these processes are not well understood, and as a result we will treat electron acceleration phenomenologically.

The reconnection event – identified with a sudden drop in magnetic field strength in the inner regions of the accretion flow and a simultaneous rise in the temperature – happens over ≈ 20 minutes, the dynamical timescale in this region; this is also comparable to the typical duration of the X-ray and NIR flares. After the plasma is heated, mass, energy, and magnetic flux are expelled outwards as the over-pressured plasma expands and is pulled out by magnetic tension; once the hot, expanding plasma escapes, the accretion flow starts to build up again. This whole process takes ≈ 150 minutes after which accretion is again in the quasi-steady state. The three "flares" we have identified are all qualitatively similar to each other. We describe one in more detail below. These flares are different from the variability expected from turbulent fluctuations in density and magnetic field strength in approximately the same region, which can produce fluctuations in the mm emission (Chan et al., 2009; Dexter, Agol, & Fragile , 2009).

Figure 5.1 shows two-dimensional snapshots of the magnetic field strength and the magnetic field unit vectors during one of the flares, from the beginning at $t = 0$ to when quasi-steady accretion is re-established at $t = 152.9$ minutes. Figure 5.2 shows the plasma temperature and velocity unit vectors at the same times. The quiescent magnetic field is split-monopolar with the field reversing in the equator. This is a consequence of the field we initialize at larger radii; it is not guaranteed that the disk will in fact have such a magnetic field.

The first panel in Figure 5.1 shows the beginning of the flare when the magnetic energy has started to decrease; this magnetic dissipation is accompanied by a significant increase in the temperature in the central few r_g (first panel of Fig. 5.2). By the second panel in Figure 5.1 at $\simeq 16$ min, the magnetic energy in the central region has decreased significantly and the equatorial current sheet in the disk (of low magnetic energy) is pushed out due to magnetic reconnection. This is because the hot super-virial plasma created near the last stable orbit is expanding outwards, as indicated by the velocity vectors in the top two panels of Figure 5.2. Most of the expanding material takes the path of least resistance and flows out along the "jet" at intermediate latitudes; note that this outflow is present at all times, but is significantly stronger during and just after the reconnection event. Once the hot, super-virial plasma leaves the inner region (bottom two panels in Figs. 5.1 & 5.2), the split-monopolar magnetic field geometry is re-established by accretion of plasma from larger radii. This last snapshot represents the 'quiescent' quasi-steady disk structure.

To test the sensitivity of these magnetic reconnection events to the initial magnetic geometry,
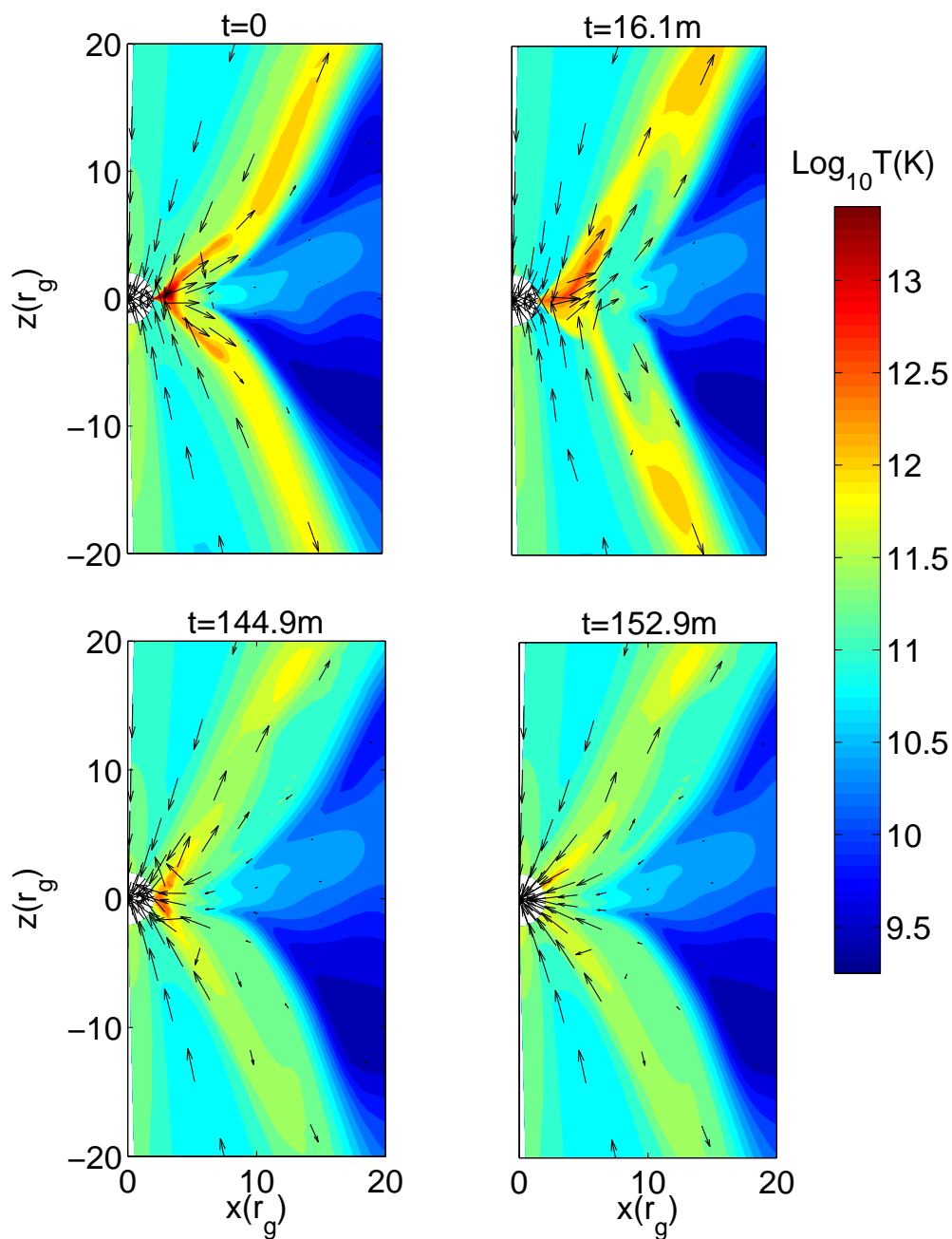
Figure 5.2 Two-dimensional contour plots of temperature (in K) at different times during the magnetic reconnection event shown in Figure 5.1. Arrows show the projection of velocity unit vectors. Starting at the beginning of the flare at $t = 0$, hot, over-pressured plasma expands outwards at mid-lattitudes at close to the speed of light. A quasi-steady accretion flow reforms at $t = 152.9$ minutes. The snapshot just before t=0 looks similar to the quiescent state at $t = 152.9$. The temperature is independent of the black hole mass and the accretion rate in these RIAF simulations.

we also studied an initial field geometry consisting of two poloidal field loops in the initial torus, with a net radial field in the equatorial plane (Fig. 8 of Sharma, Quataert, & Stone 2007b). The structure of the resulting turbulent disk is somewhat different. The disk is thicker and less dense because of the magnetic pressure provided by the strong toroidal magnetic fields in the disk mid-plane (see Figures 9 & 10 of Sharma, Quataert, & Stone 2007b). Magnetic reconnection events also occur near the last stable orbit for this initial magnetic field geometry, but they are not as dramatic and well-defined as in the case of a single initial loop. The reconnection events occur in the current sheets sandwiching the equatorial accretion disk; they are again accompanied by sudden heating of the inner regions due to magnetic dissipation. However, in this case the energy release is not sufficient to completely disrupt the quiescent accretion flow. An analogy to solar activity may be useful: in the simulations we focus on here (Figs 5.1 & 5.2), reconnection in the central region leads to a strong outflow qualitatively similar to a coronal mass ejection (CME) from the sun. In the case of two initial poloidal field loops, the reconnection events we find are more akin to true solar flares; i.e., magnetic energy is dissipated locally, but there is no large-scale outflow.

It is important to stress that the simulations presented here (Figs. 5.1 & 5.2) do *not* demonstrate that magnetic reconnection and flaring near the last stable orbit necessarily occur in MHD disk simulations (let alone in Sgr A*!). Rather, we demonstrate a weaker point: for disks with relatively coherent poloidal magnetic fields, simulations show magnetic reconnection events in which magnetic dissipation leads to localized heating and expansion of plasma. The oppositely directed magnetic fields required for these flares are generated by dragging in the coherent field lines from larger radii. Similar reconnection events are also present in axisymmetric MHD simulations of spherical accretion (Figs. 15 & 16 of Sharma, Quataert, & Stone 2008) and appears to be a generic feature of MHD accretion when inflow brings together oppositely directed field lines.

Future three-dimensional MHD simulations are required to explore in more detail the conditions under which this kind of reconnection can occur. Three-dimensional simulations, (e.g., Hawley & Balbus 2002) do show an overall flow structure that is quite similar to two-dimensional simulations (e.g., Stone & Pringle , 2001). However, the critical issue here is related to the dynamo generation of large-scale magnetic fields in disks, which is still poorly understood. Because of these uncertainties, it is also not possible for us to reliably determine the statistics of reconnection events in the simulations for comparison to observations. However, the consistency with the energetics and timescales of the observed flares is encouraging and it seems plausible that the X-ray/IR flares observed in Sgr A* are due by reconnection, qualitatively similar to what is seen in our MHD simulations.

In the next section, we present a simple non-thermal electron acceleration model to explain the observed flares from Sgr A* in the context of both quasi-stationary heated plasma (corresponding to a mild flare) and expanding plasma (a CME-like flare).

5.3   Lightcurve Modeling

In order to understand the time-dependent emission from nonthermal particles in Sgr A*, we have developed a simple model to describe the evolution of a transiently heated electron population. Some of the parameters we consider in these models are motivated by the simulations described in the previous section, but our lightcurve modeling is more general and does not depend in detail

on the source of the energetic particles.

We first investigate general properties of time-dependent models given different assumptions about the dominant energy loss mechanism (for example, synchrotron cooling or adiabatic expansion). We then apply these models to the observed properties of the very bright and very high quality simultaneous NIR/X-ray flare from Sgr A* that was observed on April 4, 2007 (Dodds-Eden et al., 2009; Porquet et al., 2008; Yusef-Zadeh et al., 2009; Trap et al., 2010). The April 4, 2007 event, observed with NACO (VLT) at 3.8μm and with XMM-Newton at 2-10 keV, was sufficiently bright that detailed lightcurves were obtained simultaneously at multiple wavelengths, giving us an unprecedented chance to use the observations to explore the acceleration and cooling physics in Sgr A*. Key properties of this luminous flare include (Dodds-Eden et al., 2009, see also Figures 5.5, 5.9 and 5.10 later in this paper):

- The NIR and X-ray lightcurves are both relatively symmetric and peak simultaneously (to within ≈ 5 minutes), and yet

- the 3.8μm rise and decay times are slower than in the X-ray, and the FWHM of the 3.8μm lightcurve is about twice that of the X-ray

- the NIR lightcurve shows dramatic substructure that is not present at the same level in the X-ray lightcurve (see Fig. 5.9)

- the X-ray flare has an average spectral index ($\nu L_\nu \sim \nu^\alpha$) of $\alpha_X < 0$ with 90% confidence (Porquet et al., 2008) while the NIR flux together with an upper limit at 11.88μm favors a spectral index $\alpha_{L'} > 0$. Previous NIR observations find $\alpha_{L'} \sim 0.4$ for luminous flares (Hornstein et al., 2007).

In Dodds-Eden et al. (2009) we proposed a "cooling break" synchrotron model to explain the average spectral properties of this flare and, by extension, all luminous flares from Sgr A*, which have similar properties (see Kardashev et al. 1962 for the basic theory of cooling breaks). In this model, both the NIR and X-ray emission are synchrotron emission, but the effect of synchrotron cooling is to produce a spectral break between the NIR and X-ray with $\Delta\alpha = 0.5$. The observed NIR and X-ray spectra are consistent with such a spectral break. The cooling break synchrotron model forms the basis of the models we explore here. In particular, observational and theoretical considerations strongly disfavor Inverse Compton (or Synchrotron Self-Compton) emission as the source of the observed X-ray flare (Dodds-Eden et al., 2009). We also explore the implications of our models for longer wavelengths (submm-radio), for which there was also data taken on April 4, 2007; in particular, a ~ 0.4 Jy flare was seen at 43 GHz with a duration of 100 minutes and a delay of ~ 6 hours relative to the NIR/X-ray event (Yusef-Zadeh et al., 2009).

5.3.1 Numerical Model

We calculate the synchrotron emission from an evolving population of electrons. The electron distribution function $N_e(\gamma, t)$ (units: number of electrons per unit Lorentz factor) evolves according to the following continuity equation (Blumenthal & Gould, 1970):

$$\frac{\partial N_e(\gamma, t)}{\partial t} = Q_{\text{inj}}(\gamma, t) - \frac{\partial[\dot{\gamma} N_e(\gamma, t)]}{\partial \gamma} - \frac{N_e(\gamma, t)}{t_{\text{esc}}} \tag{5.2}$$

where $Q_{\mathrm{inj}}(\gamma, t)$ is the rate at which electrons of Lorentz factor γ are injected at time t, the second term takes into account the redistribution of electrons in energy (i.e., cooling processes), and the third term allows the possibility that electrons may escape the region, with t_{esc} the escape timescale. We take $Q_{\mathrm{inj}}(\gamma, t)$ to be a power-law in γ: $Q_{\mathrm{inj}}(\gamma, t) = c_{\mathrm{inj}}(t)\gamma^{-p}$ with the normalization of the power law a function of time, $c_{\mathrm{inj}}(t)$, which we call the injection profile. The injected energy distribution has an exponential cutoff at γ_{max}, which we set to 10^6 in our calculations (the exact value of γ_{max} is not important), and a minimum energy of $\gamma_{\mathrm{min}} \sim 10$. This choice of minimum energy assumes that the electrons are accelerated out of the thermal population of electrons, which have $T_e \sim 3 \times 10^{10}$ K in many models (e.g., Sharma et al. 2007a), and which emit in the sub-mm (e.g., Yuan et al. 2004). Below γ_{min} the injected distribution breaks to a slope of $p = -2$, as would a thermal distribution.

The $\dot{\gamma}$ term in equation (5.2) accounts for energy loss. We consider both synchrotron cooling and adiabatic expansion:

$$\dot{\gamma} = \dot{\gamma}_{\mathrm{synch}} + \dot{\gamma}_{\mathrm{ad}}. \tag{5.3}$$

For synchrotron cooling, $\dot{\gamma}_{\mathrm{synch}} = -\gamma/t_{\mathrm{cool}}$ where $t_{\mathrm{cool}} = 7.7462 \times 10^8/(\gamma B^2)$ for an isotropic distribution of pitch angles (Rybicki & Lightman 1986). For adiabatic expansion, $\dot{\gamma}_{\mathrm{ad}} = -\gamma \, d\ln R/dt$ where $R(t)$ is the radius of the volume of interest (approximated as a sphere for simplicity). We express adiabatic losses in terms of R rather than the electron number density n_e because the latter can change by injection/escape which do not, however, modify the energy of the particles.

The electron distribution function and lightcurves depend on the value of B and on how both B and R change with time. For an adiabatically expanding plasma, the magnetic field $B(t)$ will be affected by the expansion, in addition to n_e and γ. For a fixed radial magnetic field, magnetic flux conservation implies $B \sim 1/R(t)^2$, but the dependence can be more general depending on the magnetic field geometry.

The synchrotron emission is calculated at each time given the instantaneous electron energy distribution using formulae from Rybicki & Lightman (1986). We calculate the emission coefficient from

$$j_\nu = \frac{1}{4\pi} \int_1^\infty n_e(\gamma)\langle P_e(\gamma, \nu, \phi)\rangle d\gamma \tag{5.4}$$

where we approximate the pitch-angle (ϕ) averaged spectral power emitted by a single electron $\langle P_e(\gamma, \nu, \phi)\rangle$ using

$$P_e(\gamma, \nu, \phi) = \frac{\sqrt{3}q^3 B}{mc^2} F\left(\frac{\nu}{\nu_{syn}(\gamma, \phi)}\right)\sin\phi \tag{5.5}$$

evaluated at $\phi = \arcsin(\pi/4)$ (which is close to the true pitch angle averaged spectrum and much faster to evaluate). The angle-averaged value of the critical synchrotron frequency is $\langle \nu_{\mathrm{syn}}(\gamma, \phi)\rangle = 3qB\gamma^2/(16m_e c)$, where q, m_e and c are the electron charge, mass, and the speed of light. The function $F(x) = x\int_x^\infty K_{5/3}(\xi)d\xi$ in equation 5.5 describes the shape of the spectrum.

We calculate the absorption coefficient from

$$\alpha_\nu = \frac{c^2}{8\pi\nu^2 mc^2}\int_1^\infty n_e(\gamma)\left(\frac{2P_e(\gamma)}{\gamma} + \frac{dP_e(\gamma)}{d\gamma}\right)d\gamma \tag{5.6}$$

and then the resultant emission, assuming a homogeneous sphere of radius R (Gould, 1979), using

$$\nu L_\nu = 4\pi^2 R^2 \frac{\nu j_\nu}{\alpha_\nu}\left(1 + \frac{\exp(-2\alpha_\nu R)}{\alpha_\nu R} - \frac{1 - \exp(-2\alpha_\nu R)}{2\alpha_\nu^2 R^2}\right). \tag{5.7}$$

We checked our numerically computed spectra against the analytical equations of Gould (1979) and Marscher (1983). Note that if the emission is optically thin, the luminosity only depends on the total number of accelerated electrons $N_e \sim n_e R^3$. There is thus a degeneracy between the number density of accelerated particles n_e and the size of the flaring region R. By contrast, if optical depth effects are important, which is the case for the radio emission, this degeneracy is broken.

The end result of our calculation is the self-consistently determined time-dependent synchrotron SED, given the following possibly time-dependent input parameters: magnetic field $B(t)$, particle injection rate $c_{\mathrm{inj}}(t)$, particle index of the injected electron distribution p (which we take to be constant in time), and radius of the emission region $R(t)$. In Section 5.3.5 we also calculate the inverse Compton scattered spectrum, which provides an independent constraint on the size of the emission region; we use the prescriptions of Blumenthal & Gould (1970).

5.3.2   Lightcurves

Figure 5.3 shows model NIR (L'-band; 3.8 μm) and X-ray (4.1 keV; 10^{18}Hz) lightcurves and spectral indices, for three different assumptions about the dominant electron energy loss mechanism: synchrotron cooling, escape, and adiabatic expansion (corresponding time-dependent SEDs for the different cooling mechanisms are shown in Figure 5.4). The parameters of these models are given in Table 5.1, where the models are parameterized by the total number of electrons at the peak of the X-ray flare; the particle index, p, the value of the magnetic field at the peak B_{peak} (i.e., B at 56 minutes); the escape time t_{esc}; and the (constant) expansion velocity, v_{exp}, in units of R_i/hr where R_i is the initial radius (expansion begins at $t = 0$). The actual value of R_i does not matter here because both the 3.8μm and X-ray emission are optically thin (hence we did not apply optical-depth effects in these calculations). The injection profile of the accelerated particles is the same in all of the models: a Gaussian with a FWHM of $\simeq 27.5$ min. In each calculation, the particle index p was adjusted (see Table 5.1) so that the peak IR luminosity was comparable to the peak X-ray luminosity; larger p would lead to a lower X-ray luminosity relative to the IR luminosity, and vice-versa, but otherwise the value of p does not change any of our conclusions about the NIR and X-ray flares.

Figure 5.3 shows that the X-ray and NIR lightcurves behave very differently for different model parameters. The X-ray lightcurve is almost independent of the model details, while the NIR lightcurve is much more sensitive. This difference is due to the very different synchrotron cooling timescales for electrons emitting in the IR and X-ray. The synchrotron cooling timescale for an electron emitting at a given frequency ν is given by

$$t_{\mathrm{cool}} \simeq 8 \left(\frac{B}{30\,\mathrm{G}} \right)^{-3/2} \left(\frac{\nu}{10^{14}\,\mathrm{Hz}} \right)^{-1/2} \quad \mathrm{min.} \tag{5.8}$$

In the X-ray, the synchrotron cooling timescale is almost always much shorter than the injection timescale. In that limit, the electrons radiate all of the energy they are supplied (via injection) and the emission is independent of the precise values of γ, B, R, etc. This is why the X-ray lightcurve closely follows the rate of electron injection in Figure 5.3, and is independent of the model details. By contrast, the L' emission, for most of the flare duration, occurs near or below the cooling break – the frequency at which the synchrotron cooling timescale is comparable to the injection time (which is expected to be of order the dynamical time). As a result, the NIR

SYNCHROTRON COOLING

ESCAPE

ADIABATIC COOLING
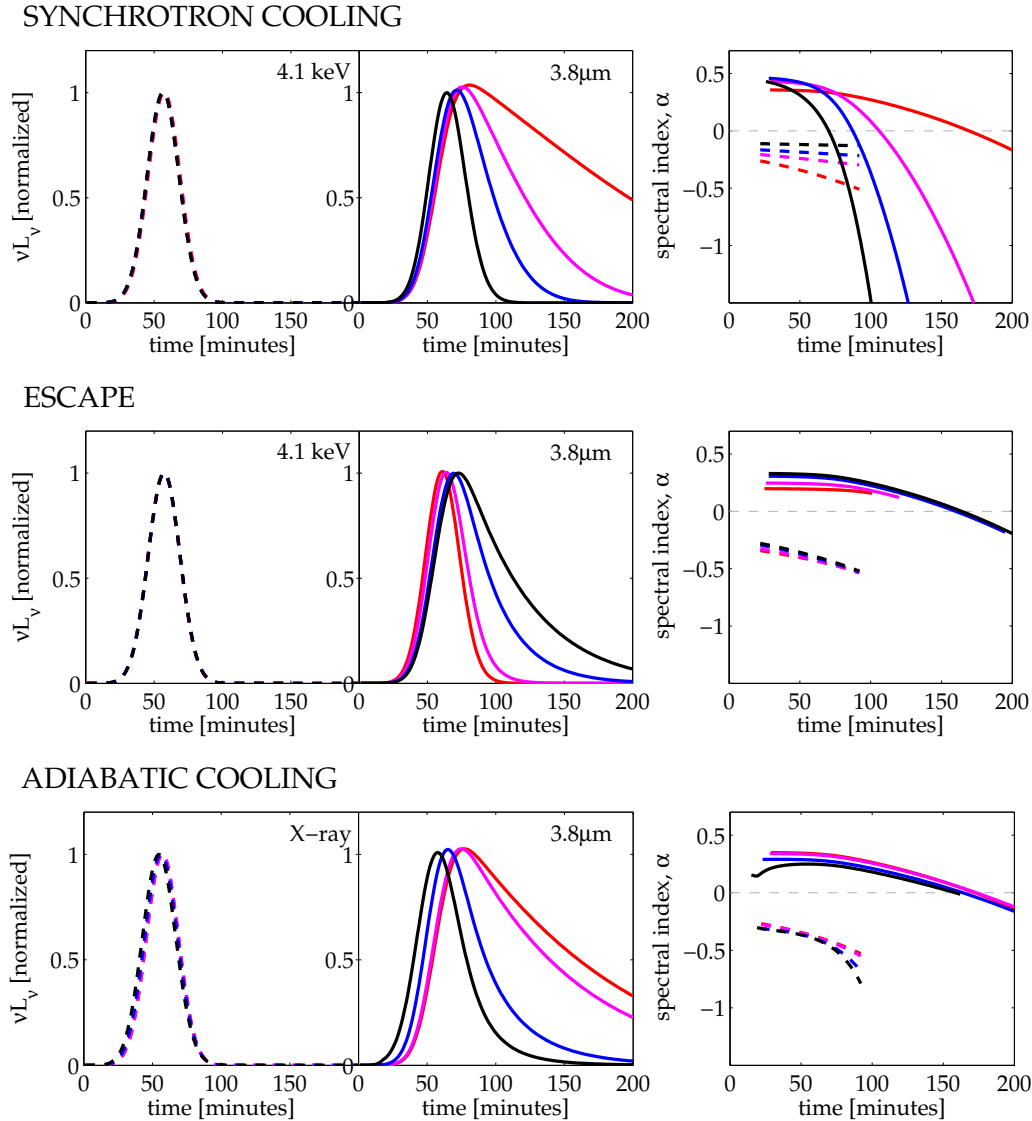
Figure 5.3 X-ray and NIR (L'-band) lightcurves, spectral indices, and (optically thin) SEDs for the flare evolution models given in Table 5.1. Both X-ray and L'-band lightcurves are normalized to the peak X-ray luminosity (the absolute luminosities are proportional to N_e because the emission is optically thin). The spectral indices are only shown where the the corresponding lightcurve exceeds 1% of the peak flux. *Synchrotron cooling:* Black to red corresponds to $B = 30, 15, 10$, and 5 G, respectively. *Escape:* Black to red corresponds to escape timescales of 60, 30, 10 and 5 min. *Adiabatic cooling:* Black to red corresponds to expansion velocities of 0.1, 0.05, 0.01 and 0.005 R_i/hr, where R_i is the initial radius of the expanding plasma.
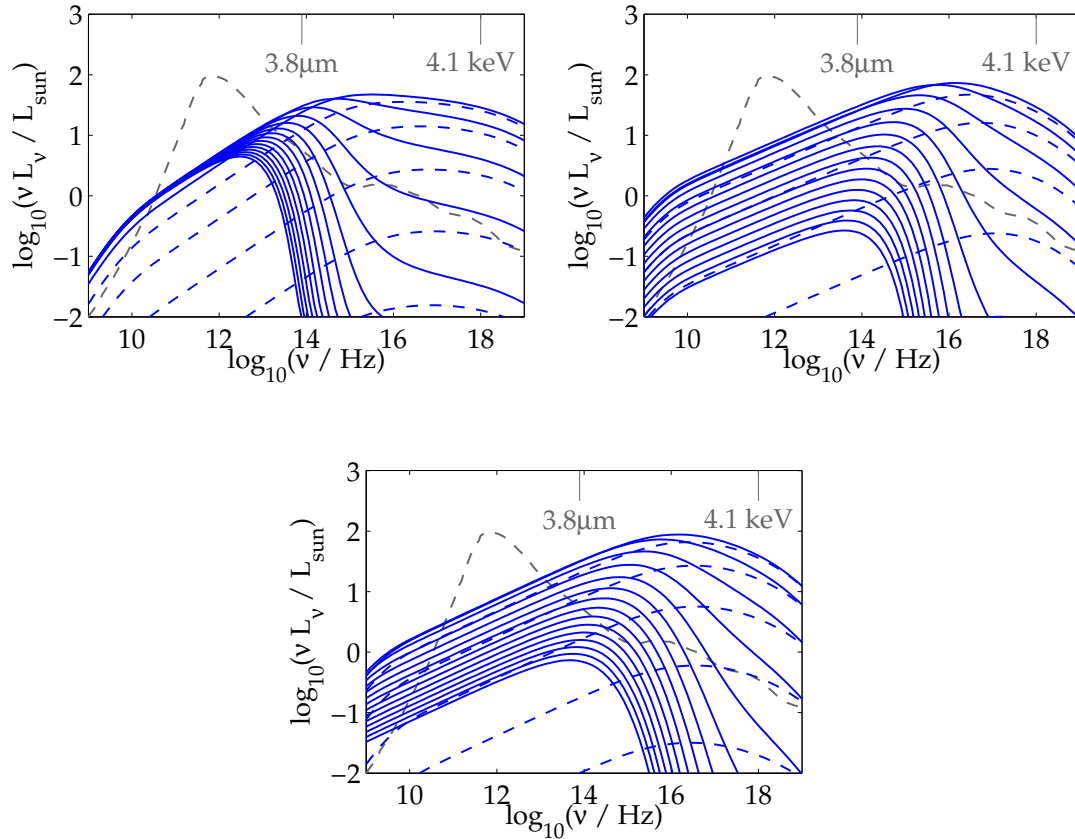
Figure 5.4 SED plots showing the evolution of the SED with time for models where the decline phase of the NIR lightcurve is dominated by synchrotron cooling, escape, or adiabatic cooling (corresponding to the lightcurves shown in blue in Figure 5.4). The dashed lines show the rising phase, while the solid blue lines show the evolution after the peak X-ray emission. The SED is plotted at 10 minute intervals. The quiescent model of Yuan et al. (2003) is plotted (dashed gray line) for reference. We did not apply optical depth effects in these models since we are focusing on the optically thin X-ray and NIR emission.

emission is sensitive to the details of the model. The general trend is the same regardless of the precise energy loss mechanism. Models with longer "cooling" times (be it via synchrotron, escape, or adiabatic losses) produce longer duration flares in the NIR, particularly when the cooling time is longer than the injection time. This is because the particle energy builds up initially and is then released over a longer period of time. These longer duration NIR lightcurves are also always delayed with respect to the peak of the injection and the peak of the X-ray lightcurve.

The results in Figure 5.3 are not consistent with some of the observed properties of the April 4, 2007 flare (see Figures 5.5, 5.9 and 5.10 for the observed data). For example, model L'-band lightcurves with the same duration as the April 4, 2007 flare ($\simeq$ 54 min) are typically delayed from the X-ray lightcurve by 10-15 minutes, longer than that observed. Of the three different energy loss mechanisms, the adiabatic model does better than the other two in matching the longer duration and short delay (compare, e.g., the $B = 10$ G synchrotron cooling model, with a 19 min delay and 68 min duration, with the $v_{\mathrm{exp}} = 0.05R_i/$hr adiabatic cooling model, which has a 9 minute delay and 55 min duration). The adiabatic expansion models have a shorter delay because the magnetic field decreases with the expansion ($B \propto 1/R^2$): this decreases the NIR emissivity of the electrons with time, and allows the lightcurve to peak earlier than it would due to the other cooling/loss processes.

The asymmetric NIR lightcurves in Figure 5.3 are also inconsistent with the April 4, 2007 flare, for which the lightcurves are reasonably symmetric and simultaneous and yet have different durations. A related problem is to understand the *rising phase* of the lightcurve. The slow rise of the NIR lightcurve compared to the X-ray lightcurve in the flares from Sgr A* cannot be explained by solely invoking a cooling mechanism, as is demonstrated in Figure 5.3, but requires a reduction in emissivity. If is, of course, possible that the discrepancies between the simple models in Figure 5.3 and the observed flares from Sgr A* are related to our overly simplistic treatment of particle acceleration. For example, lower energy (IR emitting) electrons need not have the same injection profile as higher energy (X-ray emitting) electrons. We do not explore this in detail, but instead focus on the possibility that changes in the magnetic field during flares strongly influence their observed properties.

If we define an "injection timescale" as $t_{\mathrm{inj}} = N_e(\gamma, t)/Q_{\mathrm{inj}}(\gamma, t)$ then the time-dependent position of the cooling break is given by

$$\nu_{\mathrm{cool,syn}} \approx \frac{10^{14}}{(p-1)^2} \left(\frac{B}{30 \text{ G}} \right)^{-3} \left(\frac{t_{\mathrm{inj}}}{10 \text{ min}} \right)^{-2} \text{ Hz.} \tag{5.9}$$

The relative luminosities in the X-ray and NIR depend on the position of the cooling break, which in turn depends on the injection timescale and the magnetic field strength. For example, for a fixed X-ray luminosity, a higher frequency cooling break corresponds to a lower NIR synchrotron luminosity (and vice-versa).

If the magnetic field were to *decrease* during the flare, that would increase both the synchrotron cooling time and the cooling break frequency. An increasing cooling break frequency during the rising phase of the flare would in turn cause the NIR lightcurve to rise more slowly than the X-ray lightcurve, qualitatively consistent with observations. Another way to understand this is to note that the X-ray emissivity does not decrease if the magnetic field decreases because the synchrotron cooling time in the X-rays is shorter than the injection time. However, a decreasing magnetic field strength would decrease the emissivity in the NIR where the cooling time can be longer than the injection time. The decreasing B required in this scenario is also consistent with

Table 5.1. Properties of L'-band and X-ray flares in the time-dependent synchrotron model

Model	Remarks	$N_e(t_{\mathrm{peak}})$ $[\times 10^{45}]$	p	$B(t_{\mathrm{peak}})$ [G]	t_{esc} [min]	v_{exp} $[R_i/\mathrm{hr}]$	Δt_{peak} [min]	fwhm$_X$ [min]	fwhm$_L$ [min]
Synch cooling	$B = \mathrm{const}$	0.026	1.95	30	1000	0	2	27.5	28
		0.057	2.03	15	1000	0	7	27.5	31
		0.13	2.11	10	1000	0	19	27.5	68
		0.81	2.27	5	1000	0	26	27.5	152
Escape	$B = \mathrm{const}$	7.2	2.59	5	5	0	4	27.5	29
		3.9	2.49	5	10	0	7	27.5	32
		1.7	2.37	5	30	0	12	27.5	44
		1.2	2.32	5	60	0	16	27.5	59
Adiabatic cooling	v_{exp}=const & $B \propto 1/R^2$	4.3	2.43	5	1000	0.1	4	36	46
		2.5	2.38	5	1000	0.05	9	32	55
		1.1	2.30	5	1000	0.01	18	28	97
		0.95	2.29	5	1000	0.005	20	27.5	113
Decreasing B	$B(t)$	3.1	2.4	5.1	200	0	3	31	59
		2.5	2.4	5.6	30	0	3	31	60
		1.6	2.4	7.1	10	0	3	31	62
April 4, 2007 L'/X-ray flare							3.4 ± 1.2	27.4 ± 1.4	54 ± 4

Note. — Parameters and results for the different flare models shown in Figures 5.3 and 5.4 (*Synch cooling, Escape, & Adiabatic cooling*) & 5.5 (*Decreasing B*). $N_e(t_{\mathrm{peak}})$ shows the total number of accelerated particles at the time when the X-ray flare peaks that would produce a peak X-ray luminosity of $30L_\odot$; however, the value of $N_e(t_{\mathrm{peak}})$ does not influence the lightcurve shape (i.e., duration, delays) because the NIR and X-ray emission are optically thin. The electron power-law index is p ($n(\gamma) \propto \gamma^{-p}$); $B(t_{\mathrm{peak}})$ denotes the magnetic field strength at the time when the X-ray flare peaks; t_{esc} and v_{exp} denote the escape timescale and expansion velocity, with R_i the initial radius of the expanding plasma. Δt_{peak} is the delay between the peaks of the model X-ray lightcurve and L'-band lightcurve (the X-ray lightcurve always peaks first). fwhm$_X$ and fwhm$_L$ are the full width half maximum widths of the X-ray and L'-band lightcurves, respectively. The injection profile in all models has the same FWHM of 27.5 minutes. In the adiabatic cooling models expansion begins at $t = 0$. In all cases, the electron power-law index p is chosen so that peak X-ray and L'-band luminosities are comparable. The last row shows the observed delay and lightcurve widths for the April 4, 2007 flare (Dodds-Eden et al., 2009), calculated from the best fit Gaussians to the lightcurves (the values differ slightly from those given in Dodds-Eden et al., 2009, where the fwhm was measured directly from the lightcurves).

the premise that magnetic energy dissipation generates the particle acceleration that produces the flare in the first place.

We now explore two ways in which the magnetic field might change during the flare: (i) a stationary solar-flare-like model and (ii) an expanding plasma model (analogous to a CME; see §5.2). In addition to the motivation for considering a varying B given here, these two scenarios are also motivated by the numerical results discussed in §5.2.

5.3.3   Quasi-stationary Flare Model

Suppose that magnetic reconnection occurs somewhere in the inner regions of the accretion flow, as in Figure 5.1. In the region where the magnetic reconnection occurs the magnetic field decreases as magnetic energy is converted into the energy of accelerated particles. Here we consider a quasi-stationary flaring region like this that does not expand (so there are no adiabatic losses); this is applicable when the dissipated magnetic energy is smaller than the internal energy of the ambient accretion flow.

In Figure 5.5 we show several models in which electrons are injected into the emission region over a ~ 30 minute timescale, set by the duration of the X-ray flare. The models are compared to the NIR and X-ray lightcurves of the April 4, 2007 flare. Figure 5.5 shows three different models that all reproduce the NIR lightcurve reasonably well; the three models correspond to different values of $t_{\rm esc}$ (10, 30, & 200 min) and different $B(t)$. In this context, the escape of particles corresponds to accretion onto the black hole or escape in high speed outflows that do not emit significantly.

Figure 5.5 shows that if the magnetic field decreases from ~ 40 G at the beginning of the flare to $\sim$5-10 G at the peak of the flare, the simultaneity and symmetry of the NIR lightcurve, and the differences in duration of the NIR and X-ray lightcurves, are all reproduced reasonably well. For $t_{\rm esc} \gtrsim 30$ min, we find that B must continue to decrease after the peak of the flare (or at least level off) in order to not overproduce the NIR flux at late times. By contrast, for short escape times ~ 10 min (blue lines in Figure 5.5), there are so few electrons around at late times that the magnetic field must increase again in order to produce the observed emission. This increase in B at late times is reminescent of the numerical simulations in Figures 5.1 and 5.2, in which the accretion flow returns to its quasi-steady state after the flare comes to an end. More generally, if the emission is dominated by particles that remain in the flare region, rather than expanding outwards in an outflow, then a decrease in B followed by an increase is natural if magnetic energy is what generates the accelerated particles in the first place.

5.3.4   Expanding Plasma: a "Coronal Mass Ejection"

The change in magnetic field required to explain the NIR lightcurve in Figure 5.5 could be a consequence of outward expansion, rather than a local change in the magnetic field at a given position. Figure 5.6 shows an expansion profile $R(t)$ and $v(t)$ that can reproduce the properties of the NIR and X-ray flares, i.e., lightcurves like those in Figure 5.5 (we do not explicitly show the lightcurves and spectra for this model because they are similar to Fig. 5.5). The escape time is large for these models, $t_{\rm esc} = 1000$ min. Here we assume that the only change in the magnetic field is that produced by expansion, with $B \propto R^{-2}$. The expansion profile required to explain the NIR lightcurve is somewhat complicated, incorporating an acceleration, followed by
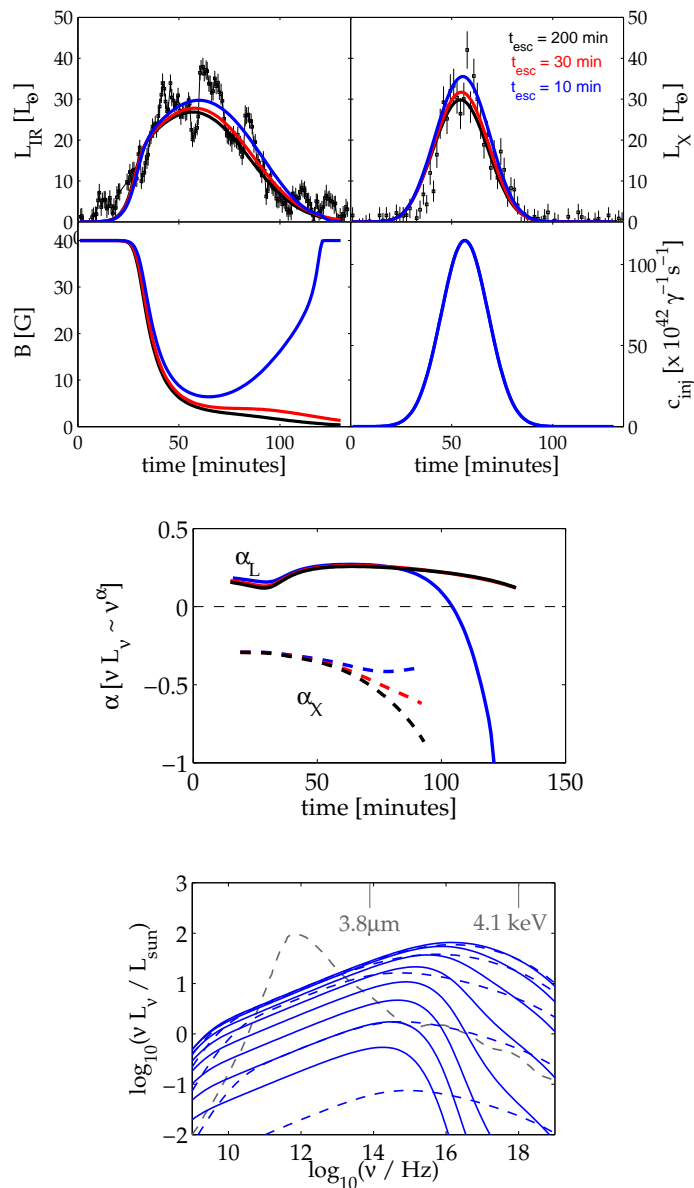
Figure 5.5 Stationary flare models with a decreasing magnetic field, envisioned to occur as a result of a magnetic reconnection in the inner regions of the accretion flow. We show results for three different escape timescales. The models are compared to the L'-band and X-ray data from the April 4, 2007 flare. *Top panel:* Model lightcurves, time dependent magnetic field and injection profiles. *Middle panel:* L'-band and X-ray spectral indices throughout the flare. *Lower panel:* The time-dependent SED for the $t_{esc} = 30$ min model. The dashed lines show the rising phase, while the solid blue lines show the subsequent evolution. The SED is plotted at 10 minute intervals. The quiescent model of Yuan et al. (2003) is plotted (dashed gray line) for reference. No optical depth effects are included in these models since we focus on the optically thin NIR to X-ray emission.
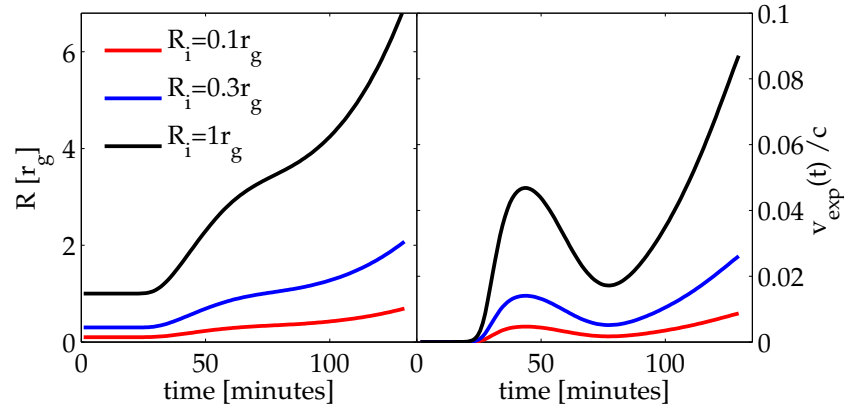
Figure 5.6 The expansion and velocity profiles $R(t)$ and $v_{\exp}(t)$ for a model which explains the NIR/X-ray lightcurves through adiabatic expansion; the magnetic field decrease is due solely to expansion with $B(R) \sim 1/R^2$. The lightcurves and magnetic field time dependence look very similar to the $t_{\mathrm{esc}} = 200$min model of Fig. 5.5 so we have not shown them here. The expansion profile has an acceleration followed by de-acceleration, followed by another acceleration. The variation is such that $1/t_{\exp} = d\ln R/dt (= v/R)$ is the same for different R_i.

deacceleration, followed again by an acceleration. This corresponds directly with the non-uniform variations in $B(t)$ required in Figure 5.5 (i.e. a sharp decrease in B during the rising phase of the flare, leveling off near the peak of the flare, thereafter decreasing once more). We suspect that in reality, the initial decrease in B required to account for the NIR lightcurve (at $t \lesssim 50$ min) is due to a sudden loss of magnetic energy (rather than expansion) – the later ($t \gtrsim 50$ min) expansion in Figure 5.6 may be due to slow expansion of the blob with the jet, as seen in the numerical simulations (see Fig. 5.2). The multi-dimensional expansion of the heated plasma in the simulations cannot be captured by the simple one-zone model considered here; the complexity in the expansion profile $v(t)$ required in Figure 5.6 may be a consequence of the limitations of this simple model.

We now consider models in which we fix the properties of the flare for the first ~ 100 min to be the same as in Figure 5.5, since this is what is required to explain the IR and X-ray emission. The NIR/X-ray flare is assumed to be static, but it sets the initial conditions for subsequent expansion (i.e., $B \simeq 5$ G and $N_e \simeq 10^{45}$). These calculations are motivated in part by observations that suggest a delay between longer wavelength (radio-mm) variations and the simultaneous NIR/X-ray events (Yusef-Zadeh et al., 2006b; Hornstein et al., 2007; Marrone et al. , 2008; Yusef-Zadeh et al., 2008; Meyer et al., 2008; Eckart et al., 2008b), where the delayed long wavelength emission might result from outflowing plasma (van der Laan, 1966).

The additional parameters determining the properties of later timescale emission are the initial size of the emitting region (prior to expansion), R_i, and the expansion speed $v_{\exp}$. The initial size R_i does not change the results of the NIR/X-ray emission because those wavelengths are optically thin (the flare emission only depends on the total number of accelerated particles N_e, not on R_i and the electron density n_e separately); however, lower frequency emission can
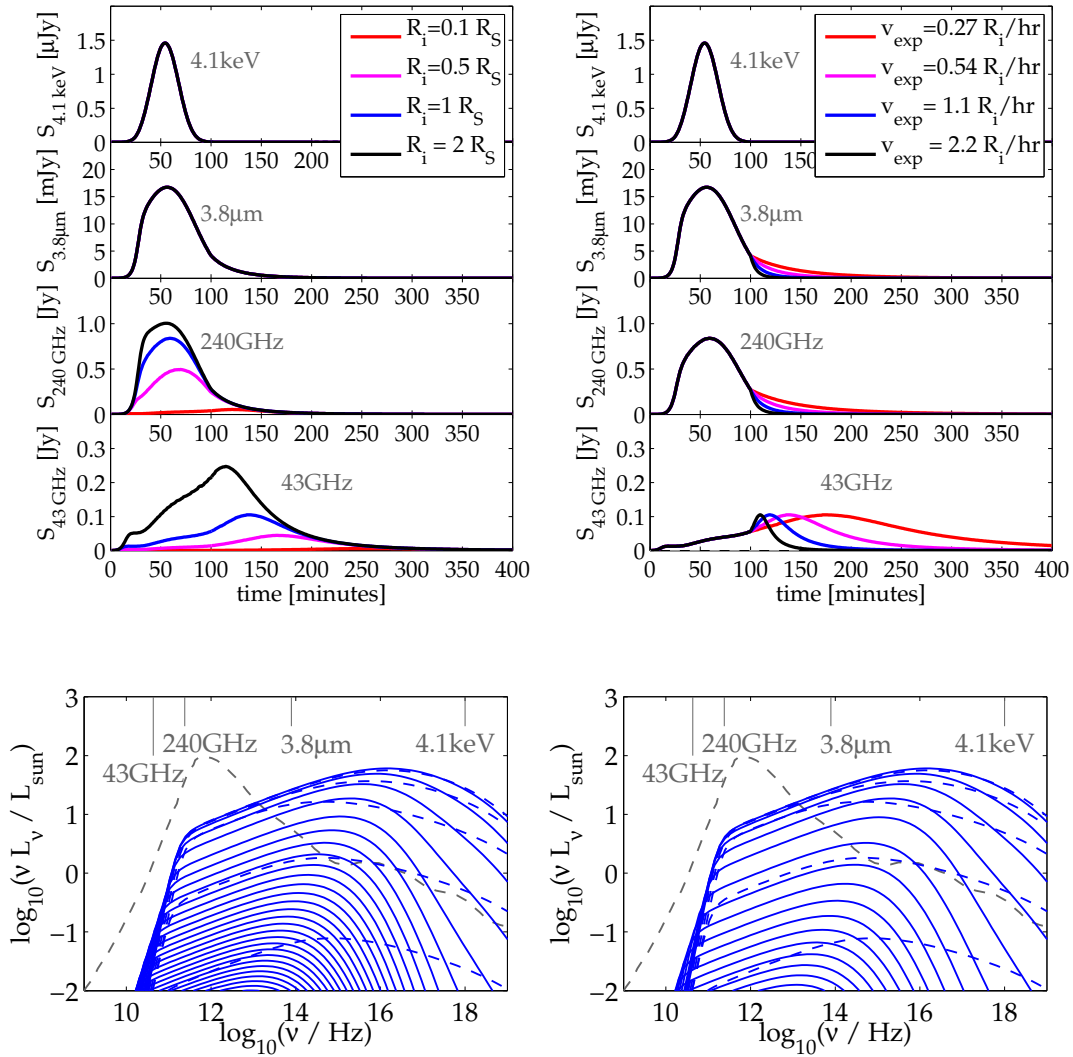
Figure 5.7 Adiabatic expansion models for radio-mm emission, including the effects of synchrotron self-absorption. The left panel shows the effect of varying R_i, the initial radius, the right panel the effect of different expansion speeds v_{exp} (see Figure 5.1 for the effects of different $B(R)$ and p). In contrast to the previous figures we plot all lightcurves in S_ν, for better comparison to the published mm/radio fluxes of the April 4, 2007 flare (the simultaneous 240 GHz flux was between $\sim$3-4 Jy; the 43 GHz radio flare, at a delay of 6 hours with a duration of 100 min, varied between $\sim 1.1 - 1.7$ Jy – see Fig. 5.10). The model from Section 5.3.3 with $p = 2.4$, $B(t_{peak}) \simeq 5G$ and $t_{esc} = 10000$ min sets the initial conditions for the expansion, which begins at $t = 100$ min. When not otherwise listed in the legend the model has $v_{exp} = 0.54R_i/$hr, $R_i = 1r_g$, and $B \propto 1/R^2$. The SED plots show the evolution of the SED with time for the model shown in blue in the upper panel; the dashed lines show the injection phase, while the solid blue lines show the subsequent evolution. The quiescent model of Yuan et al. (2003) is plotted (dashed gray line) for reference. The time-dependent SED is plotted at 10 minute intervals.
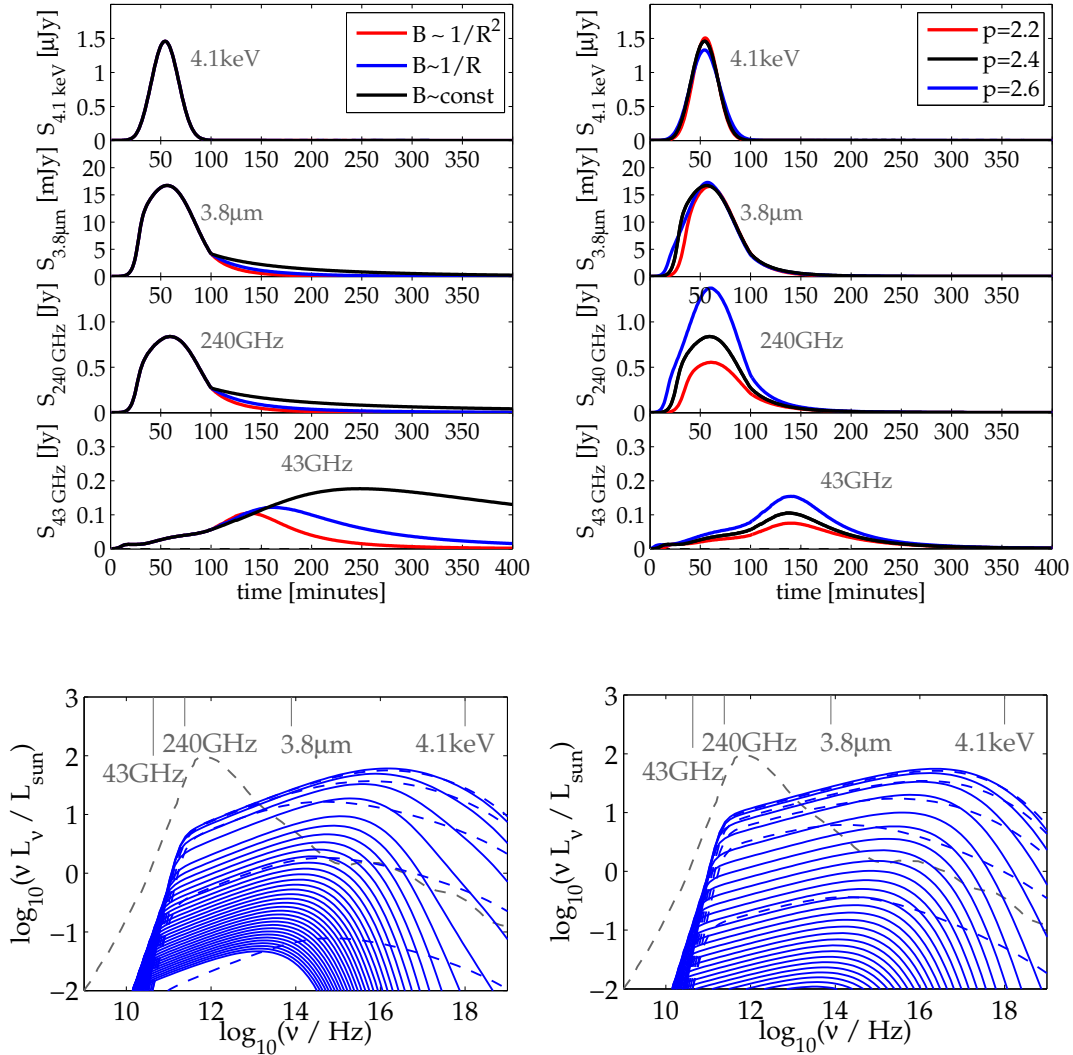
Figure 5.8 Adiabatic expansion models for radio-mm emission. The left panel shows the effect of varying different functions $B(R)$, the right panel the effect of different particle index p (see Figure 5.7 for the effects of different R_i and v_{exp}). For the left panel the model from Section 5.3.3 with $p = 2.4$, $B(t_{peak}) \simeq 5G$ and $t_{esc} = 10000$ min sets the initial conditions for the expansion, which begins at $t = 100$ min. For the right panel $B(t_{peak}) \simeq 11$ G and 2 G for $p = 2.2$ and $p = 2.6$ respectively. When not otherwise listed in the legend the model has $v_{exp} = 0.54R_i/hr$, $R_i = 1r_g$, and $B \propto 1/R^2$. See caption of Figure 5.7 for further explanation.

become self-absorbed, which introduces a dependence on R_i.

Figures 5.7 and 5.8 shows lightcurves and time-dependent SEDs for models which fit the NIR/X-ray lightcurves of the April 4, 2007 flare, but in which we also initiated expansion at $t \approx 100$ minutes. Unlike in §5.3.3, here we set the escape time to $t_{\mathrm{esc}} = 2000$ min, so that no electrons escape on any timescales of interest; this is motivated by the fact that we are now following the thermodynamics of the expanding electrons. In Figure 5.7 we show the effects of considering different values of R_i and v_{exp}, while Figure 5.8 shows the effects of changing the power-law index of the injected electrons p, as well as the effect of different functional forms for $B(R)$, relaxing the assumption we made previously of expansion in a purely radial field ($B \sim 1/R^2$).

One prominent feature of the model lightcurves in Figures 5.7 and 5.8 is that there is in general no delayed mm emission; this is because the flare is optically thin at mm wavelengths (240 GHz). The low optical depth is partially due to the low initial magnetic field of 5 G (vs., say, 30 G) but more importantly it is because of the low electron densities. The only one of our models to show a delayed flare at mm wavelengths has $R_i = 0.1r_g$ and thus an electron density of $n_e \simeq 10^{11} \mathrm{cm}^{-3}$. There are, however, independent observational arguments in favor of ambient densities $n_e \sim 10^7 - 10^8$ cm^{-3} near Sgr A* (see Bower et al. 2003; Marrone et al. 2007). For $N_e \sim 10^{45}$ accelerated electrons inferred from the X-ray and NIR flares, we require $R_i \sim$ 1-2r_g to have $n_e = 10^7 - 10^8 \mathrm{cm}^{-3}$ (see §5.3.5). Figures 5.7 and 5.8 show that for this size, the accelerated particles produce a simultaneous, rather than delayed, mm flare – this is a robust conclusion that is true for all expansion speeds, magnetic field geometries, etc. Increasing the initial magnetic field strength to ~ 30 G also does not qualitatively change this conclusion. [1]

In contrast to the optically thin mm emission, Figures 5.7 and 5.8 show that our models predict that there could be optically thick flares at 43 GHz delayed by $\sim 100 - 200$ min relative to the NIR and X-ray emission. Indeed, due to lack of coverage at 43 GHz until 250 min after the flare, we cannot rule out that such a delayed flare occurred for the April 4, 2007 event. However, the delayed flares in our models typically have peak fluxes of only $\sim$0.1-0.25 Jy for initial sizes of 1-2 r_g, and would be barely noticeable.

The flux of delayed radio emission is largest under one of two conditions. First, it is larger if the magnetic field decreases more slowly as the plasma expands (e.g., if $B \propto R^{-1}$ instead of $B \propto R^{-2}$, or even $B \propto$ const, which corresponds to expansion in a purely vertical magnetic field geometry); see the left panel in Figure 5.8. Secondly, the radio flux is also larger if there is a significant population of lower energy electrons, which do not emit in the mm to X-ray, but can emit at lower frequencies. This is demonstrated explicitly in the right panel of Figure 5.8, which

---

[1]For example, the following equations for the self-absorption frequency, adapted from Gould (1979), show that upon substituting the values from Table 5.1 for both a $B \approx 5$ G model (the decreasing B model with $t_{esc} = 30$ min) and a $B = 30$ G model (a synchrotron cooling model) which produce the correct peak fluxes to match the NIR and the X-ray flare, the self-absorption frequency is only $\nu_{SSA} \approx 180 - 220$ GHz ($\lambda \approx 1.3$ mm) in both cases:

$$\nu_{SSA}(p = 2.4, \gamma_{\mathrm{min}} = 10) = 2.2 \times 10^{11} \text{ Hz } \left(\frac{B}{5.6\mathrm{G}}\right)^{21/31} \left(\frac{N_e}{2.5 \times 10^{45} \text{ electrons}}\right)^{10/31} \left(\frac{R}{1.5R_S}\right)^{-20/31}$$

$$\nu_{SSA}(p = 1.95, \gamma_{\mathrm{min}} = 10) = 1.8 \times 10^{11} \text{ Hz } \left(\frac{B}{30\mathrm{G}}\right)^{3.95/5.95} \left(\frac{N_e}{0.026 \times 10^{45} \text{ electrons}}\right)^{2/5.95} \left(\frac{R}{1.5R_S}\right)^{-4/5.95}$$

shows that the delayed radio flux is larger for larger values of the electron power-law index p. Large values of $p \gtrsim 2.6$, however, become inconsistent with the NIR and X-ray fluxes and spectral indices. In addition $p \gtrsim 2.6$ imply a simultaneous mm flare of > 1 Jy; such large simultaneous variations in the mm flux are not observed (see Fig 5.10 below).

The observed April 4, 2007 flare from Sgr A* was followed by an increase in the 43 GHz flux to ~ 1.5 Jy, ~ 400 min after the flare (Yusef-Zadeh et al., 2009). Our results in Figures 5.7 and 5.8 demonstrate that this increase in the radio flux cannot be due to immediate expansion of the particles that produced the NIR and X-ray emission. This does not, of course, rule out that the two different "flares" are causally connected. For example, the expanding plasma that produced the NIR to X-ray emission could be reaccelerated as it moves outwards (e.g., via shocks), increasing the emission at later times above that predicted by our models.

The slow speeds required to produce delayed flares of ~ 100 minutes are also much smaller than the escape speed close to the black hole, as has been noted in previous work (Yusef-Zadeh et al., 2006b; Marrone et al. , 2008). It is also apparent in comparing our model lightcurves with the observations (compare the right panel of Figure 5.7 with the 43 GHz observations in Figure 5.10) that these slow speeds are at odds with the relatively short duration of the observed 43 Ghz flare (compared to the length of the delay). It could be the case that the expansion of the plasma does not begin until well after the NIR and X-ray emission cease, such that a shorter duration lightcurve can be produced at longer delay. Indeed, the viscous time in the inner parts of the accretion disk is likely ~ 10 dynamical times ~ 200 min. Thus if the accelerated particles are not initially overpressurized (so that they do not expand on a dynamical time), they could be advected out in the 'quiescent' outflow after a few viscous times, producing – with some re-acceleration – delayed radio emission on approximately the correct timescale. However, it is clear that significant fine-tuning and extra physics is required to explain the delayed radio flare of April 4, 2007 (Yusef-Zadeh et al., 2009) via an adiabatic expansion initiated by the NIR/X-ray flare.

5.3.5   Energetics and the Size of the Emitting Region

The total energy supplied to electrons with $\gamma \gtrsim \gamma_{min} = 10$ in our $p = 2.4$ model that reproduces the bright NIR and X-ray flare from Sgr A* is

$$\Delta E \approx 3 \times 10^{39} \text{ erg}$$

In the same model, the magnetic field decreases from ~ 40G to ~ 5G (see Figure 5.5). For the magnetic energy decrease itself to power the flare the decrease must occur in a region with a size

$$R \gtrsim \left(\frac{6\Delta E}{\Delta B^2} \right)^{1/3} \approx 1.5 \ r_g, \tag{5.10}$$

where the equality requires that the magnetic energy is converted into electron energy with 100 % efficiency. A large efficiency may not be unreasonable: in solar flares a large fraction of the released energy appears to go into particle acceleration (Lin et al. 2003). Also note that magnetic dissipation may occur over a volume much bigger than that of the current sheet where particle acceleration happens (see Figs. 5.1 & 5.2).

There are independent constraints on the size of the flaring region. For example, the requirement that *hard* synchrotron self-Compton emission should be sub-dominant in the X-rays (reminding that soft SSC only occurs for extreme magnetic fields and densities; Dodds-Eden et al.,

2009) puts a lower limit on the size of the emission region of $R \gtrsim 1r_g$. More quantitatively, we find the SSC component contributes to 30%, 16% and 9% of the total X-ray flux for $R = 1r_g, 1.5r_g$ and $2r_g$, respectively.[2] An approximate upper limit on the size of the flaring region comes from short timescale variations in the lightcurve of the April 4 event: these constrain 30% of the flux to come from a region with $R \lesssim 1.2r_g$. In addition, the total number of accelerated electrons required to produce the flare, together with independent estimates of the ambient electron density, favor a size of $R \sim 1.5 - 2r_g$. Specifically, for $R = 1r_g$ and $\gamma_{\min} = 10$, we require a local density of accelerated particles of $n_e \approx 2 - 8 \times 10^8 \text{cm}^{-3}$ depending on the escape timescale; this is larger than the ambient density $\sim 10^7 \text{ cm}^{-3}$ estimated from modeling the 'quiescent' emission and the observed Faraday rotation (e.g., Yuan et al. 2003). By contrast, for $R = 2r_g$ and/or somewhat higher $\gamma_{\min}$, we find better consistency with the ambient density estimates.

Taken together, a flaring region with a size $\simeq 1.5 - 2 \ r_g$ is implied by the observed properties of the NIR and X-ray flare, the ambient density constraint, and the energetics of the flare (eq. 5.10). This is also similar to the size of the region in the MHD simulations in which the magnetic energy decreases dramatically and the plasma is heated (§5.2).

5.3.6 Effect of the Decreasing Magnetic Field on the Steady State Emission

Our calculations demonstrate that longer wavelength delayed flares from adiabatic expansion of the initially accelerated particles are relatively faint and may be difficult to detect. However, there is another important implication of this model for longer wavelength emission.

Given that the size of the emission region estimated in §5.3.5 is comparable to the likely size of the sub-mm emitting region, if the magnetic field indeed decreases as we have argued here, the emissivity of the submm-emitting electrons could be significantly reduced (emissivity $\sim B^2$). We thus expect a *reduction* in the quiescent emission at submm wavelengths accompanying the NIR/X-ray flare. Note that this is also consistent with the MHD simulations, in which the magnetic field strength decreases over the entire inner region of the flow (the likely sub-mm emitting region; Fig. 5.1).

It is intriguing that there is such a dip in the 230/240 GHz emission following the bright NIR/X-ray event on April 4, 2007. This dip can be seen in Figure 5.10 (discussed below) and lasts for a total of $\approx$400 minutes. At its lowest the flux reaches ~ 1.7 Jy, significantly below the average mm flux of about 2.8-3 Jy (Zylka et al., 1995; Falcke et al., 1998; Zhao et al., 2003). It is also notable that this is the lowest flux measured for all 230-250 GHz observations (SMA, SMT and IRAM) of the April 2007 campaign (Yusef-Zadeh et al., 2009). After the dip the flux rises again and from 500 minutes reaches fluxes $\sim$3 Jy which are comparable with the average mm flux for Sgr A*. Possibly the radio 'flare' too, which rises around a similar time to the mm lightcurve, is also related to the recovery of the steady state emission, though it less clear that the magnetic field could be reduced over such a fraction of the radio-emitting region as to decrease the radio emission significantly.

If magnetic reconnection – accompanied by a simultaneous decrease in the field strength in the inner accretion flow – is the basis for the flares in Sgr A* in general, then this effect should be present in other flares. Previous work has suggested that submm flares follow NIR/X-ray flares by

---

[2]The IC emission produced by upscattering submm photons (assuming $R_{\text{submm}} \approx 4r_g$; Doeleman et al., 2008) contributes only 5-7% of the total X-ray flux for $R = 1 - 2r_g$, respectively.

∼100 minutes (Marrone et al. , 2008; Yusef-Zadeh et al., 2008; Meyer et al., 2008; Eckart et al., 2008b). However, our work raises the question of whether these submm variations are really flares at all – or is the rise in submm emission after ∼100 minutes simply the 'recovery' from the decreasing B that initiated the NIR/X-ray flare?

The data from previous observations are reasonably consistent with this interpretation. For example, the X-ray flare with apparent delayed mm/submm emission (1.3mm/850μm) published in Marrone et al. (2008) and Yusef-Zadeh et al. (2008) (Figs. 3 and 2, respectively) could easily be seen as a dip rather than a delayed flare. It is less clear whether the Ks-band flare at 6:00 UT published in Meyer et al. (2008) followed by a H/K'/L' flare at 8:00 UT simultaneous to observations at 1.3mm (Hornstein et al., 2007; Marrone et al. , 2008) works well with a dip interpretation, but the 1.3 mm flux is slightly lower during the 6:00 UT Ks-band flare.[3] Finally, in Eckart et al. (2008b) (Fig. 4) there is a bright L'-band flare simultaneous with a pronounced dip in the 870μm emission observed with LABOCA/APEX. The bright initial peak in the NIR is followed by a sequence of smaller peaks: these subsequent peaks however appear to be accompanied by submm activity.

5.3.7   Lightcurve Substructure

Another intriguing feature of the observed April 4 flare is the substructure in the NIR lightcurve that is not present in the X-ray lightcurve. In the synchrotron model, this puzzling property is due to the different response of NIR and X-ray emitting particles to changes in the magnetic field. If there are magnetic field fluctuations, then the infrared emission (below the cooling break) will exhibit significant variations while the X-ray emission will be comparatively smooth because the cooling time for X-ray emitting particles is less than the injection time and so the X-ray luminosity is sensitive largely to the injection rate, not the magnetic field.

To quantify this, Figure 5.9 shows a model in which we introduce some variation in the magnetic field strength as a function of time (lower left panel); the basic parameters of this model are the same as the $t_{esc} = 30$ min model of Figure 5.5. The small changes in B in Figure 5.9 (∼ 15%) can produce the variable NIR emission observed, but they have comparatively little effect on the X-ray emission. Interestingly, the magnetic field changes do introduce some small structure in the X-ray lightcurve as well, at a time when the magnetic field strength is sufficiently low (few G) that the cooling time in the X-ray is comparable to the injection time. This matches a slight feature that is seen in the observed X-ray lightcurve. The same effect may also explain the sharp drops seen in the lightcurves of other bright X-ray flares from Sgr A* (Baganoff et al., 2001; Porquet et al., 2003). These could, of course, equally well be due to changes in particle acceleration. If, however, the result in Figure 5.9 is correct, it uniquely determines both the magnetic field strength at the peak of the flare (a few G) and the fact that the field strength must have been significantly larger earlier in the flare (on energetic grounds and via the fact that a low field strength throughout the flare is inconsistent with the data; see Fig. 5.3).

Figure 5.9 demonstrates that the observed substructure in the lightcurves from Sgr A* can be explained without requiring relativistic effects (that have been suggested previously; e.g., Genzel et al. 2003b). Our model also naturally accounts for the different short timescale variabil-

---

[3]this flare is also unusual compared to others in that neither NIR peak had an accompanying X-ray flare, despite simultaneous Chandra observations; and the 1.3mm flux appears to be generally high, ∼4-5 Jy, throughout the observation.
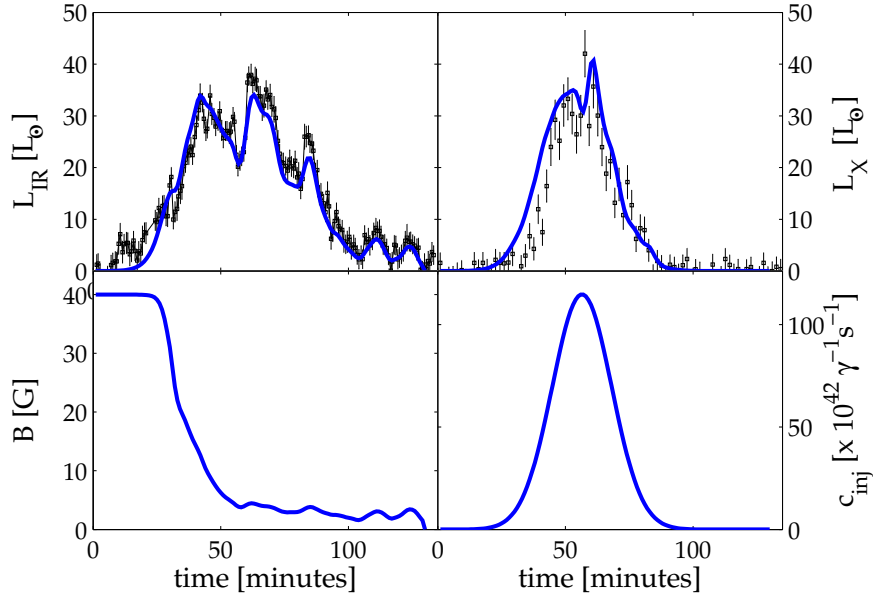
Figure 5.9 The $t_{esc} = 30$ min model of Figure 5.5, with the addition of small fluctuations in the magnetic field. These can reproduce the substructure seen in the NIR lightcurve, while the X-ray remains relatively unaffected because of the very short cooling time for electrons emitting in the X-ray.

ity observed in the NIR and X-ray as a consequence of the different synchrotron cooling timescales. The difference in substructure in the NIR and the X-ray lightcurves is not a priori unexpected if the lightcurve variations were due to relativistic effects, where one anticipates both NIR and X-ray emission should undergo similar amounts of beaming. However it is also not clear that the freshly injected electrons (emitting in X-rays) should have the same instantaneous dynamics as the bulk of the slower-cooling electrons (emitting in the NIR). Given that the timescales we are modeling correspond to multiple orbital periods at the last stable orbit, it is likely that some relativistic effects on the lightcurves must be present. Accordingly, because our model does not include any dynamics, we also cannot rule out that relativistic effects are important and modify the emission from what we find here. This will be studied in more detail in future work.

5.4   Conclusions

We have presented a model for the time-dependent non-thermal emission produced by transiently accelerated electrons in Sgr A*; although these calculations are in principle quite general, we have focused on the origin of the observed NIR and X-ray flares, and the likelihood of coincident or delayed longer wavelength emission. Our model is motivated by the hypothesis that dissipation of magnetic energy powers the flares, as is the case for solar flares and is believed to be the case in other systems like young stellar objects.

We have shown that episodic magnetic reconnection can occur near the last stable circular orbit in (non-relativistic) MHD simulations of accretion onto a central point mass (Figs. 5.1 & 5.2). This occurs when oppositely directed magnetic field lines are brought together by rapid inflow near the last stable orbit. The properties and statistics of these reconnection events depend, however, on the magnetic field we initialize in the disk at large radii. Thus a full understanding of whether such reconnection is indeed generic in RIAF models will require a better understanding of the large-scale magnetic field self-consistently generated in the accretion disk.

Motivated by the reconnection hypothesis, we developed a time-dependent, spatially one-zone, model for the acceleration and cooling of relativistic electrons under conditions appropriate to Sgr A*. Our model lacks the time-dependent dynamics and full general relativity of accretion disk simulations (e.g., Dexter, Agol, & Fragile 2009), but treats the electron distribution function in much greater detail. This is, we have argued, critical for understanding the NIR and X-ray emission produced by non-thermal particles.

Our calculations focus on the "cooling break synchrotron" model for the X-ray flares from Sgr A* (Dodds-Eden et al., 2009). In this model, both the NIR and X-ray emission are synchrotron emission. A cooling break between the NIR and X-ray causes the spectrum to steepen by $\Delta\alpha = 0.5$ ($\nu F_\nu \propto \nu^\alpha$); see Figures 5.3 and 5.4. This is consistent with the spectral indices of luminous flares from Sgr A*, in particular the very luminous and well-studied flare from April 4, 2007 (Dodds-Eden et al., 2009).

Figure 5.10 presents the overall picture we have developed for the April 4, 2007 flare. We summarize the findings from our modeling as follows:

5.4.1 Conclusions: NIR and X-ray

Model NIR and X-ray synchrotron lightcurves in which the rise and decay of the emission is governed solely by electron injection and energy loss (e.g., synchrotron cooling, adiabatic expansion, or escape) are either simultaneous and of similar duration, or the NIR lightcurve is delayed relative to, and longer than, the X-ray (the former occurs if the cooling time of NIR-emitting electrons is short compared to the timescale on which relativistic particles are injected, the latter if it is long). Simultaneous lightcurves of different duration - as is observed for luminous flares from Sgr A* – do not occur for fixed plasma parameters during the flare.

The interplay between electron acceleration, synchrotron cooling, and magnetic field evolution during the flare can produce a model that matches both the average SED and NIR/X-ray lightcurves of the luminous flares from Sgr A* (e.g., that of April 4, 2007). In particular, a magnetic field decrease by a factor of $\sim 3-10$ accompanying the injection of relativistic particles can explain the observational result that the NIR and X-ray lightcurves are simultaneous, but of different duration (Fig. 5.5). This is consistent with the hypothesis that magnetic energy dissipation powers the flare in the first place.

Furthermore, small magnetic field fluctuations can reproduce the lightcurve substructure seen in the NIR lightcurve without producing substructures of similar magnitude in the X-ray. This is because the synchrotron cooling time is typically so short in the X-ray that the emission depends primarily on the rate at which electrons are accelerated, and is relatively independent of the magnetic field strength; the same is not true for electrons emitting in the NIR, where the cooling time is longer.

A general decrease in the magnetic field (that is not so smooth, i.e. with fluctuations) can
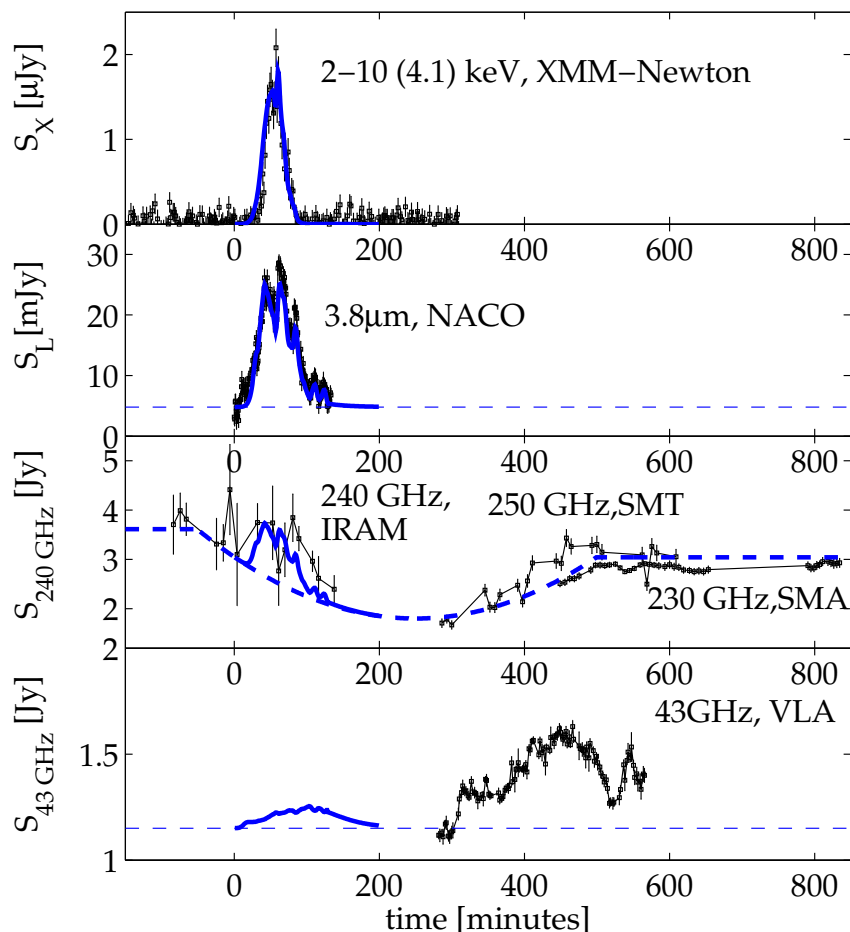
Figure 5.10 Our summary model for the April 4, 2007 flare. The size of the flaring region is $1.5r_g$. The X-ray and L'-band lightcurves are those shown in Figure 5.9. We also show the emission at 230 GHz, which is optically thin. In addition to the flare emission we show a schematic lightcurve for the "quiescent" emission (dashed line) which decreases due to the decrease in magnetic field associated with the flare. The steady state emission is re-established after ~ 400 minutes. There is a faint (~ 0.1 Jy) radio flare with a delay ~ 50 min from the peak of the X-ray/L'-band flare, insufficient to explain the observed radio flare at ~ 500 min. The latter may be due to additional particle acceleration in an outflow initiated by the NIR-X-ray flare.

also be responsible for sharp drops observed near the peaks of X-ray flares from Sgr A*, an effect which results from the cooling break reaching X-ray wavelengths. In summary, we find that with the detailed time-dependence of the magnetic field alone (the energy injection may be rather smooth), one can reproduce all the observed time-dependent features of the simultaneous lightcurves.

These models predict very little spectral evolution in the NIR and X-ray during the flare, except perhaps some reddening at the very end of the NIR flare, when the flux is $\sim 10\%$ of its peak value (Fig. 5.5). Marrone et al. (2008) argued that the dominant process governing the rise and decay of the flare emission had to be energy-independent, citing the relative stability of the NIR spectral index with flux (Hornstein et al., 2007), consistent with our finding that there should be very little spectral evolution. However, at the lowest fluxes some authors see a trend towards redder NIR spectra (Gillessen et al., 2006), which in the context of our model could be a sign of the cooling break crossing the NIR bandpass.

5.4.2   Conclusions: Millimeter and radio

We have also studied the emission produced by the adiabatic expansion of plasma during, and after, the NIR and X-ray flare. In our MHD accretion disk simulations, we find that in some cases dissipation of magnetic energy leads to over-pressurized plasma that rapidly expands outwards, analogous to a coronal mass ejection in the sun (Figs. 5.1 & 5.2). It is thus possible that the magnetic field decrease required to account for the differences between the NIR and X-ray lightcurves (in the synchrotron model) could be due to outward expansion of the plasma initiated by the flare itself (Fig. 5.6). In addition to the decrease in magnetic field strength, the magnetic field geometry also changes during the magnetic reconnection event (Fig. 5.1). This change in magnetic geometry can result in substantial changes in the polarization angle during the NIR flare, as was as observed by Trippe et al. (2007) and Meyer et al. (2006).

In our calculations, we find that the flaring region is unlikely to be self-absorbed at ~ 240 GHz. As a result, even though the plasma is expanding outwards at late times, there is no delayed flare at ~ 240 GHz. Our models do predict that at ~ 43 GHz, with adiabatic expansion there should be a delayed $\sim 0.1 - 0.2$ Jy flare $\sim 100 - 200$ min after the onset of the NIR and X-ray emission (Figures 5.7 and 5.8). This is, however, not sufficient to explain the April 4, 2007 radio (43 GHz) flare, which was delayed by 6 hours from the initial NIR/X-ray flare. Furthermore, in our simulations we have not included the additional absorption effect of thermal/non-thermal particles emitting the majority of the emission at submm/radio wavelengths, which could have the effect of suppressing the delayed emission even further, depending on the line of sight to the acceleration region through the accretion flow. These results argue against the radio flares as being produced by outward expulsion of the same relativistic electrons that produced the NIR and X-ray flare. This does not, however, preclude that the radio and NIR/X-ray flares are causally connected. The rise in the radio flux might be related to the disruption in the inner regions of the accretion flow caused by the loss of magnetic energy in the reconnection (as we suggest is the case for the mm emission), or it could be produced by in situ acceleration of particles in an outflow initiated during the NIR/X-ray flare (Liu et al. 2004). Along these lines, it could be reconnection events that are responsible for providing the non-thermal electrons required to produce the relatively flat spectrum observed in the radio for the quiescent state (e.g., Yuan et al. 2003).

Alternatively, it might be that radio flares are unrelated to the high energy particles of the NIR/X-ray flares. For example, it has been shown for the time-dependent jet model of Maitra et al. (2009) that the general spectrum, size measurements and rms variability of Sgr A* (from 7mm to 13 cm), as well as the simultaneous 22 and 43 GHz lightcurves of Yusef-Zadeh et al. (2008) can be explained simultaneously by a jet model with the variations explained by adiabatic expansion of overdensities in the jet. In this case the overdensities would likely arise through variations in the accretion rate, not necessarily linked to the acceleration of particles to high energy that occurs in the NIR/X-ray flares.

Our model makes a strong prediction for the mm emission associated with flares. In a strong magnetic reconnection event, the inner regions of the accretion flow are likely to be disrupted, with the magnetic energy decreasing in a significant portion of the submm-emitting region. We see this explicitly in our MHD accretion disk simulations (Figs. 5.1 & 5.2) and the energetics of the luminous flares from Sgr A* support this conclusion (§5.3.5). After a possible increase in emission due to particles accelerated during the flare, the mm flux should be suppressed by the decrease in the magnetic field in the inner regions of the accretion flow. We argue that there is evidence for such a decrease in the mm observations of the April 4, 2007 flare. The mm flux will recover to its quiescent value when the steady state accretion flow itself readjusts; the timescale for such a recovery is set by the viscous time in the inner parts of the accretion flow which is disrupted. This is somewhat uncertain, but ~ 3 hours (Fig. 5.1). It is likely that the 'dip' and 'delay' in the sub-mm flux will be larger for stronger X-ray/IR flares because the stronger flares correspond to the disruption of a larger part of the quiescent accretion flow.

5.4.3 Final Remarks

Although we believe that the model summarized in Figure 5.10 is theoretically well-motivated (Fig. 5.1 & 5.2) and reproduces the spectral properties and lightcurves of the luminous flares from Sgr A*, it is by no means certain that it is the only explanation. For example, we have assumed throughout this paper that particle acceleration produces a power-law distribution of electrons $\propto \gamma^{-p}$ from $\gamma \sim 10 - 10^6$, with the electron spectral index p independent of time. If however, the injection spectrum varied with time this could in principle alter some of our conclusions.

We have also not considered the possible effects of inverse Compton (IC) cooling on the time-dependent spectrum of electrons. The amount of IC cooling depends on the production rate of inverse Compton scattered photons, which depends on the size of the flaring region. For region sizes $\approx$1.5-2R_S (see Section 5.3.5) synchrotron cooling dominates for the photon densities typical of the flare peak for magnetic fields above $\approx 5 - 7$ G (i.e. while $U_{\rm B} > U_{\rm ph}$, assuming all scattering is in the Thompson limit). Thus synchrotron cooling will be the dominant effect in the rising phase of the flare while the magnetic field is still high. IC cooling may then start to play some role near the peak of the flare where the photon density is high and the magnetic field has decreased to ≈ 5 G such that $U_{\rm B} \approx U_{\rm ph}$. However the magnitude of the effect is not likely to be as large as would be estimated using the approximation from the Thompson limit, since photons scattered from $\gamma_c \sim 10^4$ electrons are already in the Klein-Nishina regime where scattering is less effective for $\nu \gtrsim mc^2/(h\gamma) \approx 10^{16}$ Hz (Rybicki & Lightman, 1986). Klein-Nishina effects will then suppress the amount of IC cooling of electrons emitting synchrotron at X-ray wavelengths (depending on the details, the X-ray spectrum may even be fully restored to a synchrotron cooling only regime, see e.g. Nakar et al. 2009). Implementation of IC cooling including the full Klein-

Nishina effects requires additional modeling, which we would like to fully explore in future work. Note, however, that (i) the effect of IC cooling produces similar breaks in the spectrum to that of synchrotron cooling so there will be no significant change in the spectrum near the peak of the flare if IC cooling starts to play a role, and (ii) the neglect of IC cooling does not change our main result – the decrease in magnetic field required to explain the simultaneous *rising* phases of the NIR/X-ray lightcurves – since synchrotron cooling dominates in the rising phase of the lightcurve.

Future multi-wavelength observations of flares from Sgr A* will enable us to build statistics and to understand whether the properties of the April 4, 2007 flare are common to Sgr A* flares in general. In the context of synchrotron emission, the fact that the NIR and X-ray lightcurves have different widths and rise times depends on details of the model, such as the escape time or how much the magnetic field decreases during the flare. *A priori* we would thus expect variation in the lightcurve properties from flare to flare. However, one might expect a trend for the peak NIR/X-ray ratio for flares to increase generally for smaller flares, which have a less dramatic magnetic field decrease. For smaller flares, it might then be possible that inverse Compton emission with a harder spectral index dominates the X-ray emission instead.

The relative spectra in the NIR and X-ray are also critical for constraining the theoretical models: it is primarily the combination of the hard NIR spectrum ($\nu L_\nu \propto \nu^{0.4}$) and the soft X-ray spectrum ($\nu L_\nu \propto \nu^{-0.3}$) that rules out IC emission as the origin of the luminous X-ray flares, favoring synchrotron emission instead (Dodds-Eden et al., 2009). The hard NIR spectrum is also what requires efficient acceleration of non-thermal electrons with $p \simeq 2 - 2.4$ near $\gamma \sim 10^3$ ($n(\gamma) \propto \gamma^{-p}$), rather than simply a modest extension of the mm-emitting thermal distribution function (which would predict a relatively red NIR spectrum; Yuan et al. 2003). It is thus critical to understand the spectrum of the NIR emission and whether it depends on flux. At longer wavelengths, it is particularly important to understand the magnitude of the submm flux during and just after NIR/X-ray flares, as compared to times of no NIR or X-ray activity.

In the long term, better understanding the flares from Sgr A* will hopefully enable us to use such time dependent emission as a probe of accretion and outflow physics, and potentially strong gravity. Moreover, understanding the flaring emission in addition to the quasi-steady emission will further refine what physics must be included in time-dependent general relativistic MHD simulations (i.e., as concerns the production of non-thermal particles) in order to explain and predict the emission from Sgr A*.

Chapter 6

Six year lightcurve from Sgr A*

Abstract: In this paper we examine properties of the variable source Sgr A* in the near-infrared (NIR) using a very extensive Ks-band data set from NACO/VLT observations taken 2004 to 2009. We investigate the variability of Sgr A* with two different photometric methods and analyze its flux distribution. We find Sgr A* is continuously variable (meaning the source is always 'on' and varying) in the near-infrared, and there also appears to be some medium-term variability on timescales of weeks to months. The flux distribution can be described by a lognormal distribution at low intrinsic fluxes ($\lesssim$ 5 mJy, dereddened with $A_{\mathrm{Ks}} = 2.5$). The lognormal distribution has a median flux of $\approx$1.6 mJy, but above 5 mJy the flux distribution is significantly flatter (high flux events are more common) than expected for the extrapolation of the lognormal distribution to high fluxes. We make a general identification of the low level emission above 5 mJy as *flaring* emission and of the low level emission as the *quiescent state*. We also report here the brightest Ks-band flare ever observed (from August 5th, 2008) which reached an intrinsic Ks-band flux of 27.5 mJy ($m_{\mathrm{Ks}} = 13.5$). This flare was a factor 27 increase over the median flux of Sgr A*, close to double the brightness of the star S2, and 40% brighter than the next brightest flare ever observed from Sgr A*.

6.1 Introduction

The *very* center of our galaxy houses the variable source named Sgr A*. This source, clearly associated with the supermassive black hole of $4 \times 10^6 M_\odot$ known to be present at the dynamical centre of our galaxy (Schödel et al., 2002; Ghez et al., 2008; Gillessen et al., 2009), is detected across the electromagnetic spectrum, at radio, submm, NIR and X-ray wavelengths. At NIR and X-ray wavelengths (Genzel et al., 2003b; Baganoff et al., 2001) the emission is highly variable (factors up to $\approx$160 and 27 in the X-ray and NIR respectively; Porquet et al. 2008, this work) compared to the comparatively steady emission at longer wavelengths. NIR peaks are detected

more often than in the X-ray (peaks occur ≈1 and 4 times a day for X-ray and NIR variable emission, respectively; Baganoff 2003; Eckart et al. 2006a). However, when both NIR and X-ray exhibit increases in emission, the peaks in emission occur simultaneously (e.g., Eckart et al., 2004; Dodds-Eden et al., 2009).

The near-infrared lightcurves from Sgr A* exhibit ∼1 hour long increases in emission that are often called 'flares' in the literature. A number of these have exhibited very suggestive sub-structural features with timescales of ∼ 20 minutes (Genzel et al., 2003b; Eckart et al., 2006b; Trippe et al., 2007; Eckart et al., 2008a,b; Dodds-Eden et al., 2009), possibly quasi-periodic oscillations (QPOs). However the existence of QPOs and even the use of the term flare to describe the NIR variability of Sgr A* has been questioned by Do et al. (2009a) (see also Meyer et al. 2008 and Meyer et al. 2009) who argue that there is no true quasi-periodicity, just a variability process with a featureless red noise power spectrum (e.g. a power spectrum $P(f) \sim f^{-2}$ where f is frequency). A stochastic source with a red noise power spectrum has higher variability at longer timescales and could potentially be responsible for the structures on longer timescales seen in the real lightcurves. The authors suggest that apparent flare peaks may simply be the highest observed flux excursions in such a purely stochastic source and are not isolated events.

A main reason for the two rather contrasting interpretations of the variable emission from Sgr A* has been that the nature of the faint emission from Sgr A* and its relationship to the high flux emission is uncertain. The NIR emission from the Galactic Center is dominated by the central cluster of bright stars, and adaptive optics at 8-meter class telescopes is required in order to separate the faint source Sgr A* from the closest S-stars (even at this resolution Sgr A* is still on occasion confused with a relatively bright star). Additional, faint stars may be present very close to Sgr A* which have not yet been tracked and identified as stars from astrometric monitoring programs (e.g. Gillessen et al., 2009). While the dramatic high flux variability can be unambiguously attributed to the black hole, when a faint source is detected at the position of Sgr A*, it is not necessarily clear that the source is Sgr A*, faint stars, or a combination of both. Accordingly, it is not clear whether Sgr A* continues to emit at all at low fluxes, whether it exhibits a 'quiescent state' (a non- or weakly active low state), or whether the low flux emission continues to vary constantly with the same statistical properties as the high flux emission.

In addition to this, an unbiased overview of the properties of the near-infrared emission from Sgr A* can be difficult to obtain from the published literature because of publication bias (bright events have individual interest and are often published alone). However, some studies have looked at the statistical properties. Yusef-Zadeh et al. (2006a) and Yusef-Zadeh et al. (2009) presented lightcurves and flux distributions for Sgr A* for about ∼11 hours of 1.6μm and ∼32 hours of 1.7μm data observed with NICMOS on the Hubble Space Telescope (HST). With the resolution of the HST the close stellar sources are not as well separated from Sgr A* as with the VLT or Keck Telescopes, and the stars S17 and S2 overlap with the Sgr A* source in these observations. The flux distributions were fitted with a Gaussian at low fluxes, which was attributed to the observational noise on constant sources (the contribution from S2, S17 and possible quiescent emission) and a power-law at high fluxes, which was attributed to transient flares. The best fit models implied that Sgr A* was active (above the noise at low levels) more than 40% of the time.

Do et al. (2009a) presented an analysis of six nights of K'-band (and one L'-band) observations at the Keck Observatory, using an unbiased set of observations taken between 2005 and 2007. A source at the position of Sgr A* was always detected in this dataset, with an estimated maximum 35% contribution from stellar contamination. These authors also reported that the source Sgr

A* was continuously variable, based on the larger variance of Sgr A* compared to stars of similar brightness on five of the six K'-band observation nights. This was the data set used to investigate timing properties of Sgr A* in which it was claimed the data set was consistent with a featureless red noise power spectrum with no quasi-periodicity. However, with a sum duration for the K-band observations of about 12.1 hours, this data set did not sample well the higher fluxes of Sgr A*, i.e. the source was relatively faint compared to publications where variable emission with suggestive quasi-periodic structure have been reported (Genzel et al., 2003b; Trippe et al., 2007; Eckart et al., 2008a, for a comparison of Ks-band peak emission from the literature see Tables 6.1 and 6.2). Although the studies of Yusef-Zadeh et al. (2006a), Yusef-Zadeh et al. (2009) and Do et al. (2009a) have gone some way towards understanding the statistical properties of Sgr A* in the near-infrared, there has not yet been a study on a very large, unbiased dataset of the variability of Sgr A* where the rare high fluxes are also well sampled.

In this paper, we analyse the Ks-band flux distribution of Sgr A* for the years 2004-2009 from 117 observation nights carried out with the VLT in Paranal, Chile with the aim of seeking the flux-dependent characteristics of the variability of Sgr A* at both high and low fluxes. We do this through investigation of the flux distribution of Sgr A*. The dataset of this paper is ∼12 times larger than the data set of Do et al. (2009a). In order that our results might be compared with other publications, we give a summary in Tables 6.1 and 6.2 of the brightest and/or notable Ks/K'-band variable emission reported in the literature, as well as the faintest values or upper limits. All are reported in the literature with different calibrations/extinction values, and we have done our best to determine the corrections to scale them to the calibration and extinction values used in this paper.

In Section 6.2 we present our observations and the results of using two different methods of photometry: a six year lightcurve (aperture photometry), and the 2009 data set (PSF photometry). In Section 6.3 we present the flux distribution of Sgr A* and our results from various model fits to the flux distribution. In Section 6.4 we discuss our results in the context of two variability states for Sgr A*: a low-level lognormally varying *quiescent state* and sporadic high flux *flares*. We summarize in Section 6.5.

6.2   Data

Since 2002 we have observed the Galactic Center with the near-infrared adaptive optics-assisted diffraction limited imager NACO at the VLT (Lenzen et al., 2003; Rousset et al., 2003). Much of the observation time 2002-2009 was spent concentrated on the central few arcseconds, measuring the positions of the S-stars and monitoring Sgr A*. By now we have amassed a large dataset with which we can investigate statistical properties of Sgr A*'s variability. While we utilised L' (3.8μm), Ks (2.18μm) and H (1.66μm) bands, by far the largest proportion of our data is taken in Ks-band, collected in either 13 mas pix imaging, 13 mas pix polarimetry, or 27 mas pix imaging mode.

The presence of many stars close to the central black hole complicates the attempt to acquire accurate photometry for the near-infrared Sgr A* source. Sgr A* is usually fainter than the surrounding S-stars, and the stars *move*. A star can on occasion get so close to Sgr A* in projection that the two sources become confused. For example, the ∼16 year orbit star S2 (Ghez et al., 2008; Gillessen et al., 2009) was confused with Sgr A* as it passed pericenter in 2002. More recently, the $m_{Ks} \approx 15.8$ mag star S17 was confused with Sgr A* in 2006-2008.

Table 6.1.   Flux comparison of Sgr A* reported in the literature: I. bright states

Reference	Obs. Date	Reported flux [dered mJy]	Photometric calibration rescaling factor	Extinction rescaling factor	Rescaled flux [dered mJy]
Brightest States		*Peak fluxes*			
Gen+03	15 Jun 2003	13.2 (10.5+2.7)	1.10	0.76	11.0
Gen+03	16 Jun 2003	10 (7.3+2.7)	1.10	0.76	8.4
Mey+07	6 Oct 2003	22[a]	1.2	0.76	20.1
Tri+07/Mey+06	31 May 2006	16/23 (+S17)	-	-	(16.7) 13.5[b]
Hor+07	31 Jul 2005	11.6	$\sim$1.06[c]	0.52	6.4
	2 May 2006	26.8	"	"	14.8
	17 Jul 2006	6.8	"	"	3.7
Do+08	3 May 2006	0.8	$\sim$1.06[c]	-	8.5
	20 Jun 2006	0.65	"	"	6.9
	21 Jun 2006	0.4	"	"	4.2
	17 Jul 2006	0.3	"	"	3.2
	18 May 2007	0.6	"	"	6.4
	12 Aug 2007	0.2	"	"	2.1
Eck+08	15 May 2007	24 (+S17)	0.76	0.76	(13.9) 10.7
this work	5 Aug 2008	30.7 (+S17)	-	-	(30.7) 27.5

Note. — Reported fluxes from the literature for high flux states of Sgr A* in the literature, rescaled to match the photometric calibration and extinction used in this paper (where S65 has $m_{Ks} = 13.7$ and $A_{Ks} = 2.5$; see text for details). For the rescaled fluxes, brackets denote the raw observed flux (including S17) and the value without brackets the S17-subtracted estimate of the intrinsic flux. Note that without more detailed analysis we have only been able to reasonably account for and subtract the contribution of S17, and not any fainter stars: thus in the rescaled fluxes quoted here there may still be order of $1 - 2$ mJy stellar contribution to the flux.
[a] though the lightcurve shows a peak flux more like $\sim$24 mJy, this is likely an overestimate since the peak was only observed in one polarization filter (45°; see Figure 2 in Meyer et al. (2007). We take instead 22 mJy, which appears to be a better estimate of the integrated flux (i.e. $F_{45°} + F_{135°}$), according to the modeling of Meyer et al. (2007).
[b] we quote the value from our own photometry; this observation night was part of our 2004-2009 dataset.
[c] Scaling for -0.06 offset in absolute photometric calibration, assuming same calibration as Do et al. (2009b).

Table 6.2.   Flux comparison of Sgr A* reported in the literature: II. faint states

Reference	Obs. Date	Reported flux [dered mJy]	Photometric calibration rescaling factor	Extinction rescaling factor	Rescaled flux [dered mJy]
Faintest States					
Hor+02	9 May 2001	0.09 ± 0.005 mJy (upper limit, not dered)	$\sim 1.06^c$	-	0.95 ± 0.05
Sch+02	5 Jun 2006	2 ± 1 mJy	?	0.76	1.5 ± 0.8
Do+08	2006: May 3, Jun 20, 21, Jul 17 & 2007: May 18, Aug 12	0.192 mJy (median flux, not dered) 0.082 ± 0.017 (faintest flux, not dered)	1.06^d 1.06	- -	2.0 0.9 ± 0.2
Sab+10	23 Sep 2004	2.4 mJy (upper limit, no stellar contamination)	$0.88^e \times 0.90^f$	0.76	1.4
	23 Sep 2004	0.9 mJy (upper limit, full stellar contamination)			0.5

Note. — Reported fluxes from the literature for low flux states of Sgr A* in the literature, rescaled to match the photometric calibration and extinction used in this paper (where S65 has $m_{Ks} = 13.7$ and $A_{Ks} = 2.5$; see text for details). For the rescaled fluxes, brackets denote the raw observed flux (including S17) and the value without brackets the S17-subtracted estimate of the intrinsic flux. Note that without more detailed analysis we have only been able to reasonably account for and subtract the contribution of S17, and not any fainter stars: thus in the rescaled fluxes quoted here there may still be order of $1 - 2$ mJy stellar contribution to the flux.

[c] Scaling for -0.06 offset in absolute photometric calibration, assuming same calibration as Do et al. (2009b).

[d] Scaling for -0.06 offset in absolute photometric calibration (as determined from comparing magnitudes reported in Do et al. (2009b) and Gillessen et al. (2009), see also Sabha et al. (2010).

[e] Scaling for 0.14 mag offset in absolute photometric calibration (as determined from comparing magnitudes reported in Sabha et al. 2010 and Gillessen et al. 2009).
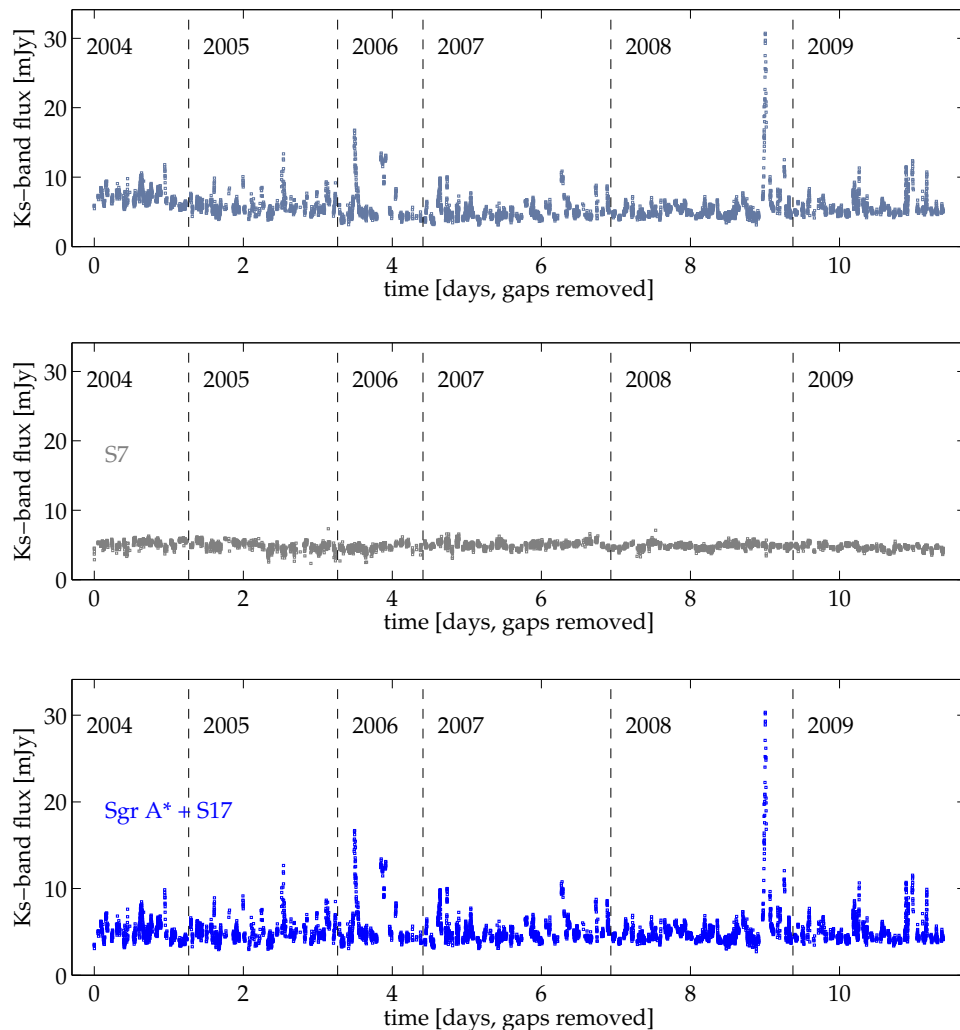
[f] Scaling for apparent different zeropoint.

Figure 6.1 Lightcurve of Sgr A* 2004 to 2009 from NACO Ks-band observations. The top panels shows the lightcurve of Sgr A* + S17, produced with aperture photometry, versus time with all gaps longer than 0.1 day removed. The second panel shows the lightcurve produced from the same data and with the same method for S7, a star of similar flux to the Sgr A*+S17 when faint. The source Sgr A*+S17 is more variable at low levels than the comparison source S7. In the lowest panel we show the detrended lightcurve, computed from subtraction of difference of the median value from each year, and the year of lowest median value (2006). We do this because there is good justification that the longest timescale trends of the source are dominated by additional faint passing stars (and in the case of 2004, extra flux in the aperture from the halo of S2 which was much closer in that year). Subtracted offsets are roughly 2.2 mJy in 2004, 0.9 mJy in 2005, 0 mJy in 2006, 0 mJy in 2007, 0.3 mJy in 2008 and 0.6 mJy in 2009.

We use two different methods in this paper:

1. We first attempted to obtain as large a homogeneous, unbiased, dataset as possible, in order to obtain a best overview of the statistical properties of the variability of Sgr A*, and to address in particular the variability at (the rarer) high fluxes. To do this we used aperture photometry because this allowed us to address the most important complication to the photometry of Sgr A* in 2004 to 2009 – the star S17, confused with Sgr A* in 2006-2008. To deal with S17 we used a two-aperture photometry method to determine the combined flux of Sgr A* and the star S17 in all years 2004 to 2009 with comparable accuracy. We did not include the Ks-band data from 2002-2003 because the star S2 was so close to Sgr A* during this time that it contributed to the flux measured with this method. Since S2 is much brighter than S17 the flux of Sgr A*+S17 could not be measured with an accuracy comparable to the other years.

2. We secondly looked at a subset of the data in more detail in order to address the nature of the variability at low fluxes. Determining the nature/existence of low level variability (and in particular to distinguish it from observational errors) requires more precise photometry than could be achieved with aperture photometry, in particular with the inclusion of S17. We address the question of the nature of the low level variability by analyzing the (high quality) 2009 data, in which S17 is not confused with Sgr A*, in greater detail with a PSF-fitting photometric method Starfinder, Diolaiti et al. 2000). Due mostly to the removal of the contribution of S17, the flux errors for this method are much smaller and allow us to ascertain whether there is true variability at low fluxes; however the data set is not completely unbiased since Sgr A* was only reliably detected in 87% of the selected images.

By using these two methods in combination, we can overcome the individual difficulties of the methods and piece together a consistent picture of the near-infrared variability of Sgr A*.

6.2.1 Aperture Photometry of Ks-band data 2004-2009

Our 2004-2009 Ks-band data set consists of $\approx$ 12000 images[1]. The data were reduced in the standard way by applying a sky subtraction, a flat field correction and a hot/dead pixel correction (see e.g., Trippe et al., 2007).

We found it necessary to apply a quality cut to eliminate the worst data and ensure we obtained a homogeneous data set on which we could perform accurate photometry. This quality cut was carried out by eye, and the criteria for elimination included:

(i) the two calibration stars were not in the image (this happened rarely, and only in the polarimetric data)

(ii) image ghosts close to Sgr A* or PSF artefacts

(iii) simply a bad quality image mostly corresponding to low Strehl ratio data resulting from poor atmospheric conditions. The quality of images for this criterion was judged by the general visibility of S-stars, not by the visibility of Sgr A* to avoid bias towards bright fluxes from Sgr A*.

---

[1]proposal IDs: 072.B-0285, 073.B-0084, 073.B-0775, 073.B-0085, 271.B-5019, 075.B-0093, 077.B-0014, 078.B-0136, 077.B-0552, 078.B-0136, 082.B-0952 and Large Programs 179.B-0261/.B-0932 and 183.B-0100.

We additionally eliminated 854 images from July in 2009 which were taken in a triggered mode, so that our dataset remains unbiased and representative of the overall variability of Sgr A*. The remaining data set totaled 6774 images which were used to obtain a lightcurve for Sgr A*.

To extract fluxes for Sgr A* as well as for several control stars, we carried out aperture photometry on each image. However, if we used a standard circular aperture centred on Sgr A*, we would have a varying contribution from S17 (the brightest star to be confused with Sgr A* 2004-2009) to the lightcurve as the star moves through the aperture during 2006-2008. A second star within the aperture, but not centered within the aperture also increases the error on our measurements of the flux of Sgr A*. We would obtain more accurate results if S17 could somehow also be well-centered in the aperture at all times, as well as Sgr A*.

To solve the problem of S17 we thus used a two-aperture method with two circular sub-apertures, one centered on Sgr A* and one centered on S17 and measure their combined flux, averaging the results where the two sub-apertures are each 40, 53 and 66 mas in size. We used this method for all data 2004 to 2009, so that we always measure the combined flux of S17 + Sgr A*. There are of course additional effects due to confusion with other, fainter stars but at first order our method ensures that we measure the fainter fluxes of Sgr A* with similar measurement errors from year to year than we would have if we neglected to include a sub-aperture about S17.

To further ensure the self-consistency of our dataset, we used the same set of calibrator stars for calibration of each image. This restricted us to only two suitable calibration stars, S30 and S65, due to the small field of view of some (especially polarimetric) images. To measure the raw counts of control stars and the calibration stars we used the same aperture as for Sgr A* and S17, but centered the star in just one of the two sub-apertures. For each image, the raw counts of Sgr A*/S17 and the control stars are then divided by the counts of the two calibrator stars and the calibrated counts are then flux calibrated by scaling relative to the median of S65 for the observation night, using $m_{\mathrm{Ks}} = 13.7$ for S65 (e.g. Gillessen et al., 2009). This photometric calibration is also consistent with Schödel et al. 2010 (S65: $m_{\mathrm{Ks}} = 13.64 \pm 0.02 \pm 0.06$). To convert magnitudes to fluxes (mJy) we used the zeropoint from Tokunaga (2000) ($m_{\mathrm{Ks}} = 0$ corresponds to 667 Jy).

We computed the expected positions of Sgr A* and of the control stars using the orbital (polynomial) fits of Gillessen et al. (2009). For our polarimetric data, we added raw counts from the ordinary and extraordinary images together for both target and calibration stars before flux calibration. We dereddened the final flux values using $A_{\mathrm{Ks}} = 2.5$ (Schödel et al., 2010, Fritz 2010 in prep.). Note that the absolute photometric calibration and extinction correction is not important for the analysis of relative fluxes presented in this paper, such that we have focused on maximising the long-term relative accuracy of our photometric measurements. However, where we compare with previous publications, we additionally scale the reported fluxes to the photometric calibration (as best as possible) and extinction of this paper.

The lightcurve we produced in this way for Sgr A* is shown in Figure 6.1. The data presented here is representative of the overall variability of Sgr A* since it is not biased towards the presence of obvious 'flare events' and the only data selection carried out concerned data quality and photometric consistency as explained above. It is by far the most extensive dataset for Sgr A* that has been published: the observations we present here consist effectively a ~184 hour long lightcurve (if one subtracts from the total time all gaps larger than about 20 min, i.e. gaps not due to sky observations). The total amount of exposure time (i.e. the time spent with the shutter open, excluding overheads) is smaller, and totals ≈72 hours, though 184 hours is a better
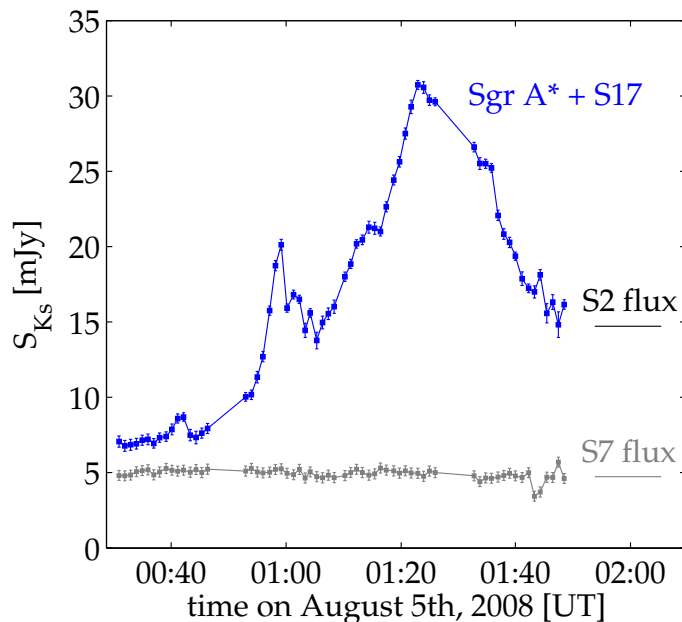
Figure 6.2 The August 5th, 2008, lightcurve. Sgr A* + S17 is shown in blue, and the lightcurve of the star S7 is shown for comparison. The flux has been dereddened with $A_{\mathrm{Ks}} = 2.5$. This flare is the brightest Ks-band flare that has ever been observed; the source reached an intrinsic peak flux of 27.5 mJy, a factor ≈ 1.7 the flux of the star S2. While the high flux excursion is preceded by what looks like a flatter, 'background' level of emission, this is however, at$\sim$7 mJy, several mJy brighter than the low flux levels from most other observation nights, and indicates there was increased source activity even at this time. The long-term trend for 2009 has not been subtracted from the lightcurve shown in this plot, and the last six datapoints did not make the data quality cut for the 2004-2009 flux distribution.

indication of the amount of continuous coverage.

We chose S7 to compare to Sgr A* because it is of similar brightness (to Sgr A* at low fluxes) and because it was reasonably isolated such that no other known stars crossed the aperture from 2004-2009 (the same double aperture was used to perform the photometry on S7 as for Sgr A*, with S7 centered in just one of the two sub-apertures). However, there is probably still more noise in the lightcurve measured for S7 compared to Sgr A* because of S7's location closer to the IRS16 cluster, for which the haloes of the brighter IRS16 stars can negatively affect the accuracy of the photometry.

Figure 6.1 shows the 2004-2009 lightcurve of Sgr A* and comparison star S7. On top of the more rapid variability, there is a general trend for the lowest fluxes of the lightcurve to wander from year to year. It is at its lowest in 2006. In 2004 the extra flux appears to be due to a

combination of a faint star[2], a contribution from the halo of S2, which was much closer to Sgr A* during that year, and S19, which was confused with S17. The lightcurve also shows some increased flux in 2008 and 2009; and as we will show in Section 6.2.1, there is at least one additional (previously unidentified) faint star which must also contribute to the increased flux in those years.

Since we can generally identify that stars are responsible there is good justification for subtracting these long (i.e. year) timescale trends from the lightcurve. For want of a better method of determining the stellar contribution to the lightcurves we subtracted the difference between the median of the data from each year and the minimum median value (in 2006). This brings the offset in the lightcurve to roughly 3.5-4 mJy, much of which can be reasonably attributed to S17 (between 2.9 and 3.3 mJy in the lightcurve can be attributed to S17; see Section 6.2.2).

It is apparent from Figure 6.1 that Sgr A* is much more variable than the comparison source S7. Some of the flux excursions are much more dramatic than others, with fluxes above 8 mJy ($\sim$5 mJy intrinsic upon subtraction of S17). Some of these have been previously published – for example, the second brightest peak of the dataset, in May 2006, was published previously in Meyer et al. (2006) & Trippe et al. (2007) and has 16.7 mJy ($\sim$13.5 mJy intrinsic; see Table 6.1).

On 5th August 2008, we saw a particularly extreme event which can be seen as the most dramatic flux excursion in the lightcurve in Figure 6.1. This event is also shown in higher time resolution in Figure 6.2. On this particular night the source at the position of Sgr A* brightened by a factor > 4 in a period of $\sim$40 minutes, reaching a peak flux of 30.7 mJy (intrinsic flux of $\approx$ 27.5 mJy minus S17, a factor increase over the upper limits on the lowest fluxes from Sgr A* of $\approx$27). An increase in Ks-band emission of this brightness is unparalleled in the literature for Sgr A*: the second brightest that has been published is a flare from October 2003 (Meyer et al., 2007) which reached an intrinsic flux of $\sim$20.1 mJy (see Table 6.1).

Stellar Contamination 2008-2009

To create the 2004-2009 flux distribution of Sgr A* we subtracted a trend from the data that we suspected to be due to faint stars. However the trend for higher fluxes in 2008-2009 can not be explained by any previously identified stars.

Here however we present evidence that there was indeed one to two faint stars confused with Sgr A* in the years 2007 to 2009. In Figure 6.3 we show that there are deviations in the source position of Sgr A* measured from imaging mosaics taken between 2007 and 2009. The systematic deviations imply there was at least one, previously unidentified, faint star confused with Sgr A*. In fact in new, very high quality observations of early 2010, it is possible to identify two new faint stars very close to Sgr A*. One or both of these stars may have undergone a close pericenter passage.

From Figure 6.3 it appears that one of the stars was present in 2007 also, while our offset for 2007 does not argue for any extra star. However as we discuss in Section 6.4.2 there appears to be a relatively steady $\sim$0.6-1.0 mJy stellar component to the flux of Sgr A*, which is probably made up of exactly such faint stars moving slowly in and out of confusion with Sgr A*: perhaps one of the newly discovered stars does indeed contribute to this stellar component in 2007 (and the increase in flux in 2009 may then be due to the second star).

---

[2]identified as S62 in Sabha et al. (2010), though we disagree with this identification (S. Gillessen, private communication)
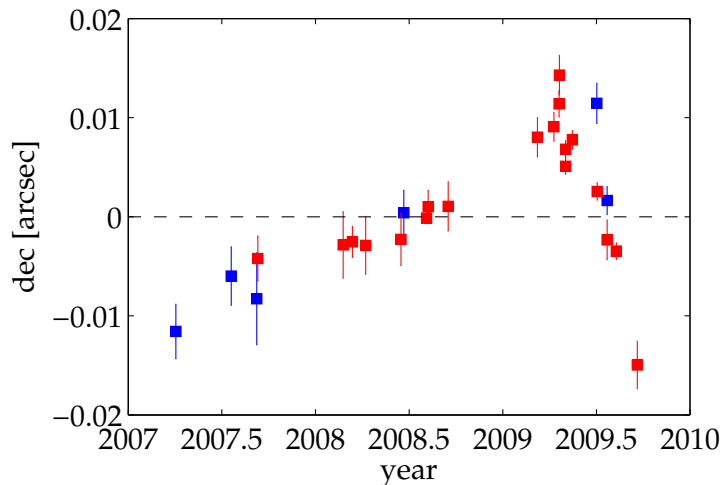
Figure 6.3 Deviations of the source position (in declination) for Sgr A* measured from (red) Ks-band and (blue) H-band imaging mosaics between 2007 and 2009. The clear deviations show that there was at least one contaminating star that may have been undergoing a close pericenter passage. Note that the measured deviations are dependent on the intrinsic fluxes of Sgr A*, which is variable, and the contaminating star. The zero position of the co-ordinate system is uncertain on the order of ∼2-3 mas; for the purposes of this plot the zero position of declination was fixed to the position for which the brightest flux from Sgr A* was recorded (the 27.5 mJy, $m_{Ks} = 13.5$ mag, event from August 5th, 2008).

It is somewhat a mystery why these stars have not been identified previously. The stars responsible for the observed deviations in the source position have not yet been identified in data prior to 2007 when they should have been resolved separately. Perhaps they have until now always been confused with other stellar sources. The star close to Sgr A* in 2004 (identified as S62 in Sabha et al., 2010, though we disagree with this identification) may be a candidate.

6.2.2 PSF photometry of Ks-band data from 2009

We additionally carried out PSF photometry on 2009 13 mas pix Ks-band data using Starfinder (Diolaiti et al., 2000), which we use especially for investigating the question of whether Sgr A* is continuously variable at low fluxes (Section 6.3.2). We use an automated program for running Starfinder on many images developed by Rank (2007). The measured fluxes were again calibrated on the S-star S65 ($m_{Ks} = 13.7$; Gillessen et al. 2009) and the results are shown in Figure 6.5. We note that due to the presence of the two previously unidentified faint stars (Section 6.2.1), we improve our chances of detecting a source in most images, while on the other hand the faintness of this additional stellar contribution ensures our flux measurements have very small error such that this data set is optimum for investigating the variability of Sgr A* at low fluxes.

To produce the lightcurve we first required that a faint S-star (S21, of ∼1.3 mJy) was detected in a given image as a basic data quality cut. From these images we then examined the detected positions of sources in the near neighbourhood (∼100 mas) of the nominal position of Sgr A* (see
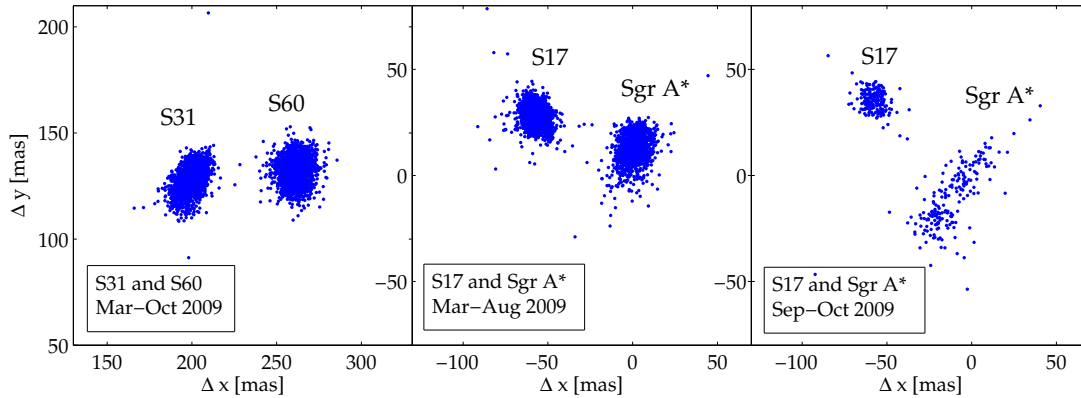
Figure 6.4 Detected positions using the Starfinder algorithm on 2009 Ks-band, 13 mas pix imaging data. S31 and S60 are two stars of similar separation and flux to S17 and Sgr A* when it is faint. Between March and August both S17 and Sgr A* are well-detected on the images; from September onwards however the contaminating star (see Section 6.2.1) begins to separate from Sgr A* and the photometry is unreliable.

Figure 6.4) and selected sources that were within 20mas of the mean position of this detected source (by this method a source was detected in 87% of the good quality selected images). Due to this method of source selection, the dataset we present here is not completely unbiased, due to the 13% of images in which no source was detected, but the fraction in which Sgr A* was not detected is small enough that the data set still serves well to assess whether Sgr A* is in general more variable than stars of comparable flux.

From the figure, Sgr A* certainly appears most of the time more variable than the comparison stars of similar flux (S21 and S60 in Figure 6.5). S60, in particular provides a very good comparison since it is also close to S31, a star of similar brightness to S17; the two sources S60 and S31 also have a very similar separation to Sgr A* and S17 during 2009 (see Figure 6.4). The flux distribution of S60 is fit by a Gaussian with $\mu = 1.309$ and $\sigma = 0.098$ which does not give any indication that the photometric accuracy is signficantly worse for sources of this separation and flux ratio (the more isolated star S21 is fit by a Gaussian with $\mu = 1.333$ and $\sigma = 0.090$).

In general the Starfinder and aperture photometry fluxes agree very well, with a constant offset of ~ 2.9 mJy. However, there is a systematic increase in the offset between the measured fluxes from the aperture photometry method and the Starfinder method towards the end of 2009, when the source(s) confused with Sgr A* has(have) moved the furthest to the south (see Section 6.2.1). This is likely explained by Starfinder's one-PSF fit to the distorted PSF of two sources (which has the effect of decreasing the flux measured with the Starfinder method); the sources are even beginning to become separated at the end of the year (see Figure 6.4).

This method also provides us with an estimate for the flux contribution of S17 to the 2004-2009 flux distribution. The offset of ~ 2.9 mJy, indicated by the black dashed line, is slightly fainter than the flux of S17 (3.3 ± 0.2 mJy when separated from Sgr A* in the 2009 data using Starfinder), which may be a result of the higher stellar background surrounding Sgr A* (i.e. in the background aperture) compared to the more isolated flux calibration star and/or a side effect of the double aperture method. Since the fluxes measured for Sgr A* may also be slightly fainter
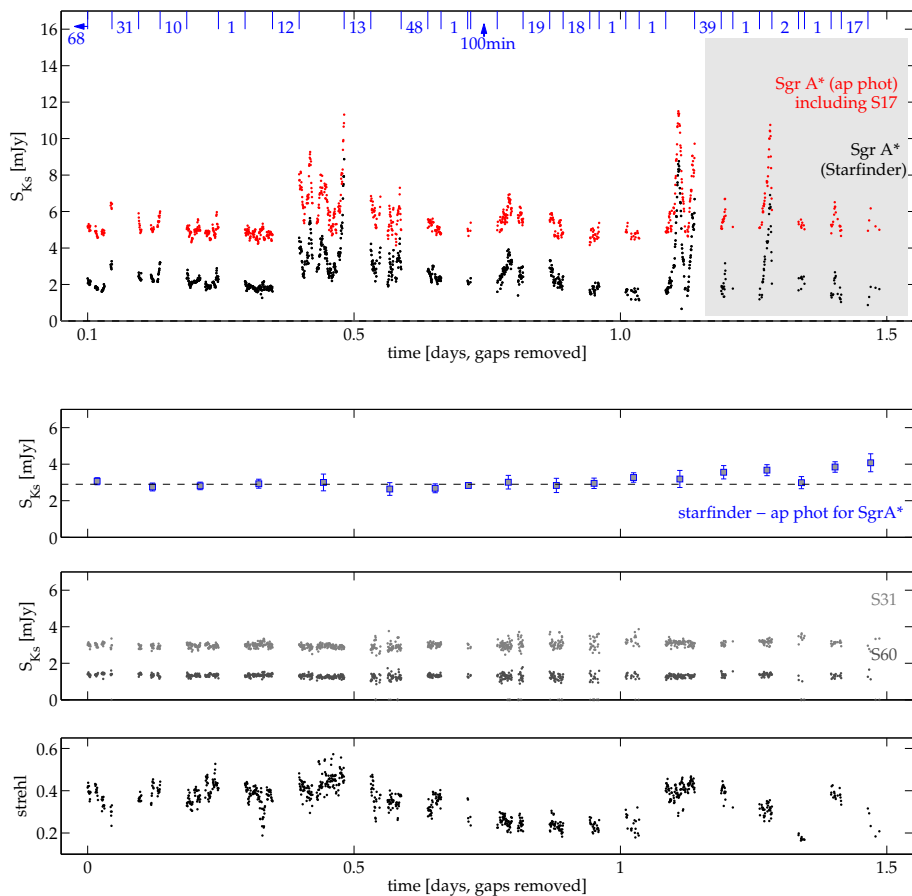
Figure 6.5 *Top:* Lightcurves from aperture photometry (described Section 6.2.1) and from Starfinder for 2009 Ks-band, 13 mas pix imaging data. We have not removed here the long-term trend that we did for the 2004-2009 lightcurve. The large gaps in time are removed so that the data can be seen in better time resolution; the real gaps in time between the individual datasets are shown at the top of the figure in days (the first dataset is 68 days from Jan 1, 2009). The data were selected on the basis of whether the star S21 (1.33 mJy) was detected or not, and then only those images (87%) in which a source was detected within 20 mas of the position of Sgr A*. Data from September-October 2009, where the faint star confused with Sgr A* begins to be separated (see Figure 6.4) is shaded in gray: this data was not used for creating the flux distribution shown in Figure 6.8. *Second from top:* Median flux differences between aperture photometry and Starfinder measurements. There is a systematic increase in the offset between the measured fluxes from the aperture photometry method and the Starfinder method towards the end of the year. *Third panel:* Lightcurves of comparison stars: S31 (2.97 ± 0.16 mJy) and S60 (1.30 ± 0.11 mJy). S31 and S60 are of similar separation and flux ratio to S17 and Sgr A* (when Sgr A* is faint). *Bottom:* Strehl ratio as calculated from the PSFs extracted in the Starfinder photometry routine.

than measured by Starfinder due to the same effect, 2.9 mJy may be an underestimate for the true flux of S17 applicable to our aperture photometry method (i.e. its contribution to our 2004-2009 flux distribution), while 3.3 mJy from Starfinder photometry is probably an overestimate (not for the true flux, but for the flux as measured by our aperture photometry method, which is as mentioned above slightly fainter due to the higher stellar background around Sgr A*). Therefore we estimate the contribution of the flux of S17 to our 2004-2009 lightcurve produced via aperture photometry to be in the range $2.9 - 3.3$ mJy.

6.3   Results

6.3.1   Flux Distribution

For the flux distribution, we define the detection frequency in bin k as

$$\text{freq}_{\text{det},k} = \frac{\Sigma_{i=1}^{N} \Delta t_i (F_k < F_i < F_{k+1})}{(F_{k+1} - F_k)\Sigma_{i=1}^{N} \Delta t_i}. \tag{6.1}$$

where Δt_i and F_i are the exposure time and flux of the ith image, respectively, there are N images and F_k and F_{k+1} denote the bin edges. The detection frequency in each bin is divided by the bin width so that the area under the measured flux distribution is equal to 1. In the flux distribution each lightcurve data point was weighted by its exposure time so that the flux distribution is not biased towards observations with shorter time samplings. We chose a logarithmic binning with bins spaced at intervals separated by a factor of $10^{0.05}$. The errors for each bin are computed as the square root of the exposure times in the bin added in quadrature (with the same normalization as in Equation 6.1) i.e.

$$\sigma(\text{freq}_{\text{det},k}) = \frac{\sqrt{\Sigma_{i=1}^{N}(\Delta t_i (F_k < F_i < F_{k+1}))^2}}{(F_{k+1} - F_k)\Sigma_{i=1}^{N} \Delta t_i}. \tag{6.2}$$

The flux distribution of Sgr A* for the years 2004-2009 as derived from aperture photometry is shown in Figure 6.6 with various model fits (described in the next Section), as well as for a comparison star.

Models for the Flux Distribution

The parameters and fit results for the models presented in this Section are given in Table 6.3 and Figure 6.6.

Comparison Star

The comparison star S7 can be fit by a single Gaussian

$$P_{\text{gauss}}(F) = \frac{1}{\sqrt{2\pi\sigma_{\text{obs}}^2}} \exp(-(F - F_b)^2/2\sigma_{\text{obs}}^2) \tag{6.3}$$

Table 6.3.   Fits to the observed flux distribution

Model	μ_* [mJy/ln(mJy)]	σ_* [mJy/ln(mJy)]	F_b [mJy]	F_t [mJy]	s	σ_{obs} [mJy]	p_{var} [%]	χ^2/dof
Aperture photometry 2004-2009 data (Ks-band: 13mas pix imaging, 27mas pix imaging, 13mas pix imaging polarimetry):								
S7: Gaussian								
no trend removed	-	-	4.900 ± 0.007	-	-	0.483 ± 0.006	-	37.2/8
trend removed	-	-	4.663 ± 0.006	-	-	0.437 ± 0.005	-	60.2/8
Gaussian	-	-	4.69 ± 0.01	-	-	0.668 ± 0.008	-	992.4/19
Lognorm	0.19 ± 0.03	0.76 ± 0.02	3.52 ± 0.02	-	-	-	-	196.7/18
Lognorm+tail	0.76 ± 0.05	0.39 ± 0.02	2.6 ± 0.1	4.5 ± 0.1	3.3 ± 0.2	-	-	92.3/16
Lognorm+err	-0.31 ± 0.08	1.03 ± 0.05	3.89 ± 0.05	-	-	0.41 ± 0.02	-	46.9/17
Lognorm+tail+err	$\mathbf{-0.07 \pm 0.10}$	$\mathbf{0.84 \pm 0.07}$	$\mathbf{3.71 \pm 0.08}$	$\mathbf{4.8 \pm 1.4}$	$\mathbf{2.7 \pm 0.2}$	$\mathbf{0.38 \pm 0.02}$	-	**30.2/15**
$p_{var} \times$ *Lognorm+err*	-0.14 ± 0.08	1.01 ± 0.04	4.20 ± 0.05	-	-	0.44 ± 0.02	65 ± 7	42.6/16
Starfinder, 2009 data (Ks-band: 13mas pix):								
S21: Gaussian	-	-	1.333 ± 0.003	-	-	0.090 ± 0.003	-	29.5/6
S60: Gaussian	-	-	1.309 ± 0.004	-	-	0.098 ± 0.003	-	29.2/6
Lognorm+err	-0.01 ± 0.07	0.81 ± 0.06	1.39 ± 0.05	-	-	0.13 ± 0.05	-	18.2/13
Lognorm+tail+err	$\mathbf{0.04 \pm 0.12}$	$\mathbf{0.8 \pm 0.1}$	$\mathbf{1.3 \pm 0.1}$	$\mathbf{4.9 \pm 0.9}$	$\mathbf{2.1 \pm 0.6}$	$\mathbf{0.11 \pm 0.07}$	-	**15.1/11**
$p_{var} \times$ *Lognorm+err*	-0.07 ± 0.08	0.85 ± 0.07	1.9 ± 0.04	-	-	0.24 ± 0.02	66 ± 6	15.0/12

Note. — Best fit parameters and formal fit errors. For description of the models and the parameters refer to Equations 6.3, 6.4, 6.5, 6.6, 6.7, 6.8 and the accompanying text. The degeneracy between continuously variable models (i.e. *Lognormal+errors* and *Lognormal+tail+errors*) and non-continuously variable (i.e. $p_{var} \times Lognormal+errors$) is broken by the comparison of 2004-2009 aperture photometry with 2009 Starfinder data and the 2009 Starfinder data in particular shows that Sgr A* is continuously variable. Both methods/datasets result in very similar best fit parameter values for the lognormal distribution which describes the low fluxes. The 2004-2009 data on the other hand gives the best statistics on the higher, less common, fluxes of Sgr A*: the model fits to the 2004-2009 distribution show that the high flux tail of the distribution flattens significantly at high fluxes (99.98% confidence), compared to what would be expected if the flux distribution were described purely by a lognormal distribution. See Section 6.3.1 for more details.
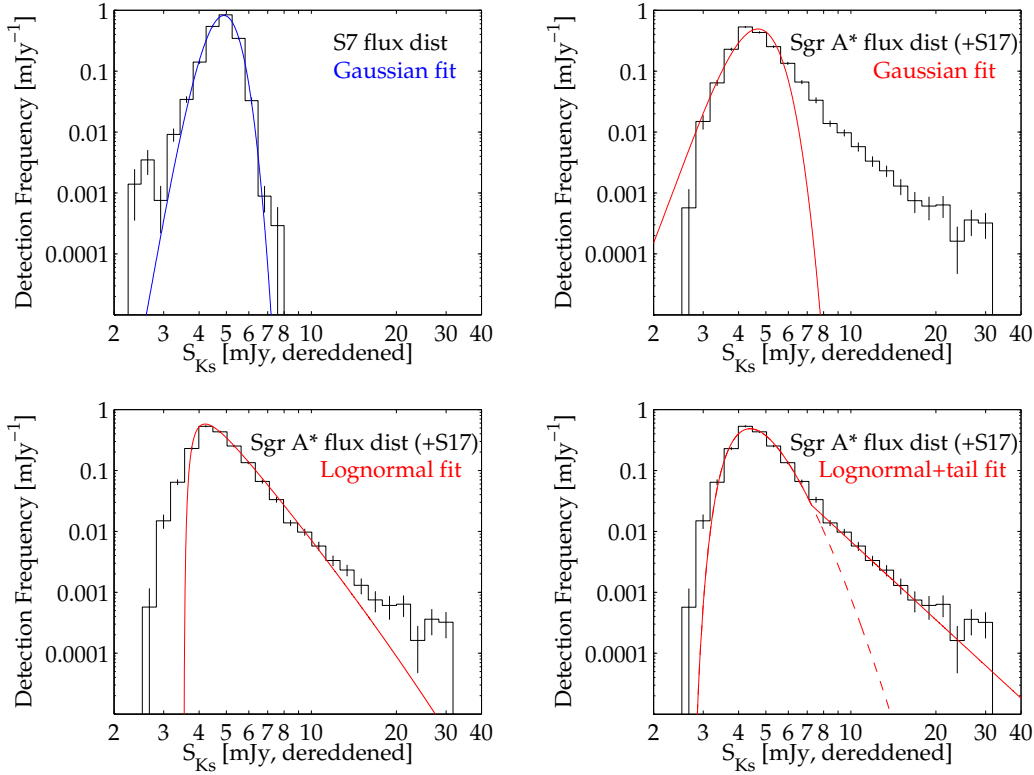
Figure 6.6 Flux distributions for comparison star S7 and for Sgr A*+S17 from 2004-2009 Ks-band data. All flux distributions have bins spaced at logarithmic intervals $10^{0.05i}$ and are shown in log-log scaling. See Table 6.3 for the model fits and best fit parameters. *Top left:* the flux distribution of S7 which is fit by a Gaussian with $\mu = 4.90$ and $\sigma = 0.48$. The flux distribution is well fit by a Gaussian around the peak of the distribution, but there is a low flux wing which is the main contributor to the reduced chi-square for this fit, $\chi^2/\mathrm{dof} \simeq 4.7$ (see Table 6.3). *Top right:* Flux distribution for Sgr A*+S17, with the best-fitting Gaussian model. *Bottom left:* Flux distribution for Sgr A*+S17, with the best-fitting lognormal model (Equation 6.4). *Bottom right:* Flux distribution for Sgr A*+S17, with the best-fitting lognormal+tail model (Equation 6.5). The dashed line shows how the lognormal component which provides the best fit to the low fluxes would continue to high fluxes.

of mean flux $F_b = 4.900 \pm 0.007$ (dereddened) and standard deviation $\sigma_{obs} = 0.483 \pm 0.006$, consistent with the magnitude reported in Gillessen et al. (2009) corresponding to a dereddened flux of 5.1 mJy. That the fit has a reduced χ^2 of $\chi^2/\mathrm{dof} \simeq 4.7$ (i.e. not a very good fit) is not so surprising given that the 2004-2009 dataset incorporates data taken under a large variety of conditions for which a single Gaussian profile is not a perfect description of the measurement errors (the largest residuals of the fit are in the low flux wing of the Gaussian profile around 4 mJy). These wings to the distribution, while the rest is well fit by a Gaussian profile, are on the 0.1% level. We can expect to obtain better fits for truly variable sources where the flux

distribution is spread out over a larger flux range such that the effect of such wings to the error distribution has a negligible on the observed flux distribution. The error on the mean, 0.007 mJy, is very close to the expected error on the mean for a source with a standard deviation of $\sigma_{obs} = 0.483$ and $N = 6774$ measurements: $\sigma_{obs}/\sqrt{N} = 0.006$.

We also present a fit to the S7 lightcurve where a trend was removed from the lightcurve in the same way as was done for Sgr A*.

Sgr A*

The flux distribution of Sgr A* is very different to that of S7. It is obvious that for Sgr A* a Gaussian is a very bad fit for the observed flux distribution (and has $\chi^2/\text{dof} \simeq 56$). The best-fitting Gaussian ($\mu = 4.69$ mJy, $\sigma = 0.67$ mJy) also has a much larger variance compared to the fit to the S7 flux distribution. We find the flux distribution of Sgr A* is better fit by a lognormal distribution with a total probability of 100% (i.e. constantly variable),

$$P_{\text{logn}}(F) = \frac{1}{\sqrt{2\pi}\sigma^*(F - F_b)} \exp\left(-\frac{(\ln(F - F_b) - \mu^*)^2}{2\sigma^{*2}}\right) \tag{6.4}$$

with parameters $\mu^* = 0.19 \pm 0.03$, $\sigma^* = 0.76 \pm 0.02$ and $F_b = 3.52 \pm 0.02$ mJy. Here F is the observed flux, and $F > F_b$ with F_b a flux offset due to some constant contribution (e.g. S17 + contaminating stars). The parameters μ^* and σ^* have a natural analogy to the normal distribution when exponentiated: the source can be thought of as having a median flux of $\exp(\mu^*) = 1.2$ with a multiplicative standard deviation of $\exp(\sigma^*) = 2.1$ (i.e. the interval $\exp(\mu^*)/\exp(\sigma^*)$ to $\exp(\mu^*) \times (\exp\sigma^*)$ contains $\approx 68\%$ of the probability).

However, a pure lognormal does not describe the entire flux distribution. There are large residuals at low fluxes (which are likely due to observation errors, see Section 6.3.3), and large residuals above ~ 8 mJy where the flux distribution of Sgr A* exhibits a flatter tail than that of the lognormal distribution, extending out to the maximum observed flux of ~ 30 mJy. To quantify the degree of flattening and its significance we fit the flux distribution with a model

$$P_{\text{logn+tail}}(F) = \begin{cases} kP_{\text{logn}}(F) & : F \leq F_b + F_t \\ kP_{\text{logn}}(F_t)\left(\frac{F - F_b}{F_t}\right)^{-s} & : F > F_b + F_t \end{cases} \tag{6.5}$$

where $P_{\text{logn}}(F)$ is the lognormal distribution of Equation 6.4, F_t is the flux at which the distribution makes the transition to the flatter tail, s is the power-law slope of the tail, and k is a renormalizing factor $k = 1/(\frac{1}{2} + \frac{1}{2}\text{erf}((\ln F_t - \mu_*)/\sqrt{2\sigma_*^2}) + F_t P_{\text{logn}}(F_t)/(s-1))$ such that the total probability is 100%.

The addition of the flatter tail to the model improves the fit significantly: from $\chi^2 = 196.7$ to 94.0, for only 2 additional degrees of freedom. The improvement is significant at $\gg 99.99\%$.

6.3.2 Is Sgr A* really continuously variable?

Here we examine the question of whether Sgr A* is really continuously variable. By continuously variable we mean the source is always 'on' and varying, in comparison with a source which emits only sporadically. While we have fitted only continuously variable models to the flux distribution
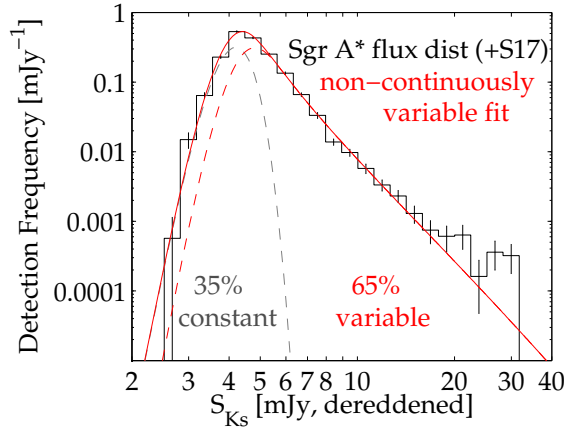
Figure 6.7 A non-continuously variable model for the flux distribution of Sgr A*; the grey dashed line shows the 'off' state, where the flux arises solely from a constant component with observational errors which has 35% of the total probability, and the red dashed line shows the 'on' state which has 65% of the total probability. The red solid line shows the total flux distribution.

in the previous Section, the flux distribution can also be fit by a non-continuously variable model where a lognormal component is present (turns "on") only a fraction p_{var} of the time,

$$
\begin{aligned}
P_{\mathrm{non-continuous}}(F) &= p_{\mathrm{var}} \int P_{\mathrm{logn}}(F')P_{\mathrm{gauss}}(F-F')dF' \\
&+ (1-p_{\mathrm{var}})P_{\mathrm{gauss}}(F)
\end{aligned}
\tag{6.6}
$$

$P_{\mathrm{logn}}(F)$ is the lognormal distribution of Equation 6.4, and it is convolved with the observational errors (see next Section). When the lognormal component is not present, the lightcurve from Sgr A* is due solely to the underlying constant component plus observational errors. Figure 6.7 (with parameters given in Table 6.3) shows the best fit non-continuously variable model for the 2004-2009 flux distribution which has $p_{\mathrm{var}} = 65 \pm 7\%$. That the observational errors of this best fit distribution (a relative error $\sigma_{\mathrm{obs}}/F_{\mathrm{peak}} \approx \sigma_{\mathrm{obs}}/F_b = 10.5 \pm 0.5\%$) are not overly high compared to that of e.g. S7, a star of similar flux (relative error $9.4 \pm 0.1\%$) demonstrates that this model also provides a plausible explanation for the 2004-2009 aperture photometry flux distribution.

To beat this model degeneracy and the influence of observation errors we need to do higher precision photometry. The method selected to analyze the 2004-2009 dataset was used with the aim of keeping the dataset overall as large and homogeneous as possible to analyze in particular the statistics of the high fluxes of Sgr A* compared to the low fluxes. However for the issue of whether the variability is continuous at low flux levels, which are so much more common, we can reasonably take just an unbiased subset of good data from one year for a more detailed analysis. We chose to carry out Starfinder photometry on our 2009 Ks-band 13 mas imaging data (as was described in Section 6.2.2) which was the year with the most high quality, 13mas imaging data, and in which S17 and Sgr A* can be resolved separately. Due mostly to the separation of S17 from Sgr A*, we obtain much higher precision on our recorded fluxes.

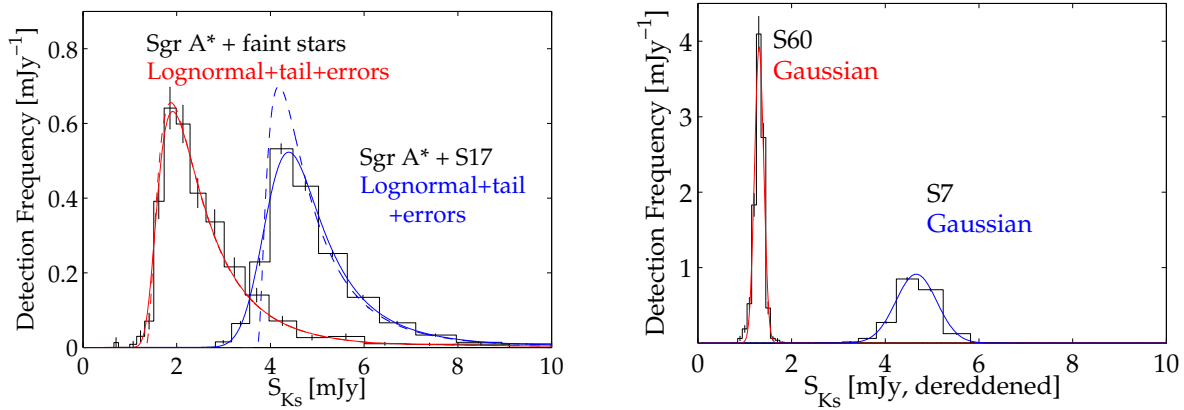We produce and compare flux distributions for Starfinder (2009 data) and aperture photom-

Figure 6.8 *Left:* Comparison of the flux distribution created from Starfinder photometry of data taken March-August 2009 (Sgr A* plus the two new faint stars resolved in 2010), with the 2004-2009 flux distribution from aperture photometry (Sgr A* + S17). The flux axis is scaled linearly for the comparison since there is a constant offset between the two flux distributions due to the different stellar contributions. Apart from the constant off-set the differences between the two distributions can be attributed to observation errors, which has a smearing effect on the peak of the distribution. The best fits to both distributions including observational errors results in a similar intrinsic flux distribution for both datasets. The 2009 flux distribution has much too much variability for the low flux end of the distribution to be explained solely by observational errors: Sgr A* is continuously variable. *Right:* Comparison stars typical of the flux at the peak of the distribution for Starfinder (S60) and aperture photometry methods (S7).

etry methods, for which the results are shown in Figure 6.8. For producing the Starfinder flux distribution we only use the data from March to August where the sources are reliably detected with Starfinder. Despite the much smaller photometric errors obtained with Starfinder photometry, the flux distribution looks very similar to that obtained with the aperture photometry method (with an offset accounting for S17). Though it does have a sharper peak and is less smeared out by the observational errors than the 2004-2009 aperture photometry distribution, the peak still has too much variability compared to the comparison stars, indicating that true intrinsic variability and not photometric errors dominates the shape of the flux distribution at low fluxes. The best fit non-continuously variable model requires a Gaussian of width $\sigma = 0.24 \pm 0.02$ mJy, a relative error of $13 \pm 1\%$ on the constant component of 1.9 mJy – which for this data is much too large to arise from photometric errors (relative errors are $6.8 \pm 0.2\%$ and $7.5 \pm 0.2\%$ mJy for stars S21 and S60 of $\sim$1.3 mJy). We can thus conclude that Sgr A* is indeed continously variable.

6.3.3   The Effect of Observation Errors on the Flux Distribution

The comparison of 2009 Starfinder and 2004-2009 Aperture Photometry datasets also shows that the observational errors can have a non-insignificant influence on the flux distribution, especially for the 2004-2009 dataset. The flux distribution suffers most from observational errors at the

lowest fluxes. We can account (to first order) for the smearing effect of the observational errors on the flux distribution at low fluxes by convolving the intrinsic flux distribution with a Gaussian of width σ_{obs} (Equation 6.3)

$$P_{\mathrm{logn+err}}(F) \;\; = \;\; \int P_{\mathrm{logn}}(F')P_{\mathrm{gauss}}(F - F')dF' \tag{6.7}$$

$$P_{\mathrm{logn+tail+err}}(F) \;\; = \;\; \int P_{\mathrm{logn+tail}}(F')P_{\mathrm{gauss}}(F - F')dF'$$

$$\tag{6.8}$$

Trying such models we obtain significantly better fits for both intrinsically lognormal and lognormal+tail models, which are presented in Figure 6.9 and Table 6.3. The best fit observational errors seem reasonable at $\sigma_{\mathrm{obs}}/F_{\mathrm{peak}} \approx 8.9 \pm 0.5\%$ (where the peak of the distribution occurs at $F_{\mathrm{peak}} = F_b + \exp(\mu_* - \sigma_*^2)$), compared to S7 with $9.4 \pm 0.1\%$. Although the addition of the observational errors allows the lognormal component to have a more extreme tail, a flatter tail to the distribution is still significant at 99.98% confidence ($\sim 3.1\sigma$).

Fitting the Starfinder distribution with models including our prescription for the observational errors, we find for the best fit models the errors are reasonable when compared with those of the two comparison stars. For these models the errors also have only a small smearing effect on the peak of the distribution (Figure 6.9). The parameters deduced from this dataset for the lognormal component agree well with those deduced from the 2004-2009 aperture photometry. Despite the smaller dataset (which only reaches to fluxes of ~ 10 mJy) the 2009 Starfinder distribution also shows a flattened high flux tail with parameters consistent with that of the 2004-2009 aperture photometry distribution, though with a lower significance of 78.8%.

As a final comment, the observational errors are not perfectly described by a Gaussian, as can be seen in the large χ^2/dof values of the Gaussian fits to the stars which might mean that are oversimplifying in our treatment of the observational errors. However, the differences are in the very low probability wings of the distributions, and around the peak the errors are indeed well fit by a Gaussian. A more critical point is that the Gaussian with which we convolve the entire flux distribution also has a fixed width, while more realistically the width of the Gaussian (the error) could change with flux (in a photon-noise dominated regime, for example; Fritz et al. 2010). That we find good agreement between parameter fits of the 2004-2009 aperture photometry flux distribution and that of the 2009 Starfinder photometry however, where the errors have little effect on the shape of the flux distribution (Figure 6.9), seems to show that the use of a fixed-width Gaussian to simulate the effect of the errors in the 2004-2009 aperture photometry flux distribution was a reasonable approximation. Indeed since Sgr A* is mostly at faint fluxes (e.g. magnitudes $m_{Ks} \gtrsim 16$ mag), the flux measurements are probably dominated more by constant read noise than by flux-dependent photon noise (Fritz et al., 2010).

6.3.4   Long timescale variability ($\sim$weeks to months)

A notable feature of the lightcurves for 2009 (Figure 6.5) is the presence of longer timescale trends in the low flux level of the lightcurves, such as an ~ 0.8 mJy increase in the minimum level from the fourth to the fifth data sections, with a gap in time of only 12 days, and a similar size decrease from the second to the fourth data sections with a gap in time of only 11 days.

It might be that a passing star (such as the two new stars discovered in 2010, see Section 6.2.1) is responsible for these trends, either passing in and out of confusion very quickly, or even
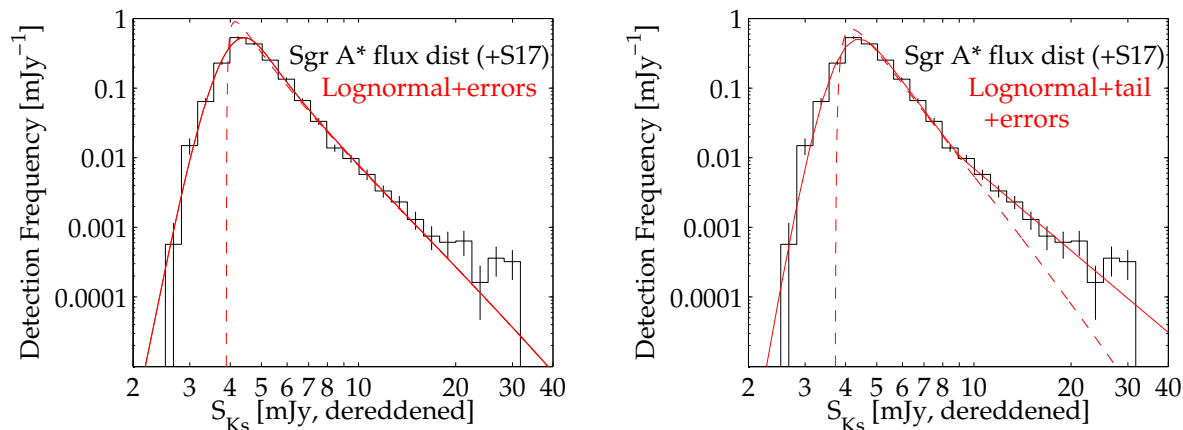
Figure 6.9 The effect of observational errors on the lognormal and lognormal+tail fits to the 2004-2009 flux distribution. A flatter tail is still a significant improvement to the fit, at 99.98% confidence.

just moving within the Sgr A* PSF and distorting the flux: the further apart the two sources the lower the fitted flux. However these stars cannot move quickly enough for this: the change in flux is so large that in either case the star must move by at least ∼50mas within a period of 12 days to distort the flux as much as observed, which at the 8kpc distance of the GC requires an average speed of at least $0.1c$ over a two week timescale. Even assuming the most extreme case – a star moving only in the plane of the sky and falling towards Sgr A* in a parabolic orbit at the escape speed – a star should take at least ∼110 days ($0.02c$ in average), to cover such a distance. A larger centroid shift between the datasets would also be expected if it were the case that a star were distorting the source PSF (∼20 mas instead of the observed ∼ 5 − 8mas). Furthermore, even if this could explain the trend between the fourth and fifth datasets, the same explanation would have to be invoked to again explain the variation between the second and fourth datasets, also on a timescale of only ∼11 days.

We therefore conclude that the observed trends on timescales of a few weeks in the lightcurve are most likely intrinsic. Though they can not be due to direct flux contamination from passing stars, they are possibly still related to the feeding of the accretion flow from their stellar winds which may trigger increased activity as the star passes orbital pericenter (e.g. Loeb 2004).

6.4   Discussion/Interpretation

6.4.1   Two states of Sgr A* in the near-infrared

We have shown in Section 6.3 that the flux distribution of Sgr A* is best described by a (continuously present) lognormal component at low fluxes but that there is a significantly flatter tail above about 5 mJy, implying that *there is something different about the high flux emission from Sgr A**. Given this fact, and that the low flux emission is continuously variable, it seems justified to identify

- emission below 5 mJy as *quiescent state* emission

- emission above 5 mJy as *flaring* emission.

This is the (phenomenological) definition by which we hereafter refer to either 'flares' or 'quiescent' emission in Sgr A*. We present how the two states may fit into a possible physical picture below.

Quiescent State Emission

That the low fluxes of Sgr A* are fit by a continuously present, variable component suggests that there is truly a *quiescent state*[3] in Sgr A*, i.e. a low-level, lognormally varying component (factor ~2.3 in flux of the lognormal component corresponds to 1σ variability). Our finding of continuous variability confirms the findings of Do et al. (2009a) who first reported continuous variability of Sgr A* from the larger variance of the flux of Sgr A*, as compared to stellar sources, in 5 out of 6 K'-band observation nights.

Lognormal distributions of fluxes are seen in X-ray binaries, where they are interpreted as a sign that multiplicative processes are behind the variability (e.g. Uttley et al. 2005). A good example of a multiplicative process is the model of Lyubarskii (1997) where variability is produced through the inwards propagation of accretion rate fluctuations at different radii. These variations, produced in regions of the flow which themselves do not emit near-infrared emission, all combine multiplicatively as they propagate inwards. The end result of combined fluctuations is then imprinted on the variability produced by the (say, near-infrared) emitting region of the flow. A very similar idea may work with magnetic turbulence, which has been shown in GRMHD/MHD simulations to be capable of producing the factor 40-50% millimeter variability (Dexter, Agol, & Fragile , 2009; Chan et al., 2009; Goldston et al., 2005).

From where exactly the quiescent emission arises is however a difficult question. Nonthermal electrons are required to emit in the near-infrared, and it's not clear how these should be related to the thermal electrons emitting at submm wavelengths, or how they should necessarily be arranged within the accretion inflow/outflow. Yuan et al. (2003, see also Özel et al. 2000) require a hybrid thermal/non-thermal electron distribution to explain the spectrum of Sgr A* (in particular the excess radio emission at low frequencies). The models predict that the same non-thermal electrons (with ~1.5% of the thermal energy) could produce emission in the near-infrared. Thus it might be interesting to compare the flux distribution of the NIR quiescent state emission ($F \lesssim 5$ mJy) with that of the low-frequency radio emission, as well as correlations in timing properties, such as whether the medium-timescale trends (~2 weeks) observed in the 2009 data (Figure 6.5) correlate with any similar long-term trends in the radio regime. More detailed comparison of the low-level NIR emission from Sgr A* with other wavelengths (e.g. submm) could also shed light on how non-thermal electrons are related to the thermal population.

Flaring Emission

It seems unlikely that the same variability process is responsible for both high and low flux emission from Sgr A*. There is no obvious reason for the underlying process, if multiplicative at low fluxes, to deviate at high fluxes. The flatter tail of the flux distribution in Sgr A* requires at the very least some transition within the source (to a *flaring state*), triggered around 5 mJy, such that either large fluctuations or their emission undergo some kind of runaway amplification.

---

[3]a *quiescent yet variable state*, in a similar sense to the quiescent state of longer wavelengths which nevertheless exhibits variability (factor 20-100% in radio to submm regime).

On the other hand the physical mechanism behind the flares could be unrelated to (though possibly still triggered by) the mechanism producing the low level variability. The flare tail could arise from additional sporadic *flare events* which dominate the distribution of fluxes above 5 mJy. Here the transition flux of 5 mJy is determined only by how the collective flux distribution of flare events compares to the flux distribution of the lognormal component, and is essentially the flux at which one is equally likely to see either a flare event or a low level lognormal variation.

Spontaneous magnetic reconnection is a good candidate for a physical process that could give rise to sporadic flares in Sgr A* (e.g. Yuan et al., 2003; Ding et al., 2010). The decrease in magnetic field strength that would accompany the conversion of magnetic energy to high energy electron acceleration in a magnetic reconnection event can explain the non-one-to-one rise in the lightcurves of the so far brightest NIR/X-ray flare from Sgr A* (Dodds-Eden et al., 2010a).

A number of other properties also indicate that there are two types of NIR emission from Sgr A*, with differences between high and low flux emission, which include:

- *Spectral Index.* There are indications that the spectral index at low fluxes is redder than at higher fluxes (Ghez et al., 2004; Eisenhauer et al., 2005a; Gillessen et al., 2006; Yusef-Zadeh et al., 2009), although this has been disputed by other authors Hornstein et al. (2007).

- *Polarization.* Changes in polarization in the rising/decaying phases of flares are seen (Eckart et al., 2006b), and low level emission appears to be generally more highly polarized ($\sim 30 - 40\%$) than high flux emission ($\sim 10\%$) (Meyer et al., 2006; Trippe et al., 2007).

- *Association with X-ray flares.* The best fit model (*Lognormal+tail+errors*) to the 2004-2009 flux distribution has 6.6% of the probability above $F_t = 4.8$mJy, which, interestingly, is much closer to the X-ray flaring rate of $\approx 4 - 7\%$ (for flares occuring once a day with a duration of 60-100 min; Baganoff 2003). In contrast, estimates of the NIR flaring rate including emission below 5 mJy typically put the NIR flaring rate much higher at $\approx 40\%$ (Eckart et al., 2006a; Yusef-Zadeh et al., 2006a), while our non-continously variable model gives 65%. Perhaps the additional low-level component is even responsible for differences in the NIR/X-ray peak flux ratios.

There are a number of high flux Ks/K'-band events ($\gtrsim 5$ mJy), not part of the 2004-2009 dataset presented here but published elsewhere in the literature, are also of $\gtrsim 5$ mJy intrinsic flux and can be identified as belonging to the flare tail of the flux distribution. To list some of the brightest (see Table 6.1 for details): ≈ 11 and 8.4 mJy (15, 16 June 2003; Genzel et al., 2003b); 20.1 mJy (6 October 2003; Meyer et al., 2007); 13.5 mJy (31 May 2006; Trippe et al. 2007, Meyer et al. 2007, and part of our 2004-2009 dataset); 10.7 mJy (15 May 2007; Eckart et al., 2008a); and 14.8 mJy (Hornstein et al., 2007).

6.4.2 Consistency with previous measurements of Sgr A* at low Ks-band fluxes

Previous measurements have put upper limits on any long-term steady quiescent state at near-infrared wavelengths which have been on the $\sim$1-1.5 mJy level (Hornstein et al., 2002; Schödel et al., 2007; Sabha et al., 2010, see Table 6.2). The true upper limit on the intrinsic flux from Sgr A*

could be even lower, 0.5 mJy, if there is a ∼0.8-1 mJy stellar contribution to the flux (Sabha et al., 2010).

For a lognormally varying quiescent state with the properties of our best fit model to the 2004-2009 flux distribution, an upper limit of 1-1.4 mJy in selected observations is not so surprising: the source is expected to be at ≲1 mJy roughly 50% of the time. Fluxes ≲0.5 mJy would be rarer, but still not unlikely, occurring ∼ 20% of the observing time.[4] The 0.8-1.0 mJy diffuse component found by Sabha et al. (2010) also finds a direct match with the ∼0.4-0.8 mJy offset we find in our fits to the flux distribution of Sgr A*, between the fitted constant component (3.7 mJy) and the expected contribution of S17 (2.9-3.3 mJy). Do et al. (2009a) estimated from the color of Sgr A* at low fluxes, that they most likely had ∼35% contribution from stellar contamination (0.7 mJy) for their observations in 2006. Thus these results all seem to point towards a relatively steady ∼0.6-1.0 mJy stellar component to the flux of Sgr A*.

We note that our results are also reasonably consistent with the median flux of 2.0 mJy over six separate observation nights from 2006-2007 found by Do et al. (2009a) (see Table 6.2 for the scaling factors applied to scale the reported values to our calibration/extinction). We, in comparison, find a median flux of ≈1.6 mJy for our 2004-2009 lightcurve with the long-timescale trend (and S17, assuming 3.1 mJy) removed.

6.4.3   Comparison with X-ray binary variability

A component with a lognormal distribution of fluxes in Sgr A* also implies a connection to X-ray binaries, where lognormal distributions of fluxes have been seen (prototype Cyg X-1 in the low hard state, Uttley et al., 2005). This may provide evidence that the accretion processes in Sgr A* are similar to those of other black holes (Falcke et al. 2003, McHardy et al. 2006). Thus insights gained about the physical processes occurring in both Sgr A* and in Cygnus X-1 might be used to complement the study of the other.

The physical picture of the low-hard state of X-ray binaries is that – compared to higher luminosity flows – the inner optically thick accretion disc disappears and is replaced by a hot inner flow (Done et al., 2007). Similar pictures, with hot inner flows, exist for Sgr A* (e.g. Quataert, 2003). Sgr A* is, however, at the extreme low end of the accretion rate range of observable sources (the 'quiescent' state). Connections between Sgr A* and low-hard state X-ray binaries of higher accretion rate such as Cygnus X-1 can shed light on whether or not the quiescent state is indeed a distinct state or whether there is simply a smooth continuation of the hard state down to such low accretion rates (Markoff 2010).

A connection between the near-infrared variability of Sgr A* and the variability of X-ray binaries has also been made from a long timescale break in the PSD of Sgr A* which can be associated with a break timescale in the low-hard state of X-ray binaries (Meyer et al. 2009), though the single dataset used to constrain the high frequency power spectrum in this case may not be representative. The lognormal distribution for low-level fluxes makes however an independent case for an analogy between the variability of Sgr A* and low-hard state X-ray

---

[4]We note that for the same dataset (September 23, 2004) our aperture photometry method yields a flux of 1.0 mJy with aperture photometry (with S17 and the empirical background fit subtracted). This compares favourably with that of Sabha et al. (2010, 0.8-1.0 mJy, scaled to our calibration) obtained with aperture photometry after PSF-extraction of all known sources close to Sgr A* including the star identified in that work as S62.

binaries.

If timescale scales with mass, then the flares in Sgr A* of ∼10-100 minute duration, correspond to ≈ millisecond timescales in a stellar mass black hole binary. Indeed, it is also true that millisecond-timescale flares are seen in Cyg X-1, though it was shown by Uttley et al. (2005) that the majority of these (and all those in the low/hard state) were not more frequent than expected in the context of the extension of the low-level lognormal distribution in this source to higher fluxes. There was one flare however, a 12.4σ event that occurred (in fact when Cyg X-1 was in the high/soft state) that could not be accounted for in the context of the underlying variability and was posited by the authors to have a different physical origin. In this vein, it could be that the flares in Sgr A* are due to the source's "flickering attempts at outburst activity from out of quiescence", as suggested by Markoff (2010).

6.4.4 Wavelength Dependence

Investigating the wavelength dependence of the flux distribution may also shed some light on the nature of the two components to the variability. If the properties of the flux distribution (e.g. position at which the lognormal peak occurs, and the relative strength of the flat tail of the distribution) change differently with wavelength it could imply two independent variability components.

The flux distributions of Yusef-Zadeh et al. (2006a) and Yusef-Zadeh et al. (2009) at 1.6μm and 1.7μm display a qualitatively similar shape to our Ks-band distribution, although these datasets are still much smaller than ours, and the low-level activity appears to be dominated by the observational noise. Nevertheless, with more data at 1.6 and 1.7 μm, it might be possible to obtain constraints on the colours of the low level and high flux components.

In future work we intend to use the same techniques as we have used in this paper at Ks-band, in other bands (L' and H) to investigate in detail the dependence of the flux distribution with wavelength.

6.4.5 Timing Analysis

Our work is not the first to point out that the flux distribution of Sgr A* is not well-described by a Gaussian: Yusef-Zadeh et al. (2006a), Do et al. (2009a) and Yusef-Zadeh et al. (2009) have all noted that the flux distribution has a high flux tail. However, the timing analyses which have been carried out to date (Do et al., 2009a; Meyer et al., 2008, 2009) in which Sgr A* was compared to simulated red noise lightcurves have nevertheless used simulated lightcurves which have had, by construction, a Gaussian flux distribution. Sgr A*'s intrinsic mean and variance are such that if one were to plot the simulated lightcurves scaled to Sgr A*'s mean and variance (for the 2004-2009 dataset $\mu = 1.3$ mJy subtracting 3.8 mJy for S17 plus other faint stars, and $\sigma = 1.9$ mJy), the model red noise lightcurves would have negative intrinsic fluxes much of the time which is rather unphysical.

In Do et al. (2009a) the high flux tail was excluded when fitting the flux distribution, and only fluxes $\lesssim 3.2$ mJy were fitted with a Gaussian (see Table 6.1 for scaling factors; the reported value in Do et al. 2009a was a reddened flux of 0.3 mJy). Thus their model lightcurves best resemble the low level emission of Sgr A*. Indeed the entire dataset used by Do et al. (2009a) does not include much bright emission $\gtrsim 5$ mJy, and thus their results really apply to the low

level emission of Sgr A*. That the low level emission from Sgr A* is consistent with red noise fits together with our finding of the lognormal distribution of fluxes at low fluxes. Both of these aspects of the variability are seen in X-ray binaries such as Cyg X-1 (Uttley et al., 2005).

However, given that the flux distribution is not Gaussian, it remains questionable that the power spectrum has yet been reliably constrained from the Monte Carlo simulations of previous timing studies. In the first place, the model lightcurves of a Gaussian flux distribution can not truly resemble the observed lightcurves from Sgr A*, and an exponential transformation is needed (Uttley et al. 2005), i.e. one essentially models the PSD of the logarithm of the observed lightcurves. Secondly however, this would be only suitable for modeling the low level lognormal component of the variability, and the models would still not produce as many high flux events as are observed.

Given that there are differences between the high and low flux states of Sgr A*, they may require separate timing analysis. In this respect it is interesting that Meyer et al. (2008) finds a quasi-periodic signal with false alarm probability of only 2×10^{-5} (4.2σ significance in Gaussian equivalent terms), if one considers just the window 385-445 minute subset from 30-31 July 2005. This signal was then deemed insignificant when the entire lightcurve from the night was analyzed. That our findings point to high flux emission from Sgr A* having a different, and perhaps episodic, character from the low-level emission, gives us, if substantiated, a valid reason to select a time window around single high flux events (e.g. those that reach peak fluxes $\gtrsim 5$ mJy). Thus it is important to further understand and characterize the high and low-level emission from Sgr A*.

6.5 Conclusions

We have determined the distribution of fluxes for the variable source Sgr A* in the near-infrared and thereby investigated flux-dependent properties of the emission. We summarize our main results as follows:

- Sgr A* is continuously variable.

- There is long-term variability (e.g. on a two-week timescale).

- At low fluxes the variability follows a lognormal distribution. We identify this continuously variable low-level state as the quiescent state of Sgr A* in the near-infrared.

- At high fluxes (above ~ 5 mJy) the flux distribution flattens which seems to be most likely explained by the presence of sporadic flare events additional to the quiescent emission.

- On August 5th 2008 we observed a very bright Ks-band flare of 27.5 mJy, the brightest Ks-band flare yet observed from Sgr A*.

Differences in spectral index, polarization properties and association with X-ray flares may already be further indications of the different nature of the high flux near-infrared emission from Sgr A*. In future work we aim to search for and quantify further possible differences between high and low flux emission of Sgr A*.

Chapter 7

Conclusions

The flares of Sgr A* carry the potential to be a probe of the physics of strong gravity close to a massive black hole, and yet their physical origin is still not known with certainty. Coordinated multiwavelength observations, spectroscopy, polarimetry are all valuable tools in trying to decipher the secrets of this enigmatic source. In this thesis we concentrated on multiwavelength and variability aspects of the emission from Sgr A* to try to obtain some insight into their physical origins. We summarize our main results as follows:

- In our detailed study of a single, high flux event at both NIR and X-ray wavelengths, we found the X-ray flare was unlikely to be due to inverse Compton scattering. Instead, the X-ray flare could be due to synchrotron emission.

- We also found that the flare was likely accompanied by a decrease in the magnetic field strength that may itself be responsible for powering the flare through the conversion of magnetic energy.

- Furthermore, we found that Sgr A* exhibits two types of variable emission in the NIR, low-level variability probably produced through some multiplicative process, on top of which isolated, high flux events sometimes occur.

These results all fit together in a scenario where the low flux emission can be associated with the steady-state emission from Sgr A*, with low-level variability due to the filtering of accretion rate or magnetic fluctuations through the accretion flow to inner radii, while the high flux emission is due to spontaneous, catastrophic events such as a magnetic reconnection.

In the future, there should be many more insights to come from the collection of more statistics and, hopefully, the observation of more multiwavelength flares of the brightness, quality and detail of the April 4, 2007 event. We plan to add dynamical (and relativistic) effects to our time-dependent SED modeling. The statistics emission at different frequencies, of polarized emission and timing properties of very large datasets such as the one presented in Chapter 6 of this thesis may shed more light on the different nature of the high and low flux emission in the NIR. The GRAVITY instrument (Eisenhauer et al., 2005a), currently in development for the Very Large Telescope Interferometer (VLTI) will have the capability to carry out 10μas astrometry ($\sim 1\ R_S$) on timescales of a few minutes for Sgr A*. With GRAVITY, a new door will be opened, as we quite possibly track the bright emission region of a NIR flare in motion close to the event horizon of a black hole.

Bibliography

Aitken, D. K., Greaves, J., Chrysostomou, A., Jenness, T., Holland, W., Hough, J. H., Pierce-Price, D., & Richer, J. 2000, ApJ, 534, L173

Arnaud, K. A. 1996, Astronomical Data Analysis Software and Systems V, 101, 17

Armitage, P. J. 1998, ApJ, 501, L189

Baganoff, F. K. et al. 2001, Nature, 413, 45

Baganoff, F. K. et al. 2003, ApJ, 591, 891

Baganoff, F. K. 2003, Bulletin of the American Astronomical Society, 35, 606

Balbus, S. A. & Hawley, J. F. 1991, ApJ, 376, 214

Balick, B., & Brown, R. L. 1974, ApJ, 194, 265

Beckwith, K., Hawley, J. F., Krolik, J. H. 2008, ApJ, 678, 1180

Bélanger, G., Goldwurm, A., Melia, F., Ferrando, P., Grosso, N., Porquet, D., Warwick, R., & Yusef-Zadeh, F. 2005, ApJ, 635, 1095

Bittner, J. M., Liu, S., Fryer, C. L., & Petrosian, V. 2007, ApJ, 661, 863

Blumenthal, G. R., & Gould, R. J. 1970, Reviews of Modern Physics, 42, 237

Bolton, C. T. 1972, Nature, 235, 271

Bombaci, I. 1996, A&A, 305, 871

Bower, G. C., Wright, M. C. H., Backer, D. C., & Falcke, H. 1999, ApJ, 527, 851

Bower, G. C., Falcke, H., Sault, R. J., & Backer, D. C. 2002, ApJ, 571, 843

Bower, G. C., Wright, M. C. H., Falcke, H., & Backer, D. C. 2003, ApJ, 588, 331

Bower, G. C., Falcke, H., Herrnstein, R. M., Zhao, J.-H., Goss, W. M., & Backer, D. C. 2004, Science, 304, 704

Bower, G. C., Goss, W. M., Falcke, H., Backer, D. C., & Lithwick, Y. 2006, ApJ, 648, L127

Broderick, A. E., & Loeb, A. 2005, MNRAS, 363, 353

Brown, R. L., & Lo, K. Y. 1982, ApJ, 253, 108

Brown, R. L. 1982, ApJ, 262, 110

Chan, C. K. et al. 2009, ApJ, 701, 521

Chiar, J. E., & Tielens, A. G. G. M. 2006, ApJ, 637, 774

Clénet, Y., Rouan, D., Gratadour, D., Marco, O., Léna, P., Ageorges, N., & Gendron, E. 2005, A&A, 439, L9

Cotera, A., Morris, M., Ghez, A. M., Becklin, E. E., Tanner, A. M., Werner, M. W., & Stolovy, S. R. 1999, The Central Parsecs of the Galaxy, 186, 240

Cohen, M., Walker, R. G., Carter, B., Hammersley, P., Kidger, M., & Noguchi, K. 1999, AJ, 117, 1864

Cuadra, J., Nayakshin, S., Springel, V., & Di Matteo, T. 2006, MNRAS, 366, 358

De Villiers, J., Hawley, J. F., & Krolik, J. H. 2003, ApJ, 599, 1238

Dexter, J., Agol, E., & Fragile, P. C. 2009, ApJ, 703, 142

Di Matteo, T., Carilli, C. L., & Fabian, A. C. 2001, ApJ, 547, 731

Ding, J., Yuan, F., & Liang, E. 2010, ApJ, 708, 1545

Diolaiti, E., Bendinelli, O., Bonaccini, D., Close, L., Currie, D., & Parmeggiani, G. 2000, Astronomical Data Analysis Software and Systems IX, 216, 623

Do, T., Ghez, A. M., Morris, M. R., Yelda, S., Meyer, L., Lu, J. R., Hornstein, S. D., & Matthews, K. 2009, ApJ, 691, 1021

Do, T., Ghez, A. M., Morris, M. R., Lu, J. R., Matthews, K., Yelda, S., & Larkin, J. 2009, ApJ, 703, 1323

Dodds-Eden, K., et al. 2009, ApJ, 698, 676

Dodds-Eden, K., Sharma, P., Quataert, E., Genzel, R., Gillessen, S., Eisenhauer, F., & Porquet, D. 2010, arXiv:1005.0389

Dodds-Eden, K., et al. 2010, arXiv:1008.1984

Doeleman, S. S., et al. 2001, AJ, 121, 2610

Doeleman, S. S., et al. 2008, Nature, 455, 78

Done, C., Gierliński, M., & Kubota, A. 2007, A&A Rev., 15, 1

Draine, B. T., & Lee, H. M. 1984, ApJ, 285, 89

Eckart, A., et al. 2004, A&A, 427, 1

Eckart, A., et al. 2006, A&A, 450, 535

Eckart, A. et al. 2006, A&A, 455, 1

Eckart, A., et al. 2006, Journal of Physics Conference Series, 54, 391

Eckart, A., et al. 2008, A&A, 479, 625

Eckart, A., et al. 2008, A&A, 492, 337

Eckart, A., et al. 2009, A&A, 500, 935

Eisenhauer, F., Schödel, R., Genzel, R., Ott, T., Tecza, M., Abuter, R., Eckart, A., & Alexander, T. 2003, ApJ, 597, L121

Eisenhauer, F., et al. 2005, ApJ, 628, 246

Eisenhauer, F., Perrin, G., Rabien, S., Eckart, A., Lena, P., Genzel, R., Abuter, R., & Paumard, T. 2005, Astronomische Nachrichten, 326, 561

Elvis, M., Page, C. G., Pounds, K. A., Ricketts, M. J., & Turner, M. J. L. 1975, Nature, 257, 656

Falanga, M., Melia, F., Prescher, M., Bélanger, G., & Goldwurm, A. 2008, ApJ, 679, L93

Falcke, H., Goss, W. M., Matsuo, H., Teuben, P., Zhao, J.-H., & Zylka, R. 1998, ApJ, 499, 731

Falcke, H., & Markoff, S. 2000, A&A, 362, 113

Falcke, H., Körding, E., & Markoff, S. 2004, A&A, 414, 895

Fender, R. P., Belloni, T. M., & Gallo, E. 2004, MNRAS, 355, 1105

Fleming, T. P., Stone, J. M., & Hawley, J. F. 2000, ApJ, 530, 464

Fragile, P. C., & Meier, D. L. 2009, ApJ, 693, 771

Fritz, T., et al. 2010, MNRAS, 401, 1177

Gaskell, C. M. 2004, ApJ, 612, L21

Genzel, R., Schödel, R., Ott, T., Eckart, A., Alexander, T., Lacombe, F., Rouan, D., & Aschenbach, B. 2003, Nature, 425, 934

Genzel, R. et al. 2003, Nature, 425, 934

Genzel, R., Eisenhauer, F., & Gillessen, S. 2010, arXiv:1006.0064

Ghez, A. M. et al. 2003, ApJ, 586, L127

Ghez, A. M., et al. 2004, ApJ, 601, L159

Giacconi, R., Gursky, H., Paolini, F. R., & Rossi, B. B. 1962, Physical Review Letters, 9, 439

Giebels, B., & Degrange, B. 2009, A&A, 503, 797

Gillessen, S., et al. 2006, ApJ, 640, L163

Gillessen, S., Eisenhauer, F., Trippe, S., Alexander, T., Genzel, R., Martins, F., & Ott, T. 2009, ApJ, 692, 1075

Goldston, J. E., Quataert, E., & Igumenshchev, I. V. 2005, ApJ, 621, 785

Goodson A. P., Böhm, K. , & Winglee, R. M. 1999, ApJ, 524, 142

Gould, R. J. 1979, A&A, 76, 306

Ghez, A. M., et al. 2005, ApJ, 635, 1087

Ghez, A. M., et al. 2008, ApJ, 689, 1044

Hawley, J. F. & Balbus, S. A. 2002, ApJ, 573, 738

Hayashi, M. R., Shibata, K., Matsumoto, R. 1996, ApJ, 468, L37

Hewish, A., Bell, S. J., Pilkington, J. D. H., Scott, P. F., & Collins, R. A. 1968, Nature, 217, 709

Ho, L. C. 2008, ARA&A, 46, 475

Hornstein, S. D., Ghez, A. M., Tanner, A., Morris, M., Becklin, E. E., & Wizinowich, P. 2002, ApJ, 577, L9

Hornstein, S. D., Matthews, K., Ghez, A. M., Lu, J. R., Morris, M., Becklin, E. E., Rafelski, M., & Baganoff, F. K. 2007, ApJ, 667, 900

Hamaus, N., Paumard, T., Müller, T., Gillessen, S., Eisenhauer, F., Trippe, S., & Genzel, R. 2009, ApJ, 692, 902

Igumenshchev, I. V., Narayan, R., & Abramowicz, M. A. 2003, ApJ, 592, 1042

Isobe, H., Miyagoshi, T., Shibata, K., & Yokoyama, T. 2006, PASJ, 58, 243

Kardashev, N. S., Kuz'min, A. D., & Syrovatskii, S. I. 1962, Soviet Astronomy, 6, 167

Kerr, R. P. 1963, Physical Review Letters, 11, 237

Krabbe, A., Iserlohe, C., Larkin, J. E., Barczys, M., McElwain, M., Weiss, J., Wright, S. A., & Quirrenbach, A. 2006, Journal of Physics Conference Series, 54, 406

Krichbaum, T. P., et al. 1998, A&A, 335, L106

Kudoh, T., Matsumoto, R., & Shibata, K. 1998, ApJ, 508, 186

Lagage, P. O., et al. 2004, The Messenger, 117, 12

Lenzen, R., et al. 2003, Proc. SPIE, 4841, 944

Lin, R. P., et al. 2003, ApJ, 595, L69

Liu, S., Petrosian, V., & Melia, F. 2004, ApJ, 611, L101

Liu, S., Melia, F., & Petrosian, V. 2006, ApJ, 636, 798

Liu, S., Petrosian, V., Melia, F., & Fryer, C. L. 2006, ApJ, 648, 1020

Lo, K. Y., Backer, D. C., Kellermann, K. I., Reid, M., Zhao, J. H., Goss, W. M., & Moran, J. M. 1993, Nature, 362, 38

Lo, K. Y., Shen, Z.-Q., Zhao, J.-H., & Ho, P. T. P. 1998, ApJ, 508, L61

Loeb, A. 2004, MNRAS, 350, 725

Loeb, A., & Waxman, E. 2007, Journal of Cosmology and Astroparticle Physics, 3, 11

Lutz, D. 1999, The Universe as Seen by ISO, 427, 623

Lynden-Bell, D., & Rees, M. J. 1971, MNRAS, 152, 461

Lyubarskii, Y. E. 1997, MNRAS, 292, 679

Mahadevan, R., Narayan, R., & Yi, I. 1996, ApJ, 465, 327

Maitra, D., Markoff, S., & Falcke, H. 2009, A&A, 508, L13

Markoff, S., Falcke, H., Yuan, F., & Biermann, P. L. 2001, A&A, 379, L13

Markoff, S. 2010, Lecutre Notes in Physics, Berlin Springer Verlag, 794, 143

Marrone, D. P., Moran, J. M., Zhao, J., & Rao, R. 2007, ApJ, 654, L57

Marrone, D. P. et al. 2008, ApJ, 682, 373

Marscher, A. P. 1983, ApJ, 264, 296

McClintock, J. E., & Remillard, R. A. 2006, Compact stellar X-ray sources, 157

McHardy, I. M., Koerding, E., Knigge, C., Uttley, P., & Fender, R. P. 2006, Nature, 444, 730

McKinney, J. C. & Gammie, C. F. 2004, ApJ, 611, 977

McKinney, J. C. 2006, MNRAS, 368, 1561

Melia, F., & Falcke, H. 2001, ARA&A, 39, 309

Merloni, A., Heinz, S., & Di Matteo, T. 2003, MNRAS, 345, 1057

Meyer, L., Eckart, A., Schodel, R., Duschl, W. J., 3, Dovciak, M., & Karas, V. 2006, Journal of Physics Conference Series, 54, 443

Meyer, L., Schödel, R., Eckart, A., Karas, V., Dovčiak, M., & Duschl, W. J. 2006, A&A, 458, L25

Meyer, L., Schödel, R., Eckart, A., Duschl, W. J., Karas, V., & Dovčiak, M. 2007, A&A, 473, 707

Meyer, L., Do, T., Ghez, A., Morris, M. R., Witzel, G., Eckart, A., Bélanger, G., & Schödel, R. 2008, ApJ, 688, L17

Meyer, L., Do, T., Ghez, A., Morris, M. R., Yelda, S., Schödel, R., & Eckart, A. 2009, ApJ, 694, L87

Misner, C. W., Thorne, K. S., & Wheeler, J. A. 1973, San Francisco: W.H. Freeman and Co., 1973,

Morris, M., Tanner, A. M., Ghez, A. M., Becklin, E. E., Cotera, A., Werner, M. W., & Ressler, M. E. 2001, Bulletin of the American Astronomical Society, 33, 841

Morrison, R., & McCammon, D. 1983, ApJ, 270, 119

Mościbrodzka, M., Proga, D., Czerny, B., & Siemiginowska, A. 2007, A&A, 474, 1

Mościbrodzka, M., Gammie, C. F., Dolence, J. C., Shiokawa, H., & Leung, P. K. 2009, ApJ, 706, 497

Nakar, E., Ando, S., & Sari, R. 2009, ApJ, 703, 675

Nayakshin, S., & Sunyaev, R. 2003, MNRAS, 343, L15

Oppenheimer, J. R., & Volkoff, G. M. 1939, Physical Review , 55, 374

Özel, F., Psaltis, D., & Narayan, R. 2000, ApJ, 541, 234

Paczynski, B. & Wiita, J. 1980, A&A, 88, 23

Porquet, D. et al. 2003, A&A, 407, L17

Porquet, D. et al. 2008, A&A, 488, 549

Pacholczyk, A. G. 1970, Series of Books in Astronomy and Astrophysics, San Francisco: Freeman, 1970,

Pantin, E., et al. 2005, The Messenger, 119, 25

Predehl, P., & Schmitt, J. H. M. M. 1995, A&A, 293, 889

Quataert, E. 2002, ApJ, 575, 855

Quataert, E. 2003, Astronomische Nachrichten Supplement, 324, 435

Rank, S. 2007, Masters Thesis, Technische Universität München.

Rees, M. J. 1988, Nature, 333, 523

Reid, M. J., Menten, K. M., Trippe, S., Ott, T., & Genzel, R. 2007, ApJ, 659, 378

Remillard, R. A., & McClintock, J. E. 2006, ARA&A, 44, 49

Rieke, G. H., & Lebofsky, M. J. 1982, The Galactic Center, 83, 194

Roche, P. F., & Aitken, D. K. 1984, MNRAS, 208, 481

Rogers, A. E. E., et al. 1994, ApJ, 434, L59

Rousset, G., et al. 2003, Proc. SPIE, 4839, 140

Rybicki, G. B., & Lightman, A. P. 1986, Radiative Processes in Astrophysics, by George B. Rybicki, Alan P. Lightman, pp. 400. ISBN 0-471-82759-2. Wiley-VCH , June 1986.,

Sabha, N., et al. 2010, A&A, 512, A2

Schmidt, M. 1963, Nature, 197, 1040

Schödel, R., et al. 2002, Nature, 419, 694

Schödel, R., Eckart, A., Mužić, K., Meyer, L., Viehmann, T., & Bower, G. C. 2007, A&A, 462, L1

Schödel, R., Najarro, F., Muzic, K., & Eckart, A. 2010, A&A, 511, A18

Schwarzschild, K. 1916, Abh. Konigl. Preuss. Akad. Wissenschaften Jahre 1906,92,Berlin,1907, 189

Serabyn, E., Carlstrom, J., Lay, O., Lis, D. C., Hunter, T. R., & Lacy, J. H. 1997, ApJ, 490, L77

Sharma, P., Quataert, E., Hammett, G. W., & Stone, J. M. 2007, ApJ, 667, 714

Sharma, P., Quataert, E., & Stone, J. M. 2007, ApJ, 671, 1696

Sharma, P., Quataert, E., & Stone, J. M. 2008, MNRAS, 389, 1815

Shen, Z.-Q., Lo, K. Y., Liang, M.-C., Ho, P. T. P., & Zhao, J.-H. 2005, Nature, 438, 62

Shakura, N. I., & Sunyaev, R. A. 1973, A&A, 24, 337

Stone, J. M. & Norman, M. L. 1992, ApJS, 80, 753

Stone, J. M. & Norman, M. L. 1992, ApJS, 80, 791

Stone, J. M. & Pringle, J. E. 2001, MNRAS, 322, 461

Shen, Z.-Q., Lo, K. Y., Liang, M.-C., Ho, P. T. P., & Zhao, J.-H. 2005, Nature, 438, 62

Tagger, M., & Melia, F. 2006, ApJ, 636, L33

Tokunaga, A. T. 2000, Allen's Astrophysical Quantities, 143

Trap, G., et al. 2010, Advances in Space Research, 45, 507

Trippe, S., Paumard, T., Ott, T., Gillessen, S., Eisenhauer, F., Martins, F., & Genzel, R. 2007, MNRAS, 375, 764

Uttley, P., McHardy, I. M., & Vaughan, S. 2005, MNRAS, 359, 345

Uttley, P., McHardy, I. M., & Papadakis, I. E. 2002, MNRAS, 332, 231

van der Laan, H. 1966, Nature, 211, 1131

Wang, L., Fang, C., & Liu, Y. Y. 2008, Ap&SS, 318, 79

Webster, B. L., & Murdin, P. 1972, Nature, 235, 37

Will, C. M. 2006, Living Reviews in Relativity, 9, 3

Yokoyama, T. & Shibata, K. 2001, ApJ, 549, 1160

Yuan, F., Quataert, E., & Narayan, R. 2003, ApJ, 598, 301

Yuan, F., Quataert, E., & Narayan, R. 2004, ApJ, 606, 894

Yuan, F., Shen, Z.-Q., & Huang, L. 2006, ApJ, 642, L45

Yuan, F., Lin, J., Wu, K., & Ho, L. C. 2009, MNRAS, 395, 2183

Yusef-Zadeh, F., et al. 2006, ApJ, 644, 198

Yusef-Zadeh, F., Roberts, D., Wardle, M., Heinke, C. O., & Bower, G. C. 2006, ApJ, 650, 189

Yusef-Zadeh, F. et al. 2008, ApJ, 682, 361

Yusef-Zadeh, F., et al. 2009, ApJ, 706, 348

Zamaninasab, M., et al. 2010, A&A, 510, A3

Zhao, J.-H., Bower, G. C., & Goss, W. M. 2001, ApJ, 547, L29

Zhao, J-H et al. 2003, ApJ, 586, L29

Zhao, J.-H., Herrnstein, R. M., Bower, G. C., Goss, W. M., & Liu, S. M. 2004, ApJ, 603, L85

Zylka, R., Mezger, P. G., & Lesch, H. 1992, A&A, 261, 119

Zylka, R., Mezger, P. G., Ward-Thompson, D., Duschl, W. J., & Lesch, H. 1995, A&A, 297, 83

Acknowledgements